Unione Europea
Fondo Sociale Europeo

Ministero dell'Istruzione,
dell'Università e della
Ricerca

Università degli Studi di
Palermo

UNIVERSITA' DEGLI STUDI DI PALERMO
FACOLTA' DI INGEGNERIA
Dottorato di Ricerca in
Ingegneria Elettronica e delle Telecomunicazioni

DEVELOPMENT OF THE PHOTON DETECTION, ACQUISITION AND OPTICAL SYSTEMS OF MODERN RING IMAGING CHERENKOV DETECTORS

Tutore:
Ch.mo Prof. Ing. Stefano RIVA SANSEVERINO

Tesi di Dottorato di:
Ing. Gianluca AGLIERI RINELLA
Ciclo XVII

Anno Accademico 2005-2006

Tesi cofinanziata dal Fondo Sociale Europeo
PROGRAMMA OPERATIVO NAZIONALE 2000/2006

"Ricerca Scientifica, Sviluppo Tecnologico, Alta Formazione"
Misura III.4. "Formazione Superiore e Universitaria"

Introduction

- Colui tra voi, o uomini, è sapientissimo, il quale come
Socrate conosciuto ha ch'ei non vale nulla in sapienza -

Platone, *Apologia di Socrate*

This thesis describes a research and development activity focused on an advanced photon detector, the LHCb Pixel Hybrid Photon Detector, and on the integration of the optical system of the Ring Imaging Cherenkov (RICH) detectors of LHCb.

LHCb is an experiment in high energy particle physics that will operate at the Large Hadron Collider at CERN, the European Organization for Nuclear Research. The author participated into the CERN Doctoral Program during his Dottorato di Ricerca.

The interest of a research on photon detectors is motivated by their role in scientific research as well as for their applications in various fields. Highly sensitive detectors of near infrared, visible or ultraviolet photons are employed in fundamental research in astronomy as well as in high energy physics and high energy astrophysics. They play an important role in analytical instrumentation for biochemistry and pharmaceutical industry. Photoluminescence spectroscopy is a powerful tool for material science, in which fast and sensitive detectors are crucial. Combining the detectors with scintillating materials permits application in X-ray spectroscopy. Devices with higher sensitivity, speed, large active areas and high spatial resolution have beneficial impact on medical imaging diagnosis tools, like X-ray tomography and fluoroscopy. It suffices to mention the reduction of the radiation dose absorbed by the patient allowed by faster and higher sensitivity detectors.

In the first chapter a description of the LHCb experiment is given, followed by a discussion of the properties of Cherenkov radiation. Two Ring Imaging Cherenkov detectors are used in LHCb as crucial components of the particle identification system. The requirements on their photon detection and optical systems are discussed.

The LHCb Pixel Hybrid Photon Detector (HPD) was developed to satisfy the stringent requirements on sensitivity, speed, active area coverage and spatial resolution of the LHCb RICHs. It is a vacuum tube equipped with an advanced hybrid pixel detector as anode. A review of the hybrid photon detection technology is given in the second chapter. The principles of silicon hybrid pixel detectors are then described and the LHCb Pixel HPD detailed. The results of an experimental characterization of the LHCb Pixel HPD detection performances are given at the end of the chapter.

The characteristics of the first prototypes of the LHCb Pixel HPD were evaluated in a Ring Imaging Cherenkov detector, in which the requirements of the target application were partially reproduced. The third chapter describes the experiment and the results.

The photon detectors will have to operate in the stray magnetic flux density of the LHCb magnet. The magnetic effects could spoil the spatial resolution of the devices. A satisfying solution to this problem was investigated, implemented and tested, as described in the fourth chapter.

The optical systems of the LHCb RICH detectors consist of large arrays of mirrors with high reflectivity. The mirrors and their supporting structure have to be optically precise and mechanically stable. Moreover they have to be thin and light in order not to deteriorate the performance of the experiment. The last chapter describes the solutions developed for the LHCb RICH 2 optical system in order to satisfy these requirements.

Contents

Chapter 1

LHCb Ring Imaging Cherenkov detectors

1.1 The LHCb experiment at CERN Large Hadron Collider

1.1.1 The LHCb experiment

The LHCb experiment (Fig. 1.1) has been conceived [1, 2] to study with high precision the CP violation and other rare phenomena in decays of B mesons produced by the Large Hadron Collider (LHC) at CERN. LHC will be a copious source of B mesons and then an optimal environment to host an experiment dedicated to the physics of the b quark. In order to exploit this feature, LHCb must have a highly performing event selection (*trigger*) system, based on the detection of particles with high transverse momentum (*tracking*) and displaced secondary decay vertices, and $\pi - K$ (pion-kaon) separation capability [3, 4]. The required particle identification performance is provided to LHCb by its two Ring Imaging Cherenkov (RICH 1 and RICH 2) detectors.

The layout of the LHCb experiment is shown in Fig. 1.1. It is a single arm forward spectrometer, with the LHC storage ring beam pipe passing through the apparatus. The b hadrons produced in the proton-proton collisions at the LHC energy (14 TeV) are concentrated at small polar angles [1] with respect to the beam axis. This justifies the configuration adopted for LHCb. A coordinate system is defined with the origin on the interaction point, z along the beam axis, x toward the centre of the accelerator ring and y pointing upward. The experiment covers an acceptance solid angle ± 300 mrad wide on the bending (horizontal) plane and ± 250 mrad wide on the non-bending (vertical) plane. It consists of a dipole magnet and several detectors. The magnetic field is oriented vertically and has a maximum value of 1.1 T.

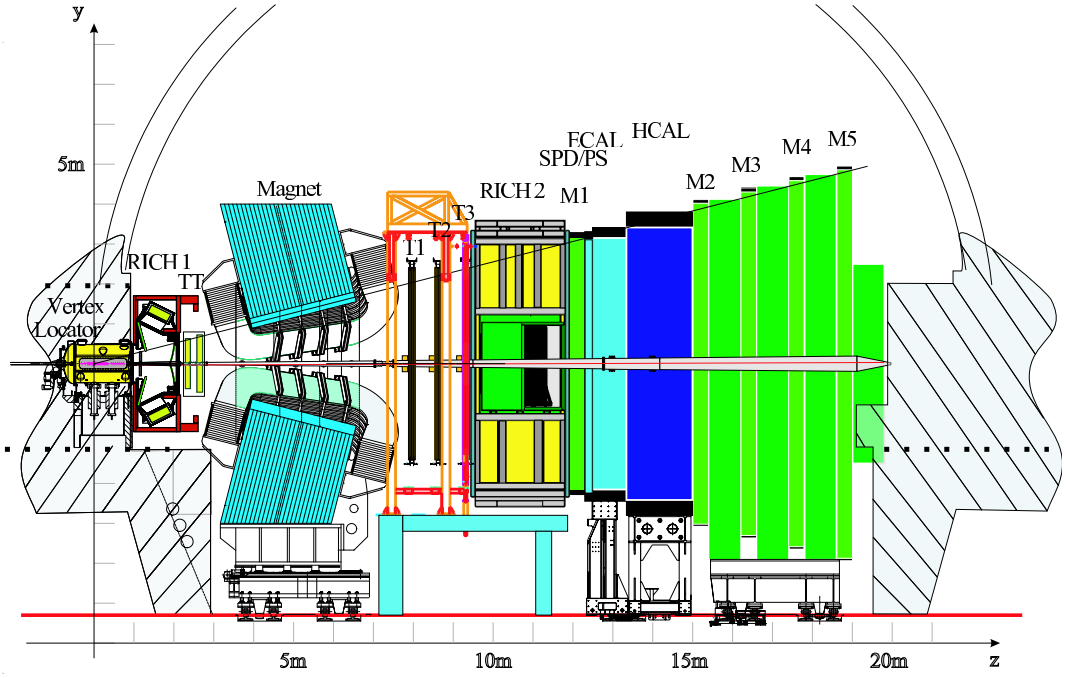

Figure 1.1: Side view of the LHCb detector (non-bending plane).

The Vertex Locator (VELO) surrounds the interaction point. It provides precise measurements of the particle tracks close to the interaction and allows the determination of secondary vertices. The RICH 1 detector and the Trigger Tracker (TT) follow it, and are located upstream the magnet. Other three tracking stations (T1, T2 and T3) are located downstream the magnet and complete the tracking system[1]. The following detectors are RICH 2 and the first station of the Muon Detector (M1-M5).

The Scintillating Pad Detector (SPD), the Preshower (PS), the electromagnetic (ECAL) and the hadronic (HCAL) calorimeters sit between muon stations M1 and M2[2]. The two RICH detectors and their specifications will be discussed in Section 1.3.

Positive identification of π and K by the RICH detectors is essential to distinguish between the final states of many decay modes of the B meson. This allows to reduce the uncertainties in the measurements of the various decay rates from which the CP asymmetry parameters are extracted. An example

[1]The trajectories of charged particles are sampled by these detectors. The momentum of the charged particles is measured by the bending radius in the magnetic field of the dipole.

[2]The calorimeters measure the energy of the particles. Electrons and gamma photons are absorbed in the ECAL, hadronic particles in the HCAL. Muons have low interaction cross section and traverse the entire detector. They are detected in the tracker and in the Muon Detector.

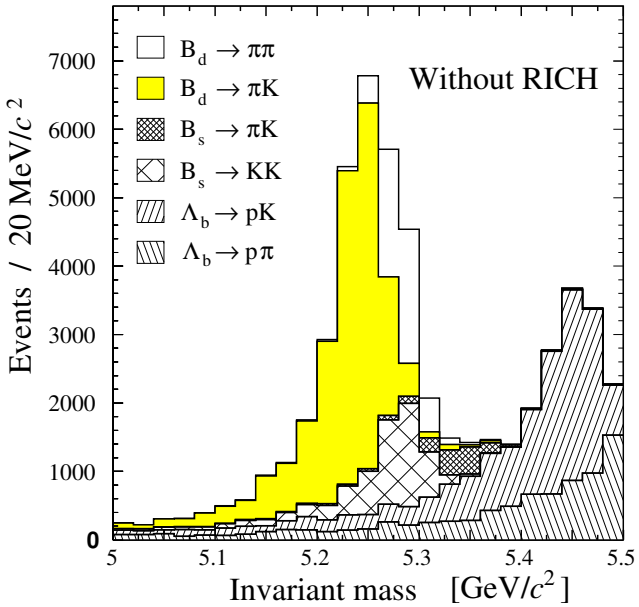

Figure 1.2: Mass spectrum of $B^0_d \to \pi^+\pi^-$ candidates before any particle identification is applied (from [3]).

of the importance of the RICH system is the measurement of CP asymmetry of $B^0_d \to \pi^+\pi^-$ decays. It requires the rejection of the background due to the decay events with the same two-body topology: $B^0_d \to K^+\pi^-$, $B^0_d \to K^-\pi^+$ and $B^0_d \to K^+K^-$. As it can be seen in Fig. 1.2 the signal from $B^0_d \to \pi^+\pi^-$ is overwhelmed by the backgrounds if particle identification is not applied.

The trigger [5] is one of the biggest challenges of the LHCb experiment. It is designed to select the B mesons through the presence of particles with large transverse momentum p_T and the existence of secondary vertices. LHCb will operate at an average luminosity of 2×10^{32} cm^{-2}s^{-1}. With this luminosity the frequency of bunch crossing containing interactions visible by the detectors is $\sim$10 MHz. Events are first filtered (Level-0 trigger) by requiring at least a lepton or a hadron with p_T exceeding 1 to 3 GeV/c. This reduces the event rate to $\sim$1 MHz. At the second trigger level (Level-1) data from the VELO and the TT station are combined with the Level-0 data, reducing the event rate to 40 kHz. These are analyzed by the High Level Trigger (HLT) which uses data of all the detectors and select events with a rate of 200 Hz. Data of the events passing the HLT decision are stored to disk. While the Level-0 trigger is implemented in full custom electronics, the Level-1 and HLT are software triggers sharing the computational power of a farm of 1800 CPUs.

1.1.2 The Large Hadron Collider at CERN

The Large Hadron Collider (LHC) is designed to accelerate and collide two counter propagating beams of protons or heavy ions [6, 7, 8]. Proton-proton collisions are foreseen at an energy E of 7 TeV per beam and with a design peak luminosity[3] $\mathcal{L} = 10^{32}$ cm^{-2}s^{-1}. The 14 TeV maximum interaction energy is one order of magnitude larger than that of the most energetic collider operated up to date[4]. The increase in luminosity is motivated by the decrease of the cross section in proportion to $1/E^2$, related to the decrease of De Broglie wavelength ($\propto 1/E$). Each of the two proton beams consists of bunches of 1.15×10^{11} particles. At peak energy their ultra relativistic speed differs by the speed of light for less than 10^{-8}. The bunch crossing rate is 25 ns and the inter-bunch spacing is 7.5 m. The transverse size of the collision area is $\sim$16 μm.

The main elements of the LHC are 1232 bending dipoles (Fig. 1.3). Each dipole is 14.3 m long and contains two vacuum pipes, one for each beam. The bending magnetic field (8.4 T) is generated by a current of 11700 A flowing into superconductive coils operating at 1.9 K and surrounding the vacuum pipes (Fig. 1.4). Liquid helium cryogenics is employed in the entire machine. LHC is planned to start operation in 2007 and it is being installed at CERN in the $\sim$27 km long underground tunnel, in which the LEP collider was formerly located.

The experimental test of supersimmetry [9] and of the Higgs mechanism (Higgs boson [10, 11]) for the explanation of mass are among the goals of the ATLAS (A Toroidal LHC Apparatus [12, 13]) and CMS (Compact Muon Solenoid [14]) detectors that will operate at LHC. The LHCb experiment is dedicated to CP violation and the physics of the B meson. The ALICE (A Large Ion Collider Experiment [15]) is dedicated to the physics of quark-gluon plasma and will exploit the LHC capability to collide heavy (Pb) ions.

CERN is the European Organization for Nuclear Research, the world's largest laboratory[5] for research in particle physics. Its mission is to serve science in conceiving and providing research tools, expertise and infrastructure for research. The results of its research and technological development activity are entirely of public domain. Twenty European countries, the Member States,

[3] The cross section σ [cm^2] is used to express the probability of interactions between elementary particles. Given two colliding beams the rate of interactions R_{int} is given by $R_{int} = \sigma\mathcal{L}$, where $\mathcal{L}$ [cm^{-2}s^{-1}] is the collider luminosity. $\mathcal{L} = N_1N_2/(A\Delta t)$ where N_1 and N_2 are the particles in each beam crossing a section A during a time interval Δt.

[4] Fermilab's Tevatron, a 1 TeV proton-antiproton collider. The HERA (Germany) electron-proton collider reaches $\sim$310 GeV. The CERN Large Electron Positron (LEP) collider reached 104 GeV before its shut down at the end of 2000.

[5] The laboratory is located at the border between Switzerland and France, close to the city of Geneva.

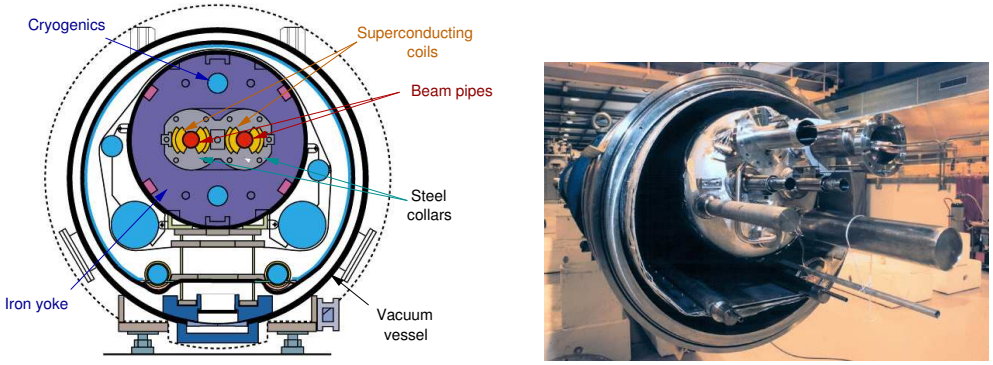

(a) (b)

Figure 1.3: Large Hadron Collider dipole. 1.3(a) Schematic view of the main dipole elements. 1.3(b) Photograph of one of the 1232 dipoles inside its vacuum vessel (CERN copyright).

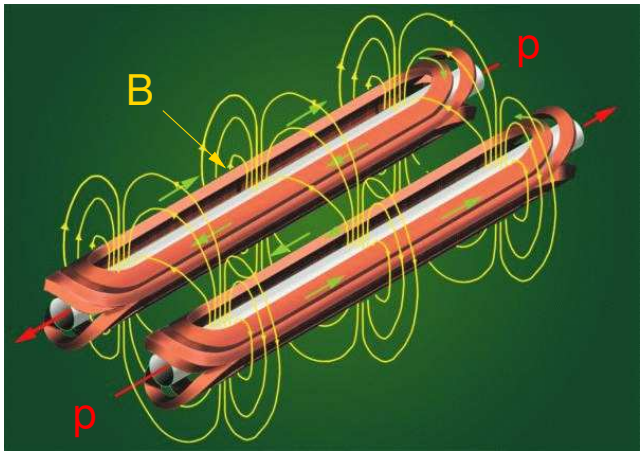

Figure 1.4: A sketch of the LHC dipoles beam pipes surrounded by the superconducting coils. The bending magnetic field lines are shown (CERN copyright).

fund and make use of the laboratory through their research institutions. Italy is the fourth contributor to CERN yearly total budget of around 700 million euros.

CERN accelerators are used by scientists of external research institutions for their experiments. The experiments use particle detectors to investigate the phenomena occurring in the interactions of highly energized particles of matter. These include the artificial creation of unstable particles that quickly decay in stable particles. CERN joins the collaborations realizing the experiments and participates in the construction and running of the detectors.

The realization of advanced accelerators and detectors pushes technological development and the advances have strong impact on society[6]. Progresses in material science, vacuum technology, cryogenics, superconductive materials are continuously realized, in partnership with industry. Computer science and data networking science are stimulated by the needs of collection, real time processing and analysis of the experimental data[7].

CERN promotes advanced education and training. The research activity described in this thesis was realized in the framework of the CERN Doctoral Program, open to doctoral students of Member States.

1.2 Cherenkov detectors

1.2.1 Cherenkov radiation

An electrically charged particle crossing a medium causes the emission of electromagnetic radiation when traveling with a speed larger than the phase velocity of light in that medium. This radiation is called Cherenkov radiation after the accurate experimental characterization of its properties done by P. Cherenkov [16]. A model describing the properties of the radiation was first published by Frank and Tamm [17]. The three shared the 1958 Nobel Prize for physics [18] for their discoveries. Cherenkov radiation is at the basis of various particle identification techniques in the field of high energy physics [19, 20].

Figure 1.5(a) represents the charged particle traveling in a medium of index of refraction n and the emission of a photon by Cherenkov effect.

[6] Accelerators and detection technologies are currently employed in medicine for diagnosis (X-ray Computed Tomography, Positron Emission Tomography), therapy (radiotherapy, hadrontherapy) and production of radio-pharmaceuticals.

[7] The http protocol was invented by Tim Berners Lee at CERN in 1989. It was chosen not to patent the invention. The first GRID protocols were created and are being developed at CERN. GRID computing is a new computational model to provide transparent, extensible and secure access to all resources distributed in a computer network, including computational power.

Basic properties of Cherenkov radiation can be derived by the conservation laws of momentum and energy. The total energy and momentum of a relativistic particle are given by

$$E = mc^2 = \sqrt{p^2c^2 + (m_0c^2)^2} \tag{1.1a}$$

$$\mathbf{p} = m\mathbf{v} = m_0\gamma\beta c\hat{\mathbf{u}}_v \tag{1.1b}$$

respectively. In previous equations m and m_0 are the mass and the rest mass of the particle, while

$$\beta = \frac{v}{c} \tag{1.2a}$$

$$\gamma = \frac{1}{\sqrt{1-\beta^2}} \tag{1.2b}$$

are the speed of the particle relative to the speed of light in vacuum c and the Lorentz factor. Vector $\hat{\mathbf{u}}_v$ is the unit vector of the particle vector velocity.

E_1, $\mathbf{p}_1$ and E_2, $\mathbf{p}_2$ are the energies and momenta of the particle before and after the emission of the photon. The relative loss of energy of the particle is very small: the energy of the photon in the visible or UV spectrum is negligible with respect to the energy of the relativistic particle. In the same way it is $\mathbf{p}_2 \simeq \mathbf{p}_1 = \mathbf{p}$.

Eq. (1.1a) expansion in series, truncated to first order, gives:

$$E_2 \simeq E_1 + \frac{\partial E}{\partial \mathbf{p}} \cdot \Delta\mathbf{p} = E_1 + c^2\frac{\mathbf{p}_1}{E} \cdot (\mathbf{p}_2 - \mathbf{p}_1)\,. \tag{1.3}$$

Introducing the expression of energy and momentum of the photon, the conservations laws for the process are

$$E_1 = \hbar\omega + E_2 = h\nu + E_2 \tag{1.4a}$$

$$\mathbf{p}_1 = \mathbf{p}_2 + \hbar\mathbf{k}. \tag{1.4b}$$

After substitution in Eq. (1.3), it results:

$$\hbar\omega = c^2\frac{\mathbf{p}}{E} \cdot \hbar\mathbf{k}. \tag{1.5}$$

The dispersion law of the medium written in terms of the wavenumber is:

$$k = n(\omega)\frac{\omega}{c}. \tag{1.6}$$

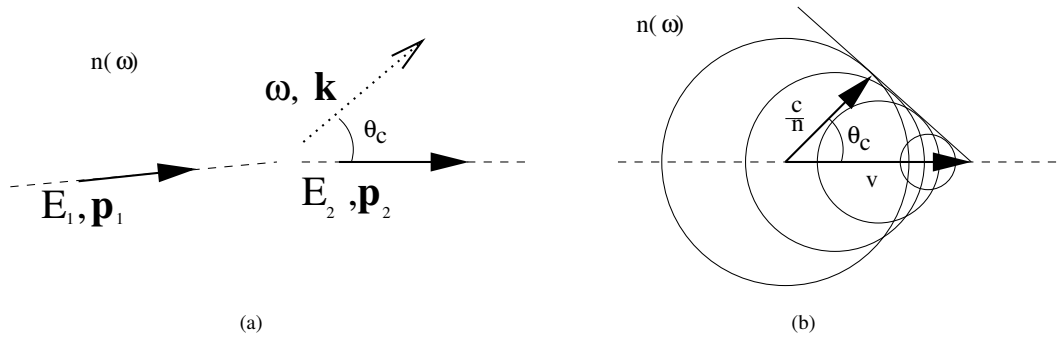

Figure 1.5: (a) The emission of a Cherenkov photon by a charged particle. (b) The geometrical construction for a determination of the Cherenkov angle.

and final substitution of Eq. (1.6) into Eq. (1.5) gives:

$$\cos\ \theta_c = \frac{1}{n(\omega)\beta}. \tag{1.7}$$

The Cherenkov angle is the angle θ_c between the velocity vector of the charged particle $\mathbf{v}$ and the momentum vector $\mathbf{k}$.

A classical electrodynamics treatment [21], [22] gives the same result. In this approach the traveling charged particle generates a perturbation of the dielectric medium that can be described with a transient electric polarization $\mathbf{P}(\mathbf{x}, t)$. Cherenkov radiation is then resulting as the far field superposition of the field irradiated by the continuous of dielectric dipoles constituting the medium. Eq. (1.7) is the condition of constructive interference.

An intuitive insight in this approach is given by Fig. 1.5(b). The spherical waves originating at the passage of the particle and propagating with speed c/n, coherently interfere on a conical surface. The angle between the trajectory of the particle and the direction of propagation of the wave front satisfies Eq.(1.7).

Three important properties of Cherenkov radiation are expressed by Eq. (1.7):

- In order to have the emission of photons the speed of the charged particle has to be larger than a *threshold speed*:

$$\beta > \beta_{thresh} = \frac{1}{n(\omega)}. \tag{1.8}$$

  The particle has to be faster than the phase velocity of light in the medium.

- The emission angle of a photon of a given wavelength is determined by the speed of the particle and by the index of refraction of the medium at that wavelength.

- For a given photon wavelength there exists a maximum (*saturation*) emission angle defined by the condition $\beta = 1$:

$$\theta_{sat} = \arccos \frac{1}{n(\omega)}. \tag{1.9}$$

The number of photons emitted in the spectral range dE per unit length of radiator is given by the Frank-Tamm relation:

$$\frac{d^2N}{dEdx} = \frac{\alpha Z^2}{\hbar c} \sin^2 \theta_c(E) \tag{1.10}$$

in which Z is the charge of the particle in units of e and α is the fine structure constant:

$$\alpha = \frac{e^2}{4\pi\epsilon_0 \hbar c} = \frac{1}{137}. \tag{1.11}$$

The energy spectral distribution of Cherenkov radiation would be constant if there were not dispersion. This is put in evidence in Eq. (1.10) by the dependence of the emission angle on the energy of the photon.

In a Cherenkov detector the photons are recorded by conversion into electric charge, i.e. in an electric signal, after collection and focusing with some optical system.

To determine the number of detectable photoelectrons one has to consider:

- the losses due to absorption in the radiator medium in which photons propagate;
- the reflection losses in the optics to collect and focus the photons;
- the conversion efficiency of the photon detectors employed.

Neglecting the angle variations due to the medium dispersion and assuming that the dielectric loss angle is very small[8], the total number of detected photoelectrons is obtained integrating Eq. (1.10) over energy:

$$N_{pe} = N_0 Z^2 L \sin^2 \theta. \tag{1.12}$$

where L is the length of the radiator medium and N_0 is the *detector response parameter*:

$$N_0 = \left(\frac{\alpha}{\hbar c}\right) \Delta E = \ 370[(\text{eV} \cdot \text{cm})^{-1}] \cdot \Delta E \tag{1.13a}$$

[8]The integration range $[E_1, E_2]$ in Eq. (1.13b) is below the plasma frequencies so that for the dielectric permittivity $\epsilon = \epsilon_r - \jmath\epsilon_i \simeq \epsilon_r$, being $\epsilon_i \ll \epsilon_r$.

$$\Delta E = \int_{E_1}^{E_2} R(E)T(E)QE(E)dE. \tag{1.13b}$$

ΔE is the factor taking into account the losses due to reflections on light collecting optics (R), the optical transmission losses (T) and the detector quantum efficiency (QE). E_1 and E_2 are a lower and upper limit of the range of sensitivity of the photon detectors.

As an order of magnitude calculation, let us assume $R = 0.9$, $T = 1$. With a typical quantum efficiency curve of the HPD photon detector (Fig. 2.21, page 56) one obtains $\Delta E \simeq 0.5$ and $N_0 \simeq 185$ cm^{-1}. Considering N_2 as gas radiator ($n \simeq 1.0003$) it results $\theta_{sat} = 24$ mrad and from Eq. (1.12) the average number of photoelectrons expected per meter of radiator length would be $N_{pe} \simeq 11$ m^{-1}.

The former calculation shows the need of a photon detection system that is highly efficient for single photons.

The photon emission yield can also be expressed as a function of wavelength since:

$$\sin^2\theta_c(\lambda) = 1 - \cos^2\theta_c(\lambda) = 1 - \frac{1}{n^2(\lambda)\beta^2}. \tag{1.14}$$

Taking into account Planck-Einstein's relation $E = h\nu$ one gets

$$dE = \frac{\partial}{\partial\lambda}\left(\frac{hc}{\lambda}\right)d\lambda = -\frac{hc}{\lambda^2}d\lambda. \tag{1.15}$$

Substitution of the previous two equations into Eq. (1.10) gives the number of photons per unit of photon wavelength:

$$\frac{d^2N}{d\lambda dx} = \frac{2\pi\alpha Z^2}{\lambda^2}\left(1 - \frac{1}{\beta^2 n^2(\lambda)}\right). \tag{1.16}$$

Referring to symbols introduced in Eq. (1.13), the average number of expected photoelectrons generating from photons in the wavelength interval $(\lambda, \lambda + d\lambda)$ is given by:

$$\frac{d^2N_{pe}}{d\lambda dx} = \frac{d^2N}{d\lambda dx}R(\lambda)T(\lambda)QE(\lambda). \tag{1.17}$$

The distribution of photoelectrons as a function of the photon emission angle is:

$$\frac{d^2N_{pe}}{d\theta dx} = \frac{d^2N_{pe}}{d\lambda dx}\frac{d\lambda}{d\theta} = \frac{d^2N_{pe}}{d\lambda dx}\frac{\beta n^2\sin\theta}{\frac{\partial n}{\partial\lambda}} \tag{1.18}$$

in which the index of refraction and its derivative must be evaluated at the λ corresponding to θ from Eq. (1.7).

Finally, integration of Eq. (1.17) over wavelength gives:

$$N_{pe} = 2\pi Z^2 \alpha L \int_\lambda \frac{1}{\lambda^2} \left(1 - \frac{1}{n^2(\lambda)\beta^2}\right) R(\lambda)T(\lambda)QE(\lambda)d\lambda \tag{1.19}$$

which, compared to Eq. (1.12), takes into account the dispersion of the medium. Eq. (1.19) will be used in the following chapters for calculating the expected number of photoelectrons generated in the experiments.

1.2.2 Particle kinematics and particle identification

The relative speed β of a relativistic particle can be determined from the scalar version of Eq. (1.1b):

$$p = mv = mc\beta = m_0 c\gamma\beta. \tag{1.20}$$

It results:

$$\beta = \frac{1}{\sqrt{1 + \left(\frac{m_0 c}{p}\right)^2}}. \tag{1.21}$$

By choosing the units such that $c = 1$ and consequently expressing mass in GeV/c^2 and momentum in GeV/c, the following truncated expansion of Eq.(1.21) can be used when $m_0 \ll p$:

$$\beta = \frac{1}{\sqrt{1 + \left(\frac{m_0}{p}\right)^2}} \simeq 1 - \frac{1}{2}\left(\frac{m_0}{p}\right)^2. \tag{1.22}$$

From Eq. (1.20) the rest mass of a particle can be determined once its momentum and its β are known[9]. The identification of the particle is achieved once its rest mass is known. The relative uncertainty σ_{m_0}/m_0 of the rest mass due to the uncertainties of the momentum (σ_p) and Cherenkov angle (σ_θ) measurements can be obtained from Equations. (1.7) and (1.20):

$$\frac{\sigma_{m_0}}{m_0} = \sqrt{\gamma^2 \tan^2(\theta)\sigma_\theta^2 + \frac{\sigma_p^2}{p^2}}. \tag{1.23}$$

Fig. 1.6 shows the Cherenkov angles, for two species of particles and in two different radiators, as a function of momentum. It illustrates the principle of particle identification by Cherenkov radiation. The type of particles, the momentum range, the difference in emission angle and the angular resolution govern the choice of the radiators.

[9]The momentum is determined by the curvature of the particle track in a known magnetic field. The relative speed is determined by the Cherenkov angle using Eq. (1.7).

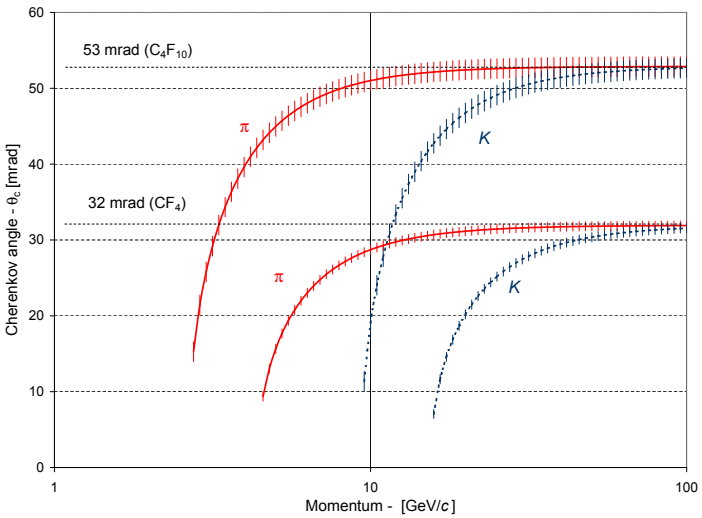

Figure 1.6: Cherenkov emission angle vs. particle momentum. Plots refer to two types of particles (pions and kaons) and two radiators (C_4F_{10} nd CF_4). The threshold onset of Cherenkov radiation as well as the asymptotic value of the Cherenkov angle for $\beta \to 1$ are shown. The error bars give an indication of the error on the measurement of the Cherenkov angle (1 σ).

1.2.3 Common gas radiators and indexes of refraction

Eq. (1.7) and Eq. (1.10) show that an accurate knowledge of the index of refraction of the radiator is essential for the operation of a detector of Cherenkov radiation.

Gas radiators are often used. A single pole Sellmeier formula can describe the index of refraction with enough accuracy in many of these cases:

$$(n-1)\cdot 10^6 = \frac{A}{\lambda_0^{-2}-\lambda^{-2}}. \tag{1.24}$$

Values of the constants for a few gases are given in Table 1.1.

For an isotropic molecular gas at low density ($n \simeq 1$) it can be shown [24] that (n^2-1) is proportional to the gas density ρ. Given that $(n^2-1) \simeq 2(n-1)$, the index of refraction at pressure p [Pa] and temperature T [K] is obtained from:

$$(n(p,\mathrm{T})-1)\cdot 10^6 = \frac{A}{\lambda_0^{-2}-\lambda^{-2}} \cdot \frac{p}{101325} \cdot \frac{273.15}{\mathrm{T}}. \tag{1.25}$$

Gas	A	λ_0 [nm]
N_2	0.053191	74.36
O_2	0.027583	97.28
Ar	0.050854	73.82
CO_2	0.068681	80.10
CF_4	0.12489	61.8
C_4F_{10}	0.25324	73.6

Table 1.1: Values of parameters of Eq. (1.24) for some common gases at 0 °C and 101325 Pa, from ref. [23].

1.2.4 Types of Cherenkov detectors

Cherenkov detectors can be based on one or more of the discussed properties of Cherenkov radiation. Three types of detectors can be distinguished on this basis [20]:

1. Threshold detectors: charged particles with relative speed greater than β_{thresh} radiate Cherenkov photons. The threshold can be set by tuning the index of refraction of the radiator medium, for example by changing the pressure of a gaseous radiator.
2. Differential detectors: optical focusing and masking of the radiation are used to select particles with velocities in a given range.
3. Ring imaging Cherenkov detectors [25, 26]: Cherenkov photons are focused onto position sensitive photon detectors in ring like patterns, whose radii depend on the Cherenkov angle. Hypothesis on the particle identity are tested against the ring radius.

The Cherenkov photons are generally focused on the photon detectors by the proximity focusing technique or by reflection on mirrors with quadric surfaces. The basic principle of Ring Imaging Cherenkov detection is shown in Fig. 1.7.

1.3 LHCb Ring Imaging Cherenkov detectors

1.3.1 General description

The LHCb experiment has two RICH detectors providing positive kaon identification capability over the wide momentum range 2-100 GeV/c. Two detectors (Fig. 1.8) are used due to the strong correlation between the momentum and the polar angle of the decay products in B decays [3]. The RICH 1 is located upstream the magnet (Fig. 1.1). It covers the full angular acceptance

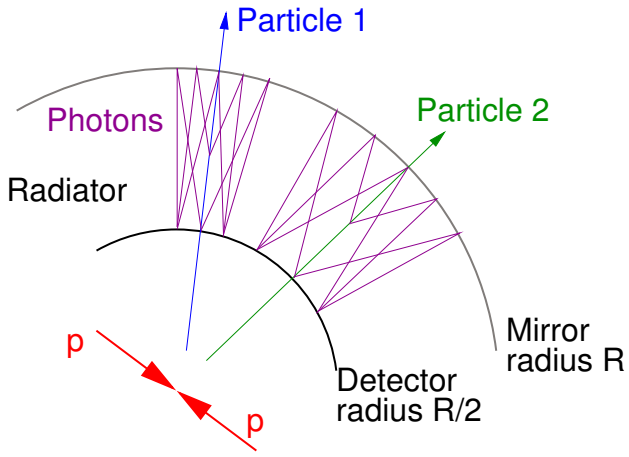

Figure 1.7: Scheme of the Ring Imaging Cherenkov detection technique. Particles cross the radiator with different speeds and Cherenkov photons are emitted along the tracks at the angle given by Eq. (1.7). They are reflected on a mirror and focused onto position sensitive photon detectors. The radii of the rings projected on the detectors depend on the particle speed.

of the experiment and is optimized for lower momentum (2-60 GeV/c) particles. RICH 2 follows the magnet, receding from the interaction point. Its coverage is limited to a solid angle of 120 mrad×100 mrad (horizontal and vertical dimensions) where the highest momentum particles (16-100 GeV/c) are abundant.

The LHCb RICH detector complex uses 3 radiators. A 5 cm thick silica aerogel (n$\simeq$1.03 at 400 nm) and a 0.85 m thick C_4F_{10} gas radiator (n$\simeq$1.0014 at 400 nm) are employed in RICH 1. RICH 2 has a 2 m thick radiator volume of CF_4 gas (n$\simeq$1.0005 at 400 nm).

RICH 1 and RICH 2 share a similar optical design as shown in Fig. 1.9. Spherical reflective surfaces focus the Cherenkov photons onto the photodetectors. In order to have the detection planes outside the acceptance of the spectrometer, a second surface of flat mirrors is interposed between the spherical mirrors and the photodetectors. Each RICH has two planes of photodetectors.

Both RICH 1 and RICH 2 are located in the fringe field of the LHCb magnet. The photon detectors are contained inside magnetic shielding boxes of high magnetic permeability iron. The design of the boxes is such that the peak magnetic flux density inside them is less than 2.5 mT in RICH 1 and less than 1.0 mT in RICH 2.

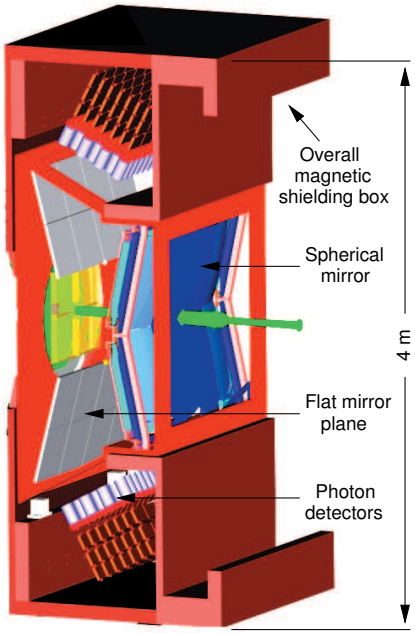

(a) RICH 1

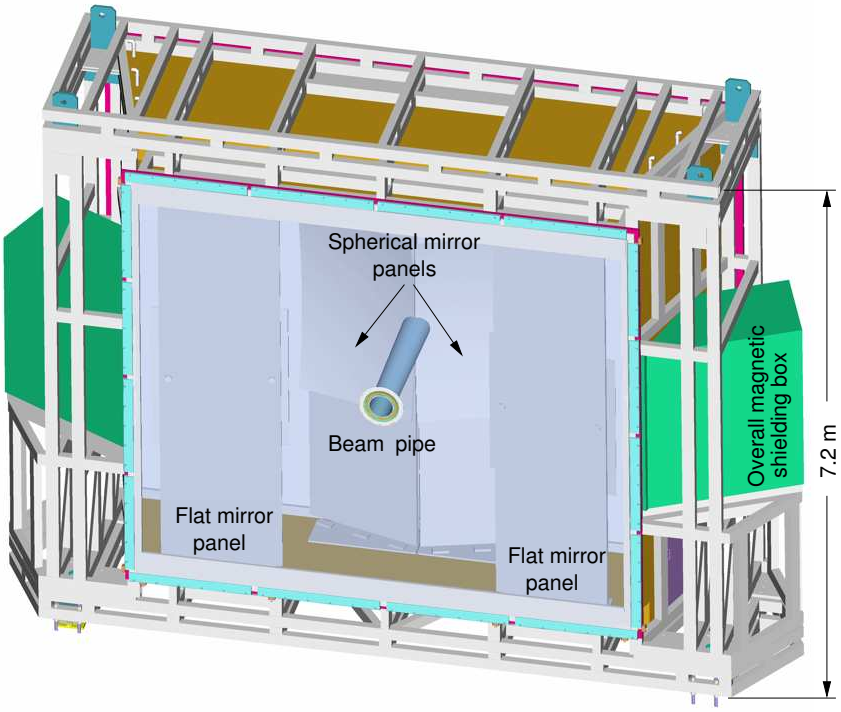

(b) RICH 2

Figure 1.8: The LHCb RICH detectors.

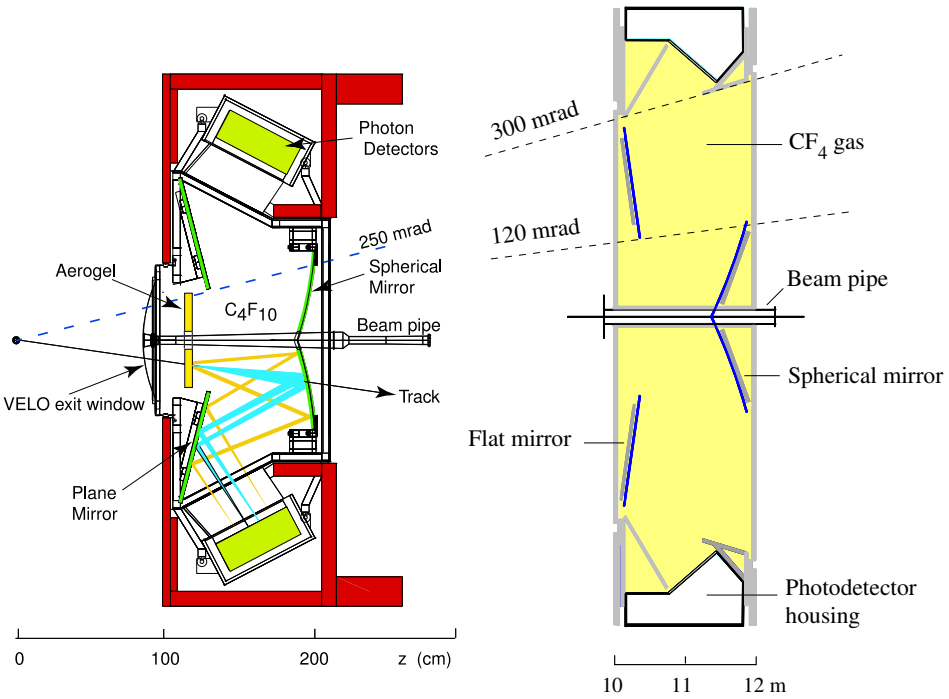

Figure 1.9: RICH 1 (left) and RICH 2 (right) detectors schemes. Scales are different, RICH 1 is viewed from the side (x), RICH 2 is viewed from the top (y). The spherical and flat mirrors collect and focus the Cherenkov photons on the photon detectors. Plates of fused silica in front of the photodetector housings seal the gas vessels (not shown).

1.3.2 Reconstruction of the Cherenkov angle: sources of uncertainty

The photon hit position on the detection plane and the corresponding track information are used to reconstruct the Cherenkov emission angle. The photon hit is geometrically traced back to the middle point of the track in the radiator, assumed as the emission point. In general, the performance of RICH detectors relies on the accuracy of the tracking system for the measurements of particle momentum and coordinates (cf. Section 1.2.2).

The identification of the particle is based on the calculation of a likelihood function for each particle type hypothesis, namely:

$$P_x = \sum_i \ln \left[1 + \frac{1}{\sqrt{2\pi}\sigma_\theta} \exp\left(-\frac{(\theta_i - \theta_x)^2}{2\sigma_\theta^2} \right) \right] \tag{1.26}$$

where θ_i is the angle reconstructed for the i-th hit, θ_x is the angle expected under the given particle type hypothesis and σ_θ is the angular resolution. The particle type maximizing the conditional probability is assigned to the track.

The particle identification efficiency is affected by the angular resolution of the detector (σ_θ). This is limited by basic factors even assuming an ideally perfect optical system. The spatial resolution of the photon detectors has been chosen as 2.5×2.5 mm^2 based on a balance with the other sources of uncertainty. A smaller pixel size would give little benefit and imply increased complexity and cost. The different sources of uncertainties are listed in Table 1.2 for the two RICH detectors.

The photons are actually emitted all along the trajectory in the radiator and with a range of energies, i.e. a range of emission angles (cf. Eq. 1.7). Both informations are not available for the reconstruction and this gives rise to the emission and the chromatic error. The finite detector pixel size and the tracking error affect the determination of the photon hit position and the calculation of the angle. Finally the expected angle θ_x is determined using the momentum measured by the tracking system, then the identification algorithm is also affected by the error of the momentum measurement, even if this does not enter explicitly Eq. (1.26).

1.3.3 Radiation length and interaction length

As is generally true for all particle detectors apart from calorimeters, the RICH detectors should not introduce any matter that might influence the motion of the particles. The interactions between a particle and matter result in angular

Uncertainty		RICH 1		RICH 2
		Aerogel	C_4F_{10}	CF4
$\sigma_\theta^{emission}$	[mrad]	0.29	0.69	0.31
$\sigma_\theta^{chromatic}$	[mrad]	1.61	0.81	0.42
σ_θ^{pixel}	[mrad]	0.62	0.62	0.18
σ_θ^{track}	[mrad]	0.52	0.40	0.20
σ_θ^{total}	[mrad]	1.82	1.29	0.58

Table 1.2: The various contributions to the uncertainty of the Cherenkov angle reconstruction in the LHCb RICH detectors.

scattering and energy loss. They are quantified by the radiation length X_0 [10] and by the interaction length λ_0 [11]. The multiple scattering angle θ_{ms} is given by

$$\langle \theta_{ms}^2 \rangle \propto \frac{dx}{X_0}. \tag{1.27}$$

The particle might undergo showering in addition to scattering or, in the case of kaons and pions, interact with nuclei before traversing the complete tracking system. The number of reconstructed events would therefore decrease and the occupancy of the detector systems increase. The detector efficiency in selecting and measuring the rates of the interesting B mesons decays would be affected.

The amount of material which is not required for the Cherenkov radiation, the dead detector material, should be much smaller than the radiator material itself when measured in units of radiation and interaction length. The total fractional radiation length of the Cherenkov radiators is 0.059 in RICH 1 and 0.02 for RICH 2.

The total radiation length for RICH 2 has been defined to be less than 0.124 of X_0. This number, comparatively large with respect to the fraction due to the radiator, can be tolerated as RICH 2 is the last detector in front of the calorimeter complex and the muon chambers. It corresponds to a relative energy loss of $1 - e^{-0.124} = 11.7\%$.

The specification is stricter for RICH 1, requiring a total radiation length less than 0.08 of X_0 [2]. The contribution of the radiators is predominant for RICH 1.

[10] The radiation length quantifies the energy losses due to electromagnetic interaction. It is defined as the average length of material over which high energy electrons lose energy by *bremsstrahlung* to $1/e$ of the initial value. *Bremsstrahlung* means braking radiation: electrons emit photons and lose energy being accelerated (deflected) in the Coulomb field of the nuclei in the material.

[11] The interaction length quantifies the interactions of hadronic particles with nuclei. It is defined by analogy with the interaction length but considering elastic or inelastic interactions with nuclei due to the strong force.

1.3.4 Specifications on the photodetectors and the optical system

The particle identification performance critically depends on the number of detected photons for each particle and on the accuracy of the determination of the photon hit position. The photodetectors must provide single photon detection capability with high quantum efficiency and a spatial resolution of 2.5×2.5 mm^2. The large total photodetection surface ($\sim$2.6 m^2) of the LHCb RICHs has to be covered with array of photodetectors with the largest possible fraction of active area. The photodetectors must operate in the residual magnetic field inside the shielding boxes without loss of detection efficiency nor spatial resolution. These stringent requirements are satisfied by the LHCb Pixel Hybrid Photon Detector (Chapters 2, 3 and 4).

The large mirror surfaces have to be highly reflective to avoid photon losses. In addition, the optical system has to be perfectly aligned for an accurate reconstruction of the Cherenkov angle (cf. the discussion of Eq. (1.26)). The mirror support system must therefore allow a precise alignment and long term stability. On the other hand the mirrors and their supports must be extremely light to satisfy the constraint on the amount of material introduced by the RICH detectors in the LHCb acceptance (Section 1.3.3). The reader is referred to Chapter 5 for further details.

Bibliography

[1] LHCb Collaboration, "LHCb Technical Proposal", CERN, Tech. Rep. CERN/LHCC 1998-004, February 1998.

[2] LHCb Collaboration, "LHCb Technical Design Report, Reoptimized Detector Design and Performance", CERN, Tech. Rep. CERN/LHCC 2003-030, LHCb TDR 9, September 2003.

[3] LHCb RICH Collaboration, "LHCb RICH Technical Design Report TDR", CERN, Tech. Rep. CERN/LHCC 2000-037, September 2000.

[4] O. Ullaland for the LHCb RICH collaboration, "Ring Imaging CHerenkov Detectors and their application in LHCb", 2005, to be published in Frascati Physics Series.

[5] LHCb Collaboration, "LHCb Trigger System Technical Design Report TDR", CERN, Tech. Rep. CERN/LHCC 2003-031, LHCb TDR 10, September 2003.

[6] O. S. Bruning, *et al.*, Eds., *"LHC Design Report vol. 1: the LHC Main Ring"*. CERN, 2004, vol. 1, CERN-2004-003-V-1.

[7] O. S. Bruning, *et al.*, Eds., *"LHC Design Report vol. 2: the LHC infrastructure and General Services"*. CERN, 2004, vol. 2, CERN-2004-003-V-2.

[8] M. Benedikt, *et al.*, Eds., *"LHC Design Report vol. 3: the LHC Injector Chain"*. CERN, 2004, vol. 3, CERN-2004-003-V-3.

[9] S. Weinberg, *The Quantum Theory of Fields, Volume 3: Supersymmetry.* Cambridge University Press, Cambridge, 1999.

[10] P. W. Higgs, "Broken symmetries, massless particles and gauge fields", *Phys. Lett.*, vol. 12, no. 2, pp. 132–133, September 1964.

[11] P. W. Higgs, "Broken symmetries and the masses of gauge bosons", *Phys. Rev. Lett.*, vol. 13, no. 16, pp. 508–509, October 1964.

[12] ATLAS Collaboration, *"ATLAS Detector and Physics Performance: Technical Design Report, 1"*, 1999, vol. 1, ATLAS-TDR-014, CERN-LHCC-99-014.

[13] ATLAS Collaboration, *"ATLAS Detector and Physics Performance: Technical Design Report, 2"*, 1999, vol. 2, ATLAS-TDR-015, CERN-LHCC-99-015.

[14] CMS Collaboration, *"CMS, the Compact Muon Solenoid: technical proposal"*, 1994, CERN-LHCC-94-38.

[15] ALICE Collaboration, *"ALICE: Technical Proposal for a Large Ion Collider Experiment at the CERN LHC"*, 1995, CERN-LHCC-95-71.

[16] P. Cherenkov, *Dokl. Akad. Nauk SSSR*, vol. 21, p. 651, 1937.

[17] I. Frank and I. Tamm, *Dokl. Acad. Nauk SSSR*, vol. 14, p. 107, 1937.

[18] "1958 Nobel Prize for physics, laureates lectures", http://nobelprize.org/physics/laureates/1958/cerenkov-lecture.pdf, http://nobelprize.org/physics/laureates/1958/frank-lecture.pdf, http://nobelprize.org/physics/laureates/1958/tamm-lecture.pdf.

[19] J. V. Jelly, *Cherenkov Radiation and its applications*. Pergamon, London, 1958.

[20] J. Séguinot, "Les compteurs Cherenkov: applications et limites pour l'identification des particules. Développements et perspectives", vol. CERN EP/89-92, LPC/89-25, 1989, cours donné à l'École Joliot-Curie 1988, Maubouisson, France, 25-30 Septembre.

[21] J. D. Jackson, *Classical Electrodynamics*, 3rd ed. John Wiley & Sons, 1998.

[22] J. A. E. Roa-Neri, *et al.*, "Induced time-dependent polarization and Cherenkov effect", *European Journal of Physics*, vol. 16, pp. 191–194, 1995.

[23] O. Ullaland, "Refractive index, Transparency and other Interesting Subjects", September 2003, private communication.

[24] M. Born and E. Wolf, *Principles of Optics*, 7th ed. Cambridge University Press, 1999.

[25] J. Séguinot and T. Ypsilantis, "Photo-ionization and Cherenkov Ring Imaging", *Nucl. Instr. and Meth.*, vol. 142, pp. 377–391, 1977.

[26] T. Ypsilantis and J. Séguinot, "Development of Ring Imaging Cherenkov counters for particle identification", vol. LPC/94-48, 1994.

Chapter 2

The LHCb Pixel Hybrid Photon Detector

2.1 Single photon detectors

The LHCb Pixel Hybrid Photon Detector is an advanced type of Hybrid Photon Detector, specially developed to fulfill the requirements of the LHCb RICH detectors. It is a position sensitive detector with single photon sensitivity. Fig. 2.1(a) shows a picture of the device. The location of the photon entering the device active window can be determined with an equivalent pixel size of about 2.5×0.31 mm^2.

This chapter gives a description of the LHCb Pixel HPD. The aim is to provide a rather self contained discussion of the working principles of the HPD, of its anode assembly and of the performance figures. The motivations for an in-depth experimental characterization of this novel device will be given. Section 2.2 gives a general description of the Hybrid Photon Detector technology. The LHCb Pixel HPD is detailed in the following section, with special attention to the advanced pixel hybrid detector constituting the tube anode.

The results of the experimental activity are presented at the end of this chapter as well as in the following chapters 3 and 4.

It is worthwhile to introduce the Hybrid Photon Detectors as compared to some other technologies capable of detecting single quanta of light: vacuum tubes and semiconductor detectors. In traditional vacuum devices (electron tubes) the photon is absorbed by a sensitive photocathode and an electron is released by photoemission. This charge signal must be amplified to a detectable level. The primary electron is first accelerated by an electrostatic field. Then secondary emission of electrons in special structures is used to achieve multiplication of the number of charge carriers. A cascade multiplication process provides extremely high gain, reaching commonly 10^5-10^6. A chain of dyn-

odes, electrodes coated with special semiconductors, or micro-channel plates are employed in the photomultiplier tube (PMT) and in Image Intensifiers.

The technology of vacuum tubes is mature. The PMT was invented at RCA in 1936. Significant progresses in PMTs date to the 1960s, but the technology is still evolving and remains advantageous in many applications. Developments of photocathode technologies are ongoing: GaAsP cathodes deposited with Ultra High Vacuum Molecular Beam Epitaxy reach peak quantum efficiencies of almost 50% [1]. Position sensitive photomultipliers (Multi Anode PMTs) recently appeared, offering imaging capabilities together with single photon sensitivity. A recent breakthrough is the flat panel MaPMT with a 5×5 cm^2 active area in a square package only few mm thick and a dead area of less than 1 mm around the periphery [1].

During last decades various type of semiconductor devices capable of single photon detection have been investigated and developed [2] and research is actively ongoing. Excellent photon-electron conversion efficiency is offered by silicon, but signal amplification by avalanche multiplication in the material is required to obtain a detectable signal from the single e-h pair generated by the absorption of a photon. The performance of these devices is limited by the amplification of the thermally generated charge and of the reverse bias current, often requiring cryogenic cooling for proper operation. Recent developments like the electron bombardment CCD provide better immunity to noise and imaging capability, but they are limited in readout speed.

A Hybrid Photon Detector (HPD) is an electron tube. The basic concept dates back to 1957 but significant advances were achieved in the 1990s exploring the advantages offered by silicon sensors [3, 4]. Single photon counting capability, large dynamic range, position sensitive photon detection were pursued. Fig. 2.1(b) illustrates the operating principle of an HPD. A photocathode is deposited on the internal surface of a transparent entrance window. The electron resulting from the absorption of a photon traversing the window and reaching the photoemissive layer is then accelerated in a high potential drop (∼15-25 kV) electrostatic field. The energized electron hits a silicon sensor acting as the anode of the HPD. Charge carriers in the silicon sensors are generated by this *electron bombardment* and constitute the detectable signal.

While the technologies of the photocathode and of the electron optical system are inherited from vacuum tubes, the silicon anode is the specific characteristic of a HPD. It gives the HPD a single-photon resolution[2] much improved over the traditional vacuum tubes (Section 2.2.3). The hybrid denomination comes from this combination of the two technologies. If the silicon sensor is a pixel sensor, the HPD is a position sensitive device with imaging capabilities,

[1] Hamamatsu Photonics, http://www.hamamatsu.com

[2] The capability to determine the number of photons in a given light pulse.

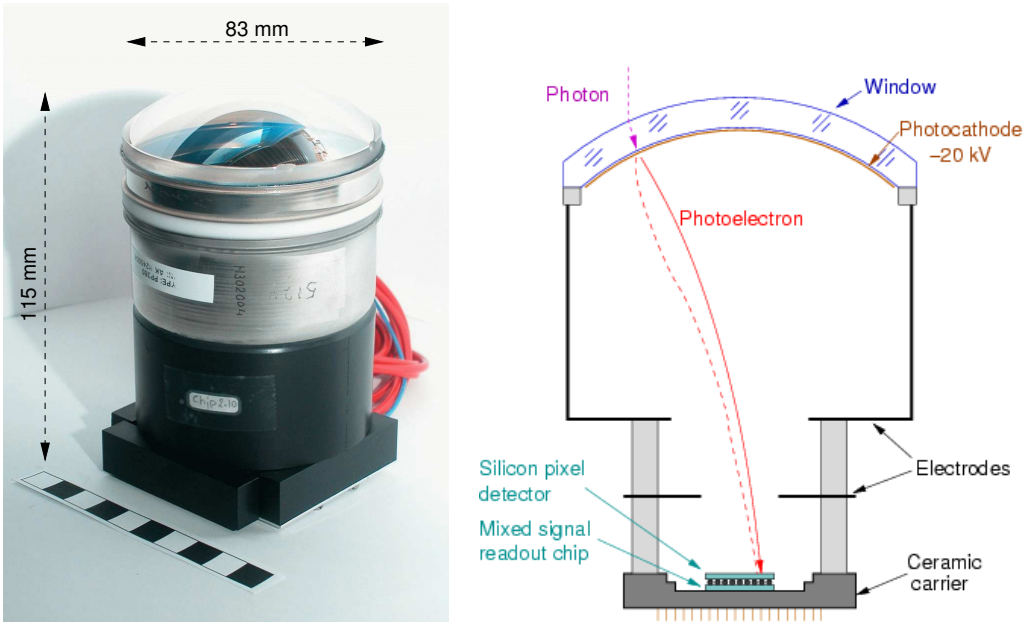

Figure 2.1: The LHCb Pixel HPD. 2.1(a) Photograph of the device. 2.1(b) Schematic view. The continuous line is a sketch of the average electron trajectory. The dashed line represents qualitatively the trajectory of an electron with a non zero emission angle with respect to the normal to the photocathode.

given the one to one correspondence between the electron emission point and the position of the hit on the anode. Other important drawbacks of PMTs are overcome by the HPDs like the low photoelectron collection efficiency and small active area relative to the device area. The active area of the LHCb Pixel HPD reaches 83% of the total front section. HPDs are fast detectors, with a typical pulse duration of few ns.

2.2 Hybrid Photon Detectors

2.2.1 Photocathodes

The first stage of the photon detection is achieved at the photocathode, where the photon is adsorbed and an electron, the *photoelectron*, emitted by the material by photoelectric effect (cf. Fig. 2.1(b)). There are two types of photocathodes. Opaque cathodes are deposited on a metal electrode inside the tube. Electrons are emitted from the illuminated surface. Semi-transparent cathodes are deposited on the inner side of an entrance window and photoelectrons are emitted from the opposite surface with respect to the incoming photons. Only a fraction of the photons is absorbed. Typical photomultipliers, Image Intensifiers and HPDs have semi-transparent photocathodes. The following discussion will focus on the most widely used semi-transparent photocathodes.

The photoemissive material is usually a semiconductor and it is vacuum evaporated and deposited as a thin layer on the window. The photoemission process can be described as a three stage process:

- a photon is absorbed and excites an electron in the material
- the excited electron diffuses in the material losing part of its energy
- the electron reaching the surface of the photoemissive layer has a sufficient residual energy to escape from the material.

Each of the three steps is a random process. Consequently not all the photons reaching the photocathode cause the emission of a photoelectron. The ratio of the number of electrons emitted to the number of incident photons of a given energy is the *quantum efficiency*, QE, of the cathode. Typical values of quantum efficiencies rarely exceed 25%, even if some materials may reach 50% and more. The conversion efficiency can also be measured by the *radiant sensitivity* (responsivity)

$$\mathrm{S\ [A/W]} = \frac{i_k[\mathrm{A}]}{P[\mathrm{W}]}, \tag{2.1}$$

the ratio between the photocurrent i_k and the power P of the incident monochromatic electromagnetic radiation. The two quantities are related by equation:

$$\mathrm{QE} = \frac{h\nu}{e}\mathrm{S} = \frac{hc}{e\lambda}\mathrm{S}. \tag{2.2}$$

The absorption process can be described by equation

$$\frac{d\Phi(\nu, z)}{dz} = -\alpha(\nu)\Phi(\nu, z) \tag{2.3}$$

where $\Phi(\nu, z)$ is the flux of photons of frequency ν at depth z in a semi-infinite layer of the material, or the intensity of the electromagnetic radiation. The absorption coefficient $\alpha(\nu)$ strongly depends on the photon frequency as well as being characteristic of the material. It is related to the optical extinction coefficient $k = \mathrm{Im}\left[\sqrt{\epsilon_r}\right]$ by:

$$\alpha = 4\pi\frac{k}{\lambda}. \tag{2.4}$$

In direct band gap semiconductors the optical absorption coefficient is given by [5]:

$$\alpha \propto \sqrt{h\nu - \mathrm{E}_g} \tag{2.5}$$

where E_g is the energy band gap of the material.

The absorption of the photon results in an excited electron in the conduction band. It then diffuses while losing energy. Limiting the discussion to semiconducting photocathodes, the excited electron can interact with the material only by phonon scattering. The energy loss of each phonon interaction of the order of 0.05 eV, and this allows the electron to diffuse relatively long distances. If the thickness of the photocathode is small enough they can reach the surface of the photoemissive layer. An average *escape depth* of the excited electrons can be defined. For a typical photon energy of few eV and a mean free path between two consecutive phonon interactions in the range 2.5-5.0 nm, the escape depth can be up to some tens of nanometers in semiconducting photocathodes.

The electrons reaching the surface can escape into the vacuum if they have enough residual energy to overcome the surface potential barrier. The height of the barrier depends on the material and on the characteristics of the surface. Therefore also the photocathode deposition conditions may influence it. The electron affinity $\mathrm{E_A}$=$\mathrm{E_0}$-$\mathrm{E_c}$ is the difference between the vacuum level and the base of the conduction band. At room temperature only valence band electrons can give a significant photocurrent. The incident photon must carry an energy sufficient for a valence band electron to overcome the band gap and the electron affinity barrier. Therefore the photon energy must be larger than

a typical photoemission threshold given by:

$$W_{\mathrm{ph}} = \mathrm{E}_0 - \mathrm{E}_\mathrm{v} = \mathrm{E}_\mathrm{g} + \mathrm{E}_\mathrm{A}. \tag{2.6}$$

where E_0 is the energy level of the free electron in vacuum and E_v is the top of the valence band.

It follows from the earlier discussion that the photoelectrons escape the photocathode with randomly distributed initial energy and angle with respect to the normal to the layer. The distributions of energy and angle change with the material and with the photon energy. Multiple inelastic collisions during diffusion and scattering at the surface barrier generate more or less complicated distributions. The emission angle is not correlated with the direction of the incoming photon. The kinetic energies are distributed in the range from 0 eV to a maximum determined by the energy of the absorbed photon hν:

$$\mathrm{E}_{\mathrm{k,max}} = h\nu - W_{\mathrm{ph}}. \tag{2.7}$$

Commonly used semiconducting photocathodes are silver-oxygen-caesium (AgOCs), antimony-caesium (SbCs), bi-alkali (SbKCs, SbRbCs) or multi-alkali ($\mathrm{SbNa_2KCs}$) compounds. Gallium arsenide GaAs(Cs) and GaAsP(Cs) have become more recently of wide spread use owing to their higher quantum efficiencies. Caesium is evaporated in the last step of the process on the previously deposited p-doped semiconducting layer. This causes the bending of the energy levels at the surface due to the formation of a p-n junction. Therefore the difference between the vacuum energy level and the in-depth value of E_c, that is the efficient electron affinity, is reduced. This is essential to make photocathodes sensitive in the visible range of the spectrum.

Multi-alkali photocathodes are polycrystalline semiconducting layers with E_g=1.3-1.4 eV. They have nearly zero electron affinity (NZEA). A phonon energy value of $\mathrm{E}_{ph} = 0.027 \pm 0.002$ eV was reported [5]. A typical curve of the multi-alkali spectral response is given in Fig. 2.2, together with some other photoemissive materials. The radiant sensitivity peaks at λ=420 nm, reaching 70 mA/W. The quantum efficiency has a maximum around 250 nm, reaching 25%.

2.2.2 The electron optical system and the point spread function

The photoelectron that escapes the photocathode into the vacuum region of the tube is accelerated and focused onto the HPD sensor by a static electric field. Accelerating voltages of 15-25 kV are employed in HPD tubes. The field configuration is determined by a set of electrodes kept at well designed voltages

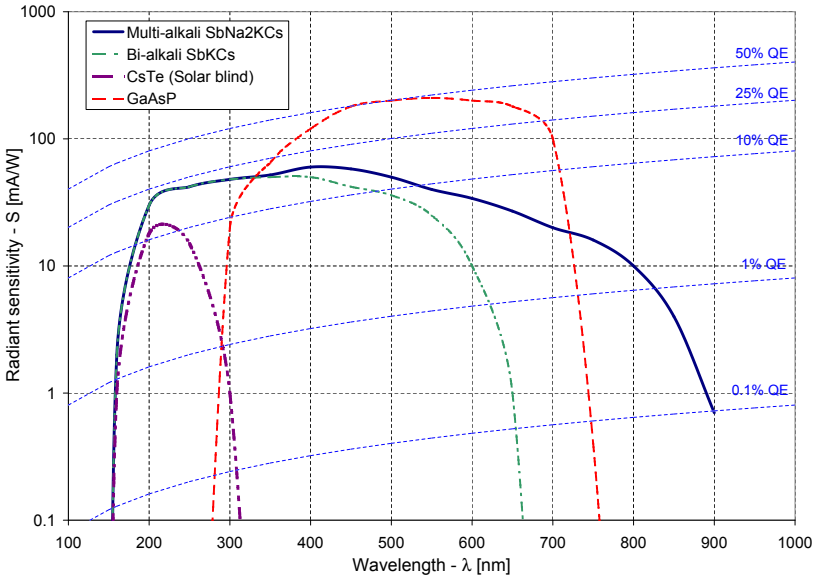

Figure 2.2: Radiant sensitivities of some photoemissive semiconductors as functions of incident radiation wavelength. Curves of constant quantum efficiency are shown.

Three different types of HPDs can be distinguished on the basis of the geometries of the accelerating field and the corresponding shape of the electron trajectories. Proximity focused HPDs operate with a uniform field parallel to the tube axis z[3]. Assuming zero initial velocity, the photoelectron trajectories coincide with the field lines parallel to z. The electronic image on the anode has the same size of the cathode. Such devices need only one bias voltage and are compact.

Careful design of a set of electrodes kept at various voltages realizes an electronic lens, allowing to focus the photoelectrons on an anode smaller than the cathode. The trajectories may or may not intersect, resulting in the *cross focusing* or in the *fountain shaped* geometry respectively. In all cases a one to one correspondence between the emission points and the hit points can be preserved. The photon hit position can be determined if a pixel silicon sensor is employed as detecting anode, obtaining a position sensitive (*imaging*) device like the LHCb Pixel HPD.

From the earlier (Section 2.2.1) discussion on the distribution of the photoelectron initial energy, it follows that the photoelectron trajectories originating from a given point on the photocathode surface are actually mapped onto an extended region surrounding the average hit position on the anode. This is

[3]Cylindrical symmetry of the devices is assumed.

also sketched in Fig. 2.1(b). The ideal point to point correspondence between cathode and anode is affected and an intrinsic limit is set to the spatial resolution of HPDs and similar devices. The *point spread function* is the distribution of the hit points on the anode corresponding to a fixed emission point. It will be quantified by its RMS spread on two perpendicular directions on the anode surface.

The mapping function between cathode and anode and the point spread function are determined by the choice of the electrode geometry and voltages. A design minimizing the latter may not be satisfactory on the aspect of the geometrical correspondence, so a compromise choice is often required. The design is invariably computer aided and implies a trial and error optimization of the calculated field map and photoelectron trajectories until the mapping functions and the point spread function satisfy the requirements.

2.2.3 The Hybrid Photon Detector anode. Silicon detectors

The detection of the photoelectron is done with a silicon sensor acting as the HPD anode. The silicon sensor is a reverse biased, fully depleted p-i-n silicon detector. The kinetic energy of the incoming photoelectron is released in the silicon, resulting in the generation of electron hole pairs. Charge carriers drift in the sensor inducing current signals in the readout circuitry connected to the pixel pads. The principle is illustrated in Fig. 2.3.

A description of the signal formation and detection mechanisms are given in the following. Signal generation in the silicon detector is first described, followed by a discussion on the signal amplification. The flip-chip bump bonding technology is then presented. It allows the combination of the sensor and of the readout electronic in a hybrid pixel detector. A hybrid pixel detector is used for the LHCb Pixel HPD anode.

Charge generation

Electrons penetrating the silicon sensor with energies in the keV range are scattered in the material by inelastic collisions with electrons and by elastic collisions with the shielded nuclei. The inelastic collisions may involve:

- ionization of atoms at deep energy levels. A chain of ionization events develops with an increasing number of free electrons sharing the initial energy. Part of the initial energy is also spent in the creation of phonons.
- Generation of X-rays. The rearrangement of the electron shells causes emission of an X-ray photon that can in turn excite other electrons.

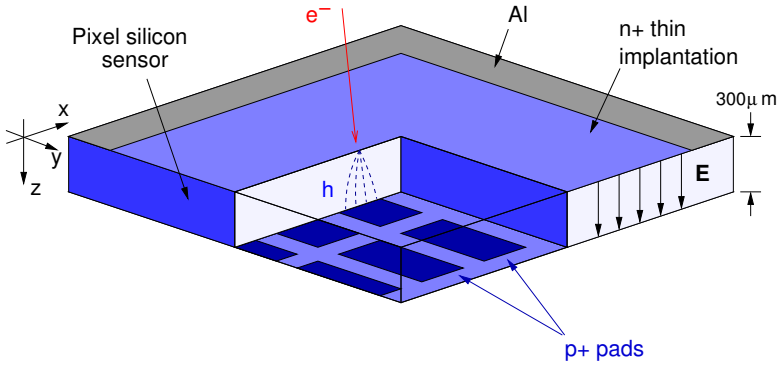

Figure 2.3: A schematic illustration of a pixel silicon detector.

- Absorption in the valence band.
- Excitation of volume and surface plasmons.

The first two processes result in the excitation of electrons in the conduction band, while the elastic collisions scatter the electrons by large angles.

In [6] a model is given for the dependence of the electron energy loss as a function of penetration depth. It is shown that it does not depend on the material once the depth and the energy are normalized to the penetration range and to the initial energy. The experimental results on penetration depth R are well described by:

$$R = 3.98 \cdot 10^{-6}\ E_{el}^{1.75}\ \left[\frac{g}{cm^2}\right] \tag{2.8}$$

for an incoming electron energy E_{el} in the 5-50 keV range. The energy is expressed in keV and the depth is normalized with the density of the material in previous equation. It follows that for 20 keV electrons in Si (ρ=2.33 g/cm^3) is R $\simeq$ 3.2 μm. The photoelectron is completely stopped and its energy released in a thin layer below the entrance surface, resulting in the formation of electron-hole pairs as discussed before. This process is sometimes called charge injection by electron bombardment.

The scattering at wide angles of the energetic photoelectron entering the silicon detector may cause the back-diffusion (*back scattering*) of the incident photoelectron in a significant fraction of events (10-25%). In this cases the initial energy is only partially released in the material. Moreover, the electrons excited in the material can acquire an energy sufficient to escape from the surface (as in secondary emission). Both processes cause a reduction of the number of carriers released in the detector by a photoelectron hit.

An average energy ϵ for the creation of an electron-hole pair can be defined:

$$\epsilon = \frac{\mathrm{E}}{< \mathrm{N} >} \tag{2.9}$$

with E the energy released and N the number of pairs. Independently of materials and radiation type [7, 8] it is roughly $\epsilon = 2.8\mathrm{E_g} + r$ [eV], where $0.5 < r < 1.0$ eV. The average pair creation energy is larger than the band-gap $\mathrm{E_g}$ because of two main reasons. Momentum conservation may require the simultaneous emission of a phonon. Other processes are possible requiring less energy than $\mathrm{E_g}$. The value for silicon is:

$$\epsilon(\mathrm{Si}) = 3.63 \text{ [eV]}. \tag{2.10}$$

A 20 keV photoelectron stopped in silicon releases on average 5510 e-h pairs. For comparison, a minimum ionizing particle[4] releases 112 keV across 300 μm of Si, corresponding to ∼30000 e-h pairs created along the track crossing the entire thickness of the detector.

The electrons excited by the primary one lose their energy by inelastic phonon scattering or pair creation. This cascade process results in a statistical fluctuation of the number of generated carriers. The variance of the fluctuation is proportional to the average number of pairs by the Fano factor F [10]:

$$\sigma_{\mathrm{N}}^2 =< \Delta \mathrm{N}^2 >= \mathrm{F} \cdot < \mathrm{N} > = \mathrm{F} \cdot \frac{\mathrm{E}}{\epsilon}. \tag{2.11}$$

Typical values of F are in the range 0.08-0.13 and F=0.115 in silicon. See [11] and references therein for a model of scattering in semiconductors and a derivation of Eq. (2.11).

The fluctuation of the generated charge constitutes an intrinsic source of noise. The relative spread with respect to the average number of carriers is readily found to be:

$$(\mathrm{HPD}) \rightarrow \quad \frac{\sigma_{\mathrm{N}}}{< \mathrm{N} >} = \sqrt{\frac{\mathrm{F}}{< \mathrm{N} >}} = \frac{0.33}{\sqrt{< \mathrm{N} >}}. \tag{2.12}$$

A similar fluctuation of the number of carriers occurs for secondary emission at the first dynode of the chain of a photomultiplier tube. In the case of secondary emission from a dynode, however, the number of emitted electrons follows a Poisson distribution[5]. Then the relative variance of the number of

[4] A heavy charged particle with ($\beta\gamma \simeq 3$) giving the minimum specific energy loss of $d\mathrm{E}/dx = 1.6$ [(MeV cm^2)/g], Ref. [9].

[5] No solid theoretical background has been found for this [12], but it is a customary approximation of the measurements.

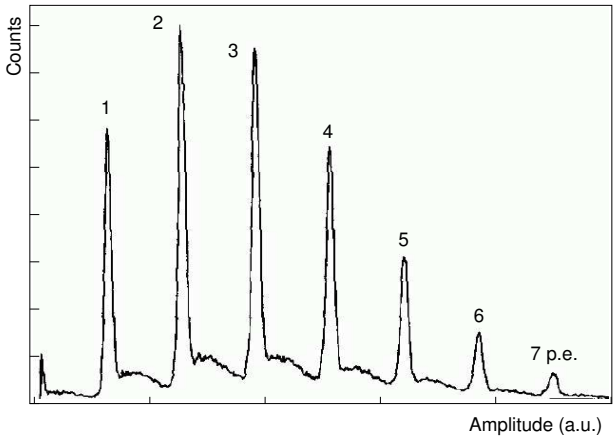

Figure 2.4: A pulse amplitude spectrum measured on a HPD under very low illumination, giving on average $< \mathrm{N} > \sim 2.8$ photoelectrons (from Ref. [14]).

carriers N in a photomultiplier is given[6] by:

$$(\mathrm{PMT}) \rightarrow \qquad \frac{\sigma_{\mathrm{N}}}{< \mathrm{N} >} = \frac{1}{\sqrt{< \mathrm{N} >}}. \tag{2.13}$$

In the case of the HPD (Eq. 2.12) one has $< \mathrm{N} > \simeq 5000$. The typical value of the secondary emission coefficient in dynodes, to be introduced in Eq. (2.13), is in the range 5-15[7]. The reduction of relative spread due to the Fano factor adds up to the smaller relative spread intrinsic to the single step gain mechanism of the HPD. Consequently a typical pulse amplitude spectrum of a HPD has well separated and sharp peaks corresponding to the events with different number of electrons hitting the sensor. An example is given in Fig. 2.4, showing the excellent photon counting capability of the HPD [13]. The background of the amplitude spectrum is due to the partial release of energy in a fraction of events because of back scattering.

Signal induction and motion of charge carriers

The charge q generated in the fully depleted sensor drifts in the electric field in the intrinsic (depleted) region. During the drift of q a charge $\mathrm{Q}(t)$ is induced on the pixel pad (electrode) and a current $i(t) = d\mathrm{Q}/dt$ flows in the readout circuit connected to the pad. The current pulse is induced during the drift process and constitutes the output signal. It begins with the injection of the carriers and terminates when all drifting charges are neutralized at the

[6] If N is a Poisson distributed stochastic variable of mean μ, from $\mathrm{P}_{\mu}(\mathrm{N}) = e^{-\mu}\frac{\mu^N}{N!}$ follows: $< (\mathrm{N} - \mu)^2 >= \mu$.

[7] Modern negative electron affinity GaP(Cs) dynodes may reach values of 60-100.

electrodes. The time integral of the current flowing in the external circuitry is equal to the charge q.

The current pulse is resulting from the motion of electrons and holes and the two contributions can be independently determined [10]. In our case the charge is injected in a layer close to the n+ implantation. The electrons drift toward the implantation layer rapidly reaching the insensitive undepleted region. The component of the current due to the electrons is a fast pulse with a duration much shorter than the one due to the holes. These drift across the entire thickness of the depleted detector, recombining when reaching the p+ pads (Fig. 2.5(a)).

The charge and currents induced on a set of electrodes at the boundaries of a region in which a point charge is drifting, can be determined by the Shockley-Ramo theorem. An interesting review and a straightforward demonstration based on conservation of energy are given in [15]. The theorem states that the charge Q and the current i induced by a moving charge q on the j-th electrode of a given set are determined by:

$$\mathrm{Q} = -q\phi_0(\mathbf{x}) \tag{2.14}$$

$$i = q\mathbf{v}\cdot\mathbf{E}_0(\mathbf{x}). \tag{2.15}$$

$\mathbf{v}$ is the instantaneous velocity of charge q located at $\mathbf{x}$.

$\phi_0(\mathbf{x})$ and $\mathbf{E}_0(\mathbf{x}) = -\nabla\phi_0(\mathbf{x})$ are the electric potential and field that would exist at point $\mathbf{x}$ under the following conditions: electrode j at unit potential, all other electrodes at zero potential and all space charges removed. They are called *weighting potential* and *weighting field*. A corollary of the theorem is that the charge (current) induced does not depend on the potentials applied to the electrodes but only on the geometry of the problem and on the position (motion) of the charge.

In order to get at least a qualitative understanding of the importance of the theorem to determine the induced current pulse, let us consider an ideal situation condition like the one shown in Fig. 2.5(a). It represents a two dimensional section of a structure similar to two conducting parallel plates, separated by a distance d. The lower plate is segmented in smaller adjacent electrodes of size D, separated by gaps. The electrodes at the bottom are kept at potential $-V$ with respect to the plate situated above. The field in the region between the plates is uniform in the ideal approximation of an infinitesimal gap between the electrodes.

The weighting potential relative to electrode j is the solution of Laplace equation with the boundary conditions: electrode j at unit potential and all others at zero. A solution may be found, for example, by considering the

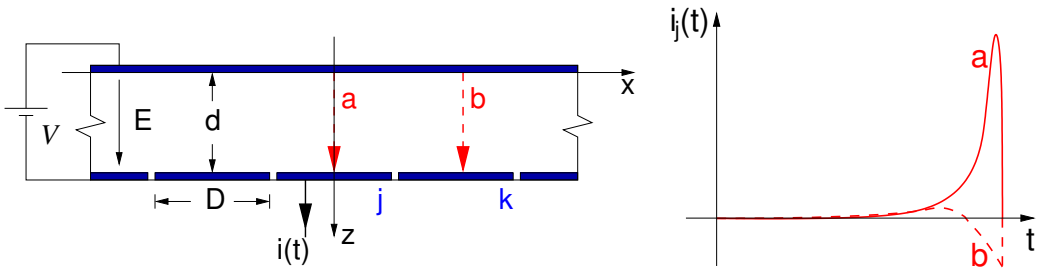

(a) (b)

Figure 2.5: 2.5(a) Scheme for the evaluation of the currents induced on electrode j by a point charge drifting along paths a or b. 2.5(b) Current pulses corresponding to drift along a or b (qualitative).

potential partial Fourier transform with respect to x, obtaining:

$$\phi_0(x,z) = \frac{1}{2\pi}\int \frac{D\sin\left(\frac{kD}{2}\right)}{\left(\frac{kD}{2}\right)}\frac{\sinh(zk)}{\sinh(dk)}e^{\jmath kx}dk. \tag{2.16}$$

The previous function is plotted in Fig. 2.6. Cuts along the depth in the detector z, at different displacements with respect to the center of electrode j, are plotted in Fig. 2.7.

Let us consider a point charge q drifting with uniform speed[8] along the paths labeled a and b in Fig. 2.5(a).

The curve labeled +0 in Fig. 2.7 gives the weighting potential with respect to z along path a. The z-component of the gradient of the weighting potential increases going closer to electrode j. Therefore the induced current (cf. Fig. 2.5(b)) shows a rise toward the end of its duration, according to Eq. (2.15). The drifting charge is neutralized at its arrival at the electrode and the integral of the current pulse is equal to q. Consider now the drift along path b. The weighting potential along b is labeled with +62 in Fig. 2.7 and its gradient changes sign approaching electrode k. This corresponds to the bending of the weighting field lines originating from j and terminating onto k. Consequently the current induced on j has the evolution labeled with b in Fig. 2.5(b). The integral of the current is zero, still corresponding to the total charge collected at electrode j in this ideal case.

[8]This is a simplification. The motion would be uniformly accelerated in vacuum. It would be with constant speed only in a semiconductor and in absence of space charge. In the case of non zero space charge the velocity increases with the electric field rising along z. This actually enhances the peaking shape of the current pulse.

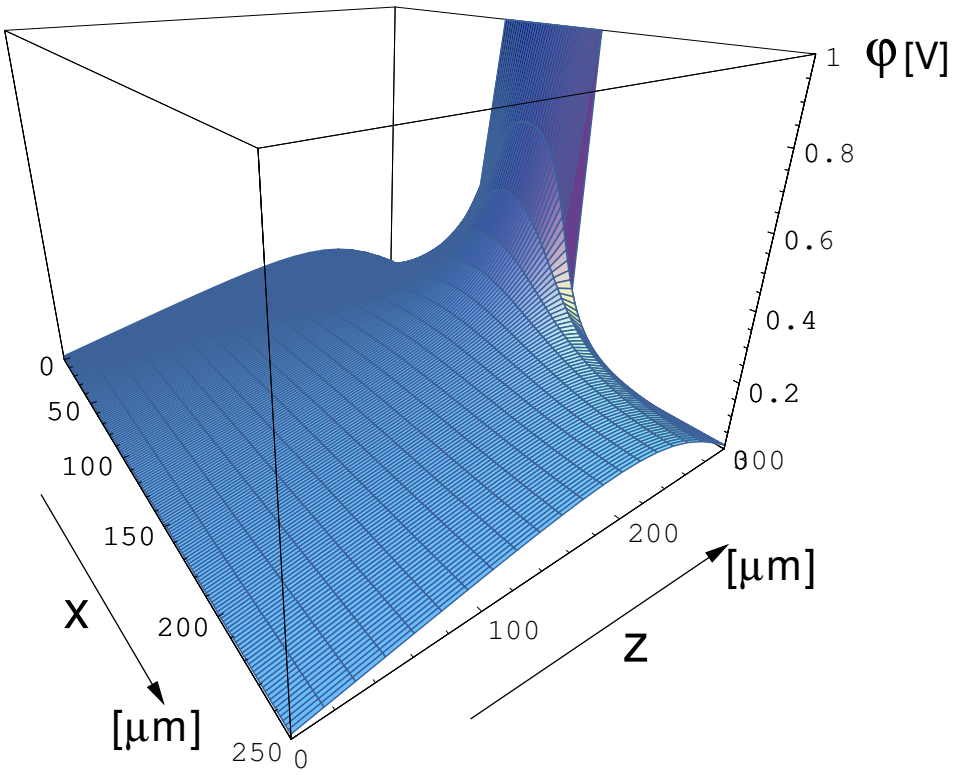

Figure 2.6: Weighting potential in the two dimensional geometry of Fig. 2.5(a). Eq. (2.16) is plotted for d=300 μm and D=62.5 μm. The center of electrode j is at x=125 μm.

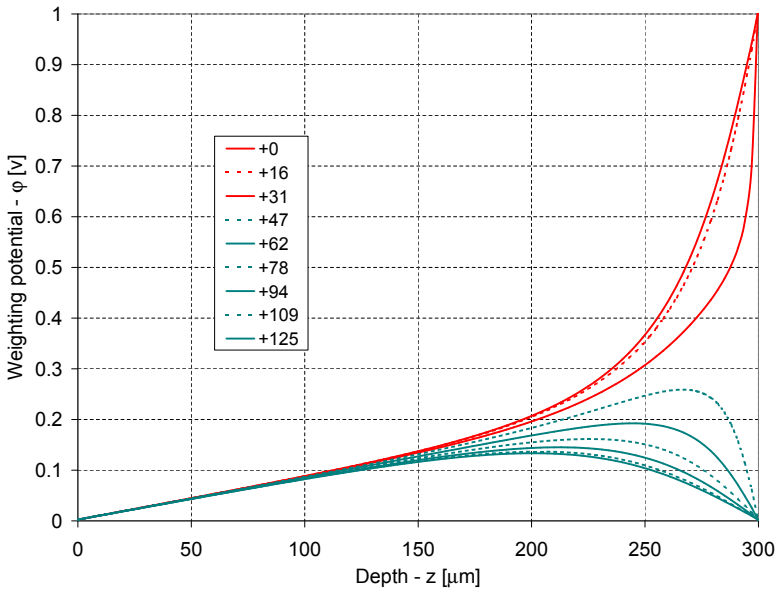

Figure 2.7: Cuts along z of the weighting potential of Fig. 2.6 at different distances (indicated in μm in the legend) from the center of the considered electrode (x=125 μm in Fig. 2.6).

In the real case a set of holes is released by the photoelectron hitting the detector. Lateral diffusion of the cloud of charge drifting in the detector causes sharing of charge between pixels, as shown in Fig. 2.8. The integral of the current pulse of the adjacent pixel is equal to the collected fraction of the charge. An estimate of this effect is given in Section 2.3.5 for the case of interest.

The module of the electric field in the bulk of the reverse biased silicon detector, as a function of depth z, can be written:

$$E(z) = E_0 + \frac{e\mathrm{N_{eff}}}{\epsilon} z \tag{2.17}$$

where e is the electron charge, $\mathrm{N_{eff}}$ is the volume density of donors in the n-bulk and ϵ is the dielectric permittivity of the material. E_0 is a constant term depending on the applied reverse bias voltage V_b and detector thickness d[9]:

$$E_0 = \frac{1}{d}\left[V_b - \frac{1}{2}\frac{e\mathrm{N_{eff}}}{\epsilon} d^2\right]. \tag{2.18}$$

[9]The right term between parenthesis in Eq. 2.18 is the depletion voltage. It is proportional to $\mathrm{N_{eff}}$. To achieve full depletion at reasonable voltages, it is compulsory to use high resistivity silicon with a low level of impurities. Sufficient purity can be obtained only growing the crystal with the Fused Zone method.

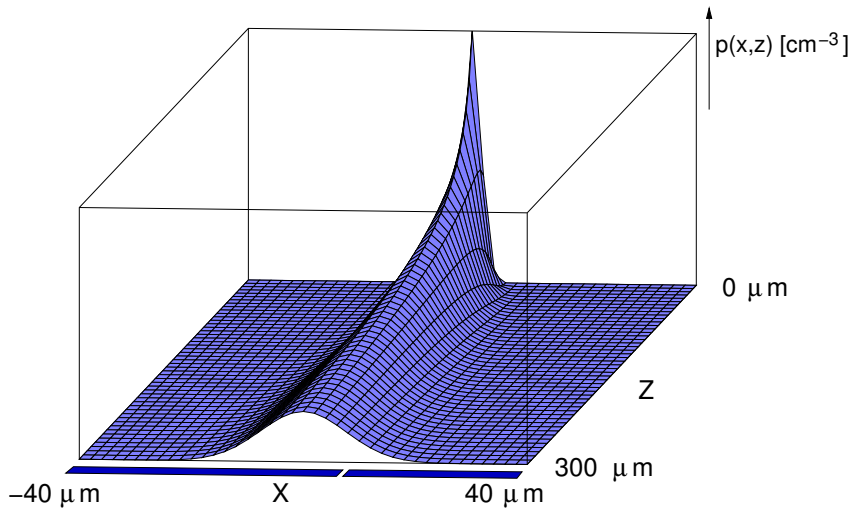

Figure 2.8: Concentration profile p(x,z) of the injected holes at different depths z in the silicon sensor while drifting toward the pixel pads and laterally diffusing. Drift is from z=0 μm to z=300 μm. The dark polygons next to the x axis are a qualitative sketch of two adjacent p+ pads.

Solving the equation of motion of a point charge with mobility μ in the field given by Eq. (2.17), one obtains the transit time necessary to cross the full detector:

$$t_{tr} = \frac{\epsilon}{\mu e \mathrm{N_{eff}}} \ln\left[1 + \frac{e\mathrm{N_{eff}} d}{\epsilon E_0}\right]. \tag{2.19}$$

$z = 0$ was assumed as the initial position of the charge.

While drifting under the action of the field, the cloud of carriers diffuses laterally. The transverse charge density distribution is Gaussian with a RMS spread σ_x increasing with time t:

$$\sigma_x = \sqrt{2Dt} \tag{2.20}$$

$$D = \frac{kT}{e}\mu. \tag{2.21}$$

Eqn. (2.21) is Einstein's equation relating the diffusion coefficient D to mobility μ.

It is of interest to plot the transit time of holes as a function of the reverse bias voltage. The result is shown in Fig. 2.9 together with the transverse lateral spread due to diffusion during a time interval of the same duration. The parameters valid for the LHCb Pixel HPD silicon sensor were used in the computation. They are listed in Table 2.3 on page 47. These considerations and the earlier discussion on Ramo-Shockley theorem show that the reverse bias voltage has a strong influence on the current pulse shape, duration and amplitude.

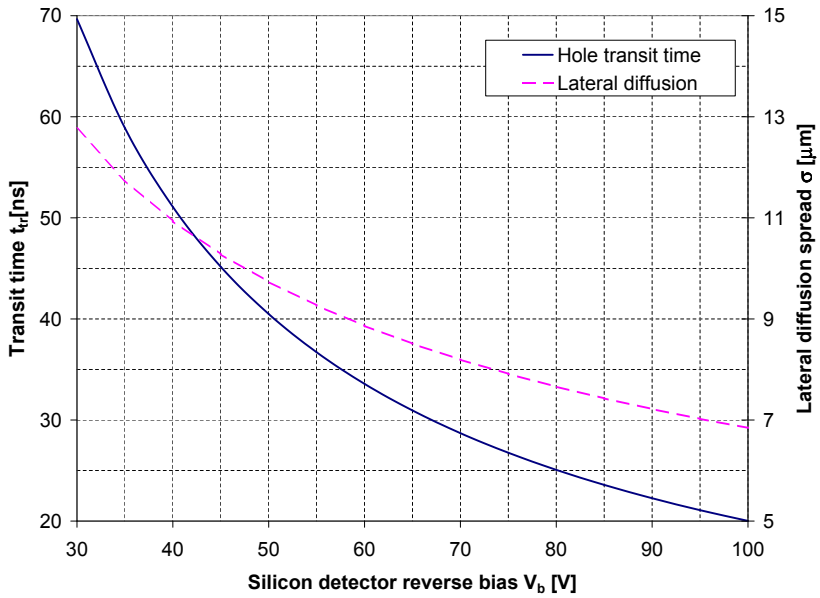

Figure 2.9: Transit time and lateral diffusion of holes in a silicon sensor, as a function of the reverse bias voltage. The curves were calculated from Eq. (2.19) and (2.20), assuming the LHCb Pixel HPD silicon sensor parameters (Table 2.3).

Readout electronics: charge amplification, pulse shaping and noise model

The current pulse from the detector must be amplified and processed in order to be detected. A canonical analog front end commonly used for particle detectors is shown in Fig. 2.10. The silicon detector is modeled by a reverse biased diode, I_b is the reverse current and C_d the capacitance.

Considering the response time of the amplifying circuit, the current pulse signal $i_s(t)$ can be considered of infinitesimal duration and total integral equal to the injected charge Q_s, i.e. $i_s(t) = Q_s\delta(t)$. The signal pulse is applied to the input of a charge sensing amplifier (CSA), via the decoupling capacitance C_s. The CSA integrates the pulse current on the feedback capacitance C_f. This allows the response to be independent from C_d:

$$V_2 = \frac{Q}{C_f + \frac{C_f + C_d}{A_0}} \simeq \frac{Q}{C_f}, \tag{2.22}$$

where A_0 is the CSA low frequency gain.

The CSA is followed by a shaper section, indicated in the figure by its transfer function $W_\tau(s)$. It can be assumed that the CSA has a much higher bandwidth than the following shaper and then it can be simply modeled by a

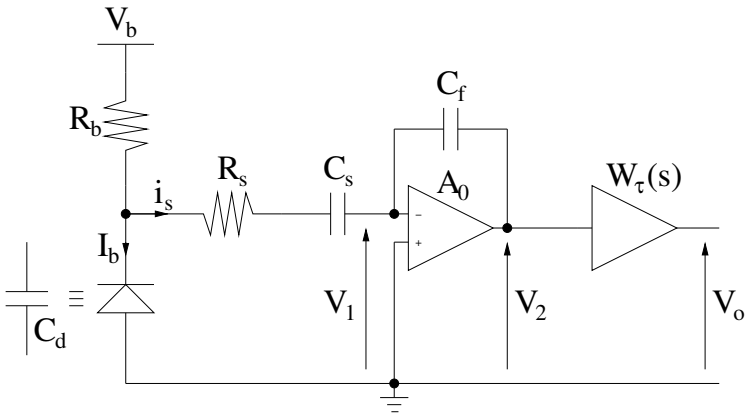

Figure 2.10: Circuit schematic of a front end amplifier for a silicon detector.

constant gain A_0. The shaper integrates the output of the CSA, allowing the formation of a pulse with a peak value proportional to the input charge. A differentiating behavior is also needed to restore the output baseline to ground, in order to process the following pulses avoiding the buildup of pulses at the output.

The simplest shaping function can be realized by cascading a single pole RC integrator (low pass filter) and a single pole CR differentiator (CR high pass filter). The output pulse peak amplitude is maximized choosing the same time constant τ for the two stages. For the present discussion, it is then assumed:

$$W_\tau(s) = \frac{s\tau}{(1+s\tau)^2}. \tag{2.23}$$

The unit step response of this system is

$$w(t) = \frac{t}{\tau} e^{-\frac{t}{\tau}} u(t), \tag{2.24}$$

reaching its peak value e^{-1} at instant $t = \tau$. From Eq.(2.22) it follows that the output pulse amplitude is:

$$v_{ox} = v_o(\tau) = \frac{Q}{eC_f}. \tag{2.25}$$

Noise rejection is provided by the band-pass response function. The equivalent circuit for the noise analysis is shown in Fig. 2.11. There are two thermal noise equivalent sources ${i_b}^2$ and ${e_s}^2$, related to the bias resistor R_b and the series resistor R_s respectively. The shot noise of the reverse current in the silicon detector is modeled via source ${i_d}^2$. The noise of the preamplifier section is modeled via two series generator ${e_n}^2$ and ${e_f}^2$, the latter representing the flicker

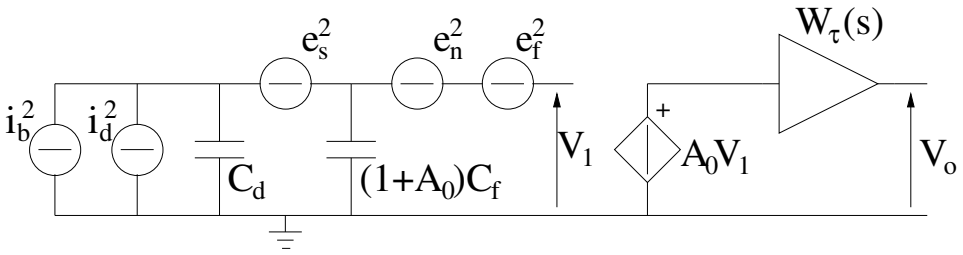

Figure 2.11: Noise model equivalent of the circuit shown in Fig. 2.10. Refer to the text for a detailed description.

noise. The parallel resistance R_b and the series impedance $R_s + 1/(sC_s)$ were not included because with a proper design they must be negligible with respect to the preamplifier input impedance.

The power spectral densities of the stochastic signal sources are:

$$i_d{}^2 \rightarrow \quad q_e I_b \tag{2.26}$$
$$i_b{}^2 \rightarrow \quad \frac{2kT}{R_b} \tag{2.27}$$
$$e_s{}^2 \rightarrow \quad 2kTR_s \tag{2.28}$$
$$e_n{}^2 \rightarrow \quad P_{en} \tag{2.29}$$
$$e_f{}^2 \rightarrow \quad \frac{A_f}{|f|}. \tag{2.30}$$

They are independent sources of white noise, apart from the flicker noise with the characteristic 1/f power spectral density.

Let us consider the $i_d{}^2$ and the $e_n{}^2$ sources. The covariance of the output v_{od} due to source $i_d{}^2$ is obtained integrating over frequency the square of the trans-impedance characteristic times the input power spectral density, namely:

$$< v_{od}^2 > \simeq \frac{q_e I_b}{C_f^2} \int_{-\infty}^{+\infty} \frac{\tau^2}{(1+(2\pi f\tau)^2)^2} df = \frac{q_e I_b \tau}{4C_f^2}. \tag{2.31}$$

In a similar way the covariance of the output v_{on} due to source $e_n{}^2$ is obtained by:

$$< v_{on}^2 > \simeq A_0^2 P_{en} \int_{-\infty}^{+\infty} \frac{(2\pi f\tau)^2}{(1+(2\pi f\tau)^2)^2} df = P_{en} \frac{A_0^2}{4\tau}. \tag{2.32}$$

It is customary to express the output noise covariance by the equivalent noise charge (ENC), defined as the input charge that gives an output pulse amplitude equal to the RMS noise. Considering Eq. (2.25), the ENC contri-

butions of the shot and electronic noise are:

$$\mathrm{Q}_{\mathrm{od}}^2 = e^2\mathrm{C}_{\mathrm{f}}^2 < \mathrm{v}_{od}^2 >= \frac{e^2}{8} 2q_e \mathrm{I}_{\mathrm{b}} \tau \tag{2.33}$$

$$\mathrm{Q}_{\mathrm{on}}^2 = e^2\mathrm{C}_{\mathrm{f}}^2 < \mathrm{v}_{on}^2 > \simeq \frac{e^2}{8} 2\mathrm{P}_{\mathrm{en}} \frac{\mathrm{C}_{\mathrm{eq}}^2}{\tau}. \tag{2.34}$$

Following a similar procedure for all the other sources of noise, the overall ENC is determined:

$$\mathrm{Q}_{\mathrm{ENC}}^2 = \left(\frac{e^2}{8}\right)\left[\left(2q_e\mathrm{I}_{\mathrm{b}} + \frac{4k\mathrm{T}}{\mathrm{R}_{\mathrm{b}}}\right)\tau + \left(4k\mathrm{TR}_{\mathrm{s}}\mathrm{C}_{\mathrm{d}}^2 + 2\mathrm{P}_{\mathrm{n}}\mathrm{C}_{\mathrm{eq}}^2\right)\frac{1}{\tau} + 8\mathrm{A}_{\mathrm{f}}\mathrm{C}_{\mathrm{eq}}^2\right] \tag{2.35}$$

where $\mathrm{C}_{\mathrm{eq}} = \mathrm{C}_{\mathrm{d}} + (1 + \mathrm{A}_0)\mathrm{C}_{\mathrm{f}}$ is the equivalent capacitance at the input.

While the parallel noise sources contribute proportionally to the integration time, the effect of the noise sources in series with the input is inversely proportional to τ. Moreover the latter increases with the overall capacitance at the preamplifier input. In a realistic situation this would include all stray and wiring capacitances.

A plot of previous equation with realistic values for the numerical coefficients is given in Fig. 2.12. From the earlier analysis and referring to the figure, it follows that:

- the minimum of th ENC is obtained for an optimal value of integration time. The parallel and the series noise are equal in this case.
- The series and 1/f noise contributions get smaller reducing the equivalent capacitance at the input; the minimum ENC consequently reduces.
- The optimal integration time reduces as the equivalent capacitance is reduced. This means that the system may have a faster response (larger bandwidth.

Summarizing the previous discussion, *the reduction of the equivalent input capacitance* is the necessary condition to obtain a detection system with higher sensitivity and speed.

2.2.4 Hybrid pixel detectors. Flip chip bump bonding

The state of the art in pixel detector technology is the *hybrid pixel* technique [17], used also for the LHCb Pixel HPD anode assembly. The technique is illustrated in Fig. 2.13. A pixel silicon sensor is overlaid on a readout chip. The two chips are mechanically and electrically connected by the flip-chip bump bonding technique. A matrix of small solder bumps connects the two

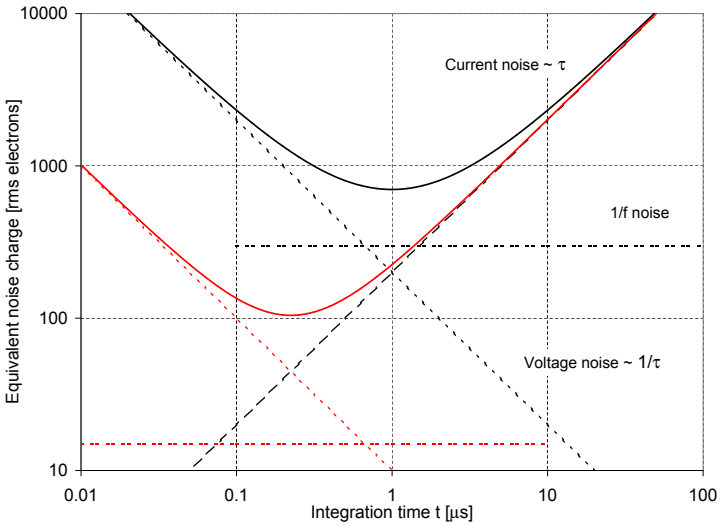

Figure 2.12: Equivalent noise charge vs. integration time calculated from (2.35). The voltage noise and 1/f noise curves are plotted for two different values of capacitance. Optimum integration time and ENC consequently reduce (from Ref. [16]).

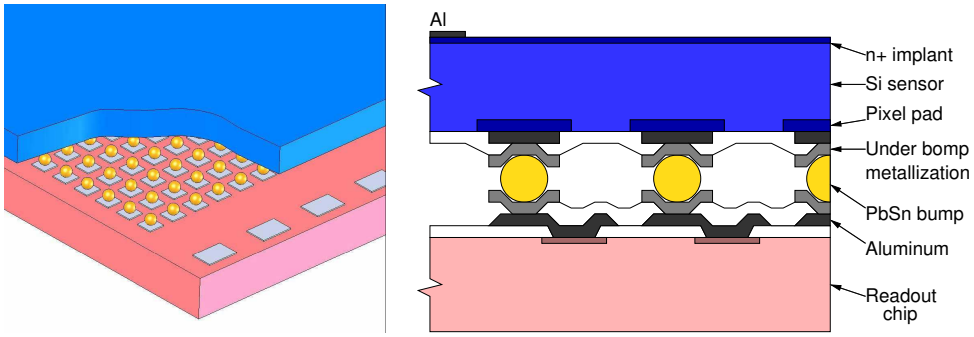

(a) (b)

Figure 2.13: Illustrations (not in scale) of the flip chip bump bonding technique. Each pixel pad of the silicon sensor (on top) is connected to an input pad on the readout chip (bottom) via a metallic bump.

chips, providing an electrical path between each of the sensor pixels and the corresponding readout circuitry.

Hybrid pixel detectors offer many advantages. The sensitivity is favored by the reduction of the stray capacitance (cf. Section 20). Signal charge much below ∼1000 electrons can be efficiently detected with proper low noise electronic design. The entire detector area is sensitive to incoming particles, with uniform sensitivity across the surface and no dead gap between pixels. The device is position sensitive due to its fine pixelization. Spatial resolution can reach 10 μm, being limited by charge diffusion. Moreover, the minimum attainable pitch and dimension of the interconnecting metallic bumps is of the order of ∼25 μm at the present time. A full mixed signal readout chain can be realized on the readout chip, providing the device with digital readout.

The bump bond connections can be made of SnPb solder[10]. The technological steps [18] can be summarized as follows. Windows in the passivation layers are opened at the desired locations of the sensor and the readout wafers by lithographic techniques[11]. Under bump metallizations (Ni) and the solder are then electroplated. The solder is normally grown thicker on the readout wafer. After removal of the processing layers the bumps are re-flowed (Fig 2.14(a)). The sensors and the readout chips are diced from the wafers. The sensor chips are flipped upside down and aligned on top of the readout chips. Pressure and heating allow the formation of the bump bonds (Fig. 2.14(b)).

[10]Indium is also used [17].

[11]The wafers for the sensors have typically 125 mm diameter, being the crystal manufactured with the fused zone (FZ) method.

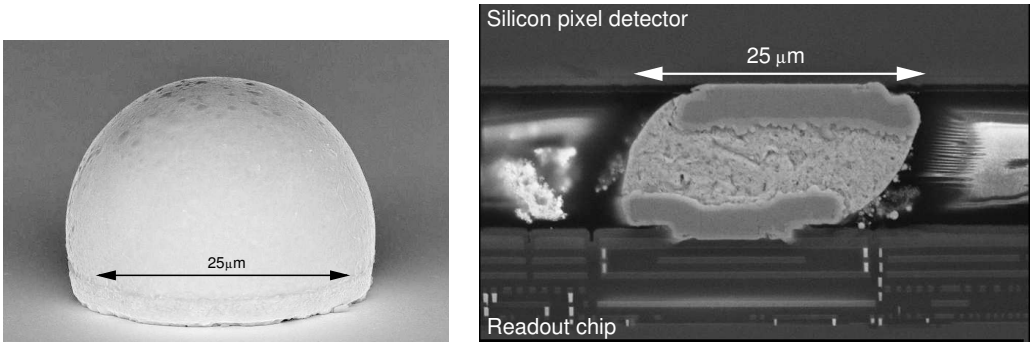

(a) (b)

Figure 2.14: SEM photographs of bump bonds. Fig. 2.14(a) shows a single high Pb content solder bump after reflow, on a glass substrate. Fig. 2.14(b) shows a cut of the LHCb Pixel HPD anode assembly with a bump bond in evidence. Under bump Ni metallizations are visible.

λ [nm]	Typical transmittance T
200	0.35
240	0.75
>280	0.92

Table 2.1: Typical transmittance of the LHCb Pixel HPD synthetic silica entrance window. Values include boundary reflections.

2.3 LHCb Pixel Hybrid Photon Detector

2.3.1 Entrance window

The LHCb Pixel HPD entrance window is made of synthetic silica. It is a circular section of a spherical shell. The external and internal surfaces have 62 mm and 55 mm radii of curvature. The external diameter of the window is about 80 mm. The typical transmittance is summarized in Table 2.1.

2.3.2 The photocathode

The LHCb Pixel HPD is equipped with an S20[12] multi-alkali photocathode. It is vacuum evaporated on the inner surface of the window during the assembly of the device. The photocathode active diameter is 72 mm and is defined by an annular metalization following the evaporation. The refraction at the entrance

[12]The S designation refers to the overall spectral characteristic including the effect of the input window and does not identify the material (JEDEC N. 50, Oct. 1954, S curves).

λ [nm]	E [eV]	Minimum QE
270	4.59	0.20
400	3.10	0.157
520	2.38	0.083

Table 2.2: Specification on the LHCb Pixel HPD quantum efficiency QE, including losses due to the entrance window. Minimum values of quantum efficiency are required at three different photon wavelengths λ. The corresponding photon energies E are listed.

window results in an active diameter of ∼75.5 mm for normally incident light. The maximum external diameter of the device is 83 mm, resulting in an active-to-total area ratio of 83%.

The specification on the quantum efficiency is summarized in Table 2.2. Minimum values of QE are specified at three different wavelengths. The specified values include the effects of reflections at the interfaces and absorption in the window.

Electrons are emitted by the photocathode even with no direct illumination. This is due to thermoionic emission and causes the detection of hits (dark counts) on the anode not corresponding to photons hitting the cathode. The dark count rate is higher for the photocathodes with a higher radiant sensitivity in the long wavelength region (Fig. 2.20 on page 56). The specification for the LHCb Pixel HPD requires the dark count rate to be less than 5 kHz/cm^2 at 25 °C. The value measured for the first prototypes [19] was $\sim$ 1 kHz/cm^2 at 25 °C. This rate corresponds to an average number of $\sim 1.5 \times 10^{-3}$ electrons emitted every 25 ns by the photocathode.

2.3.3 LHCb Pixel HPD electron optical system. Point spread function and sensitivity to magnetic flux density

The LHCb Pixel HPD (Fig. 2.1 on page 25) is a cross focusing tube with a cathode to anode size demagnification factor around 5.

The HPD electrodes are made of Kovar[13] and their nominal voltages are -20 kV (photocathode), -19.7 kV (focusing electrodes), -16.4 kV (zoom electrodes) and the anode at ground. The cathode area (72 mm) is mapped, using these voltages, onto a circular area of ∼12.7 mm diameter, fully contained on the square 16 mm silicon detector. The simulation of the electron trajectories (cf. Fig. 4.1 on page 81) gives a point spread function with transverse RMS

[13]Kovar®: ferromagnetic alloy, 54% Fe, 29% Ni and 17% Co. Its thermal expansion coefficient matches that of hard borosilicate glass, making it a preferred glass sealing alloy.

Thickness	[μm]	300
Depletion voltage	[V]	12
Nominal operating voltage	[V]	80
Breakdown voltage	[V]	>120
Bulk resistivity	[Ω·cm]	25000
$N_{D,eff}$ (*)	[cm^{-3}]	$1.75 \cdot 10^{-11}$

Table 2.3: Summary of the main properties of the LHCb Pixel HPD silicon sensor. (*) The efficient donor concentration was calculated from the bulk resistivity.

dimensions $\sigma_x \simeq \sigma_y \simeq 160$ μm [20].

The electrons must travel on relatively long trajectories from the emission point to the impact point with the cross focusing geometry. Therefore the focusing system is sensitive to an external magnetic field. The photoelectron trajectories may be significantly changed by the component of Lorentz force due to magnetic field $\mathbf{F} = e\mathbf{v} \times \mathbf{B}$, resulting in the distortion of the point to point correspondence between cathode and anode. The spatial resolution is consequently affected. The reader is referred to Chapter 4 for the detailed study of this phenomenon and of the solutions developed.

The vacuum inside the tube is not perfect. The residual pressure is due to the manufacturing vacuum level, outgassing of the components and permeability to gas of the entrance window[14]. A residual molecule can be ionized by an accelerated photoelectron. The positive ion is then accelerated toward the cathode causing an abundant emission of electrons (*back pulse* or ion-feedback), observed as a large cluster of hits on the anode and constituting a source of positive feedback that is to be minimized. A countermeasure is to put inside the tube a material acting as *getter*, i.e. adsorbing molecules. However, this was not felt necessary for the LHCb Pixel HPD.

2.3.4 The anode assembly

The anode of the LHCb Pixel HPD is a hybrid pixel detector (cf. Section 2.2.4). A detailed description is given in [21]. Each pixel of the silicon sensor is 500×62.5 μm^2. Other electrical characteristics are summarized in Table 2.3.

The pixels are electrically connected via the solder bumps to the inputs of the circuitry on the readout chip. The bump-bonded chips are glued onto a ceramic carrier and the readout chip is wire bonded to the carrier pads. This

[14]The permeability of fused silica to helium is $\sim 3.75 \times 10^{-14}$ $\left(\frac{cm^3(STP)}{s}\right)\left(\frac{mm}{cm^2 Pa}\right)$. Due to the diffusion of atmospheric helium through the HPD window, the partial pressure inside the tube could increase of $\sim 1.33 \times 10^{-3}$ Pa $\simeq 1 \times 10^{-5}$ mmHg every 1.3 years. Storage and operation of the Pixel HPD in low helium content environment are foreseen.

constitutes the anode assembly of the device. The pins of the carrier are the electrical interface with the external world, through which the binary data of the pixel hits are read out. The remaining pins serve for control signals and bias lines.

The standard solder bump bonding process is done with eutectic SnPb (63% Sn, 37% Pb) which has a melting point temperature of 183 °C. This temperature is not compatible with the LHCb Pixel HPD manufacturing process that includes a 3 hour long bake out at 300 °C before the cathode deposition. The silicon assembly anodes manufactured with the standard process were damaged during the bake out [18]. An important advance in the development phase of the LHCb Pixel HPD was to identify the problem and to substitute the standard eutectic solder with one with a higher Pb content[15]. This results in a higher melting point temperature, compatible with the subsequent bake out phase.

2.3.5 LHCBPIX1 readout chip

The readout chip of the LHCb Pixel HPD hybrid anode is conventionally called LHCBPIX1 [21]. It is a mixed signal chip realized in a commercial 0.25 μm CMOS technology, containing around 13 million transistors. Special layout techniques improve the tolerance to radiation. It consumes 1.8 W operating at the nominal 40 MHz clock frequency and 1 MHz trigger rate. The pixel matrix is made up of 8192 readout channels arranged in a matrix with 256 rows and 32 columns. Each channel occupies an area of 500×62.5 μm^2, corresponding to a pixel on the detector. The total active area is 16×16 mm^2.

Digital logic allows to form a logical OR of the hit information from 8 adjacent pixels on a same column, thus forming a *super-pixel* of 500×500 μm^2. This mode of operation is called LHCb mode, whereas the full resolution one ALICE mode. In this way the equivalent pixel size on the entrance window is increased to 2.5×2.5 mm^2, fully satisfying the requirement for the LHCb RICH detectors. Two side advantages are obtained with this approach: neither the capacitance at the input of each channel nor the channel occupancy are increased.

The readout channel

The pixel channel is divided into an analog and a digital part, as shown in Fig. 2.15. The analog front-end is constituted by a charge sensing amplifier followed by two shapers. Details are given in [22]. The ideal pulse response of

[15]The bump bonding process is carried out at VTT Information technology, Microelectronic, Finland

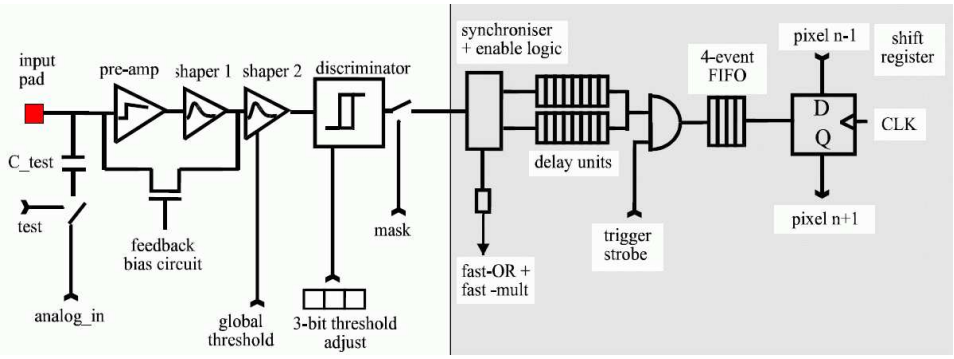

Figure 2.15: Block diagram of a single readout channel of the LHCBPIX1 chip.

the analog section is shown in Fig. 2.16, together with the response to input current pulses calculated as discussed in Section 18.

A test charge pulse can be applied to the input of the pre-amplifier using a voltage step applied across a capacitor. A discriminator compares the analog output of the shaper with a threshold. The threshold can be regulated globally across the chip (8 bit DAC) and finely for each pixel channel (3 bit DAC). The test pulse is used to evaluate and calibrate the threshold setting. The discriminator output is fed into the digital part of the cell, after being synchronized to the following rising edge of the chip clock (Fig. 2.16). The hit information is binary from this point onward and data are constituted by the binary values indicating the recording of a pixel hit.

The digital section stores the binary hit until the arrival of a trigger (*strobe*) pulse. The triggered events are buffered and stored in a four locations FIFO register. The binary pixel hit map of an event stored in the FIFO is read out via 32 digital lines, one per column. A clock synchronous shifting scheme is adopted for each column. Therefore the readout scan of the full set of rows takes 256×25 ns $= 6.4$ μs in ALICE mode and 32×25 ns $= 0.8$ μs in LHCb mode.

Detection efficiency

The conditional probability of recording a hit given a photoelectron impinging on a pixel will be called *detection efficiency*. This probability constitutes an important performance figure of the silicon assembly and should be as close as possible to unity.

The statistical fluctuation of the signal pulse amplitude at the shaper output and the noise limit the detection efficiency. Back scattering and lateral diffusion cause the fluctuations of the total charge injected and of the fraction of charge collected at the pixel pad (Section 2.2.3). The shaper output pulse

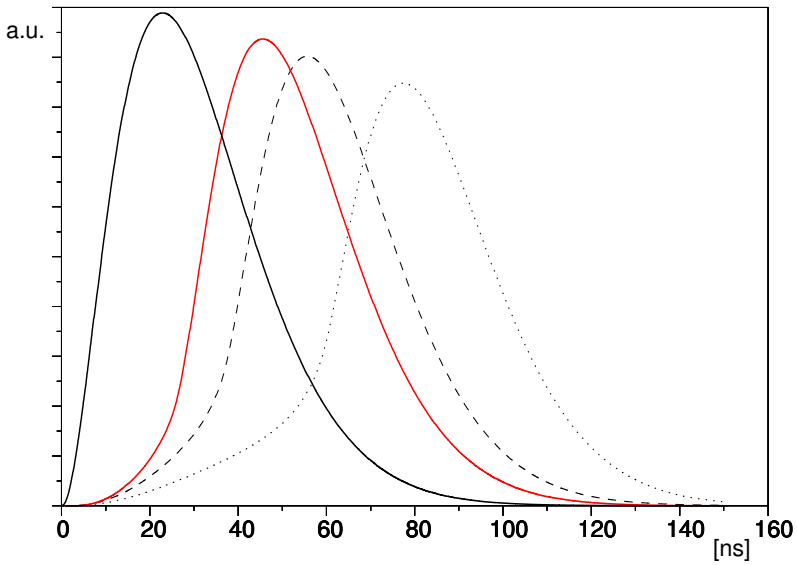

Figure 2.16: Pulse response of the LHCBPIX1 analog section. The leftmost curve is the ideal pulse response, calculated from the design transfer function. The following three curves were calculated for an input current pulse due to charge drifting in the sensor biased at 80 V, 55 V and 35 V respectively, following the discussion of Section 18.

amplitude changes proportionally. The discriminator threshold level cannot be set arbitrarily close to the baseline of the shaper output because of the noise. Therefore a fraction of events has a pulse amplitude that does not reach the discrimination level and is not detected.

In order for a hit to be recorded in the output FIFO, a fixed latency of an integer number of clock periods must elapse between the synchronized discriminator output transition and the strobe pulse. The latency duration is controlled by a register on the chip. This is to allow for any trigger latency. In order to detect the hit, the asynchronous discriminator commutation instant must fall in the clock period before the synchronizing clock edge. The fluctuation of the pulse amplitude implies a variation of the discriminator commutation time (*time walk* effect) as illustrated in Fig. 2.17. The delay between the photon hit and the discriminator commutation instant is then a random variable. Therefore, it exists an optimal phase delay between the photon hit and the clock that maximizes the detection efficiency.

As the cathode to anode voltage drop determines the average amount of charge injected in the sensor, the silicon detector reverse bias voltage influences the signal current pulse shape, duration and amplitude (cf. Section 18), affecting in their turn the output of the shaper.

Summarizing, the detection efficiency depends not only on the discrimina-

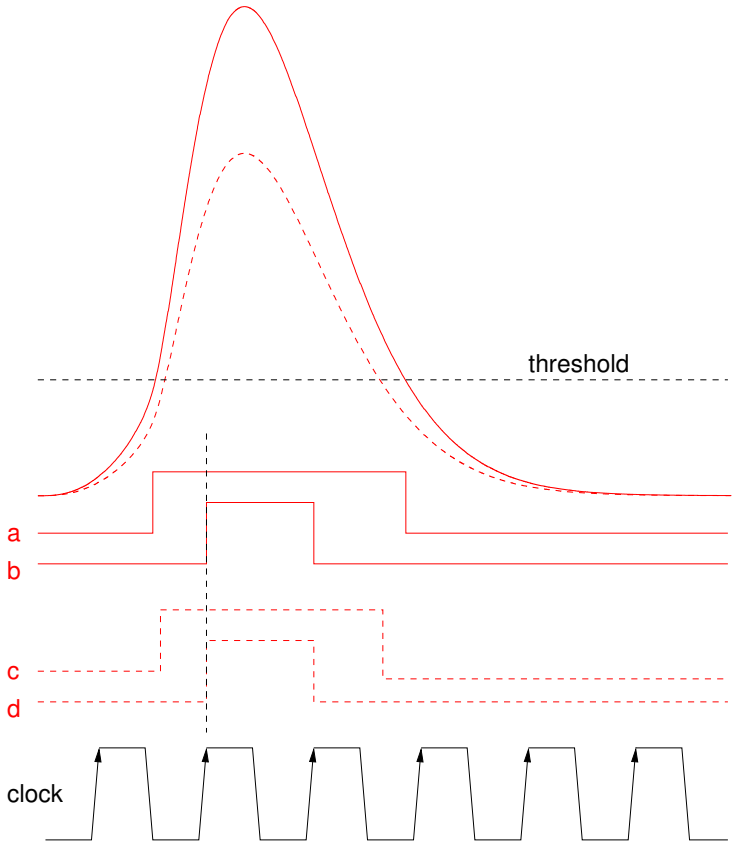

Figure 2.17: Illustration of the detection process. Two shaper pulses are shown. The amplitude of the smaller is 70% of the larger one. Signal a (c) is the output of the discriminator for the larger (smaller) pulse; b (d) is the corresponding synchronized version. The synchronizing clock transition is shown. The shaper analog pulses were calculated according to the discussion of Section 18 and with the design LHCBPIX1 chip pulse response (Fig. 2.16).

tor threshold setting but also on the the cathode to anode high voltage drop, the silicon detector bias voltage and the delay between the photon hit and the clock. An experimental study of these dependencies will be discussed in Section 2.4.2.

Charge sharing

Due to lateral diffusion of injected carriers, the pixel pads adjacent to the one hit by the photoelectron can collect enough charge to bring the discriminator above threshold (Section 18). A hit may be recorded also in these pixels. This effect tends to increase the number of recorded hits with respect to the number of photoelectrons, detecting clusters of two or even more adjacent pixels in correspondence of a single photoelectron. The statistic of this random process depends on the operating parameters and requires an experimental characterization. Nevertheless, an estimate of the effect can be tried under a few (strongly) simplifying assumptions.

Consider a single dimensional arrangement of pixel pads of width D, as in Fig. 2.18. A photoelectron hits the region above pixel k. At the end of the drift the concentration of the charge has a Gaussian shape of width σ. The median of the distribution is in correspondence of the hit position at a distance ξ from the edge between pixels k and $(k+1)$. Let us assume that the charge collected by each pad is equal to the integral under the gaussian distribution between the pad edges. The fraction of charge f collected by pixel $k+1$ is readily obtained:

$$f(\xi) = \int_{\xi}^{\infty} \frac{1}{\sqrt{2\pi}\sigma} \mathrm{e}^{-\frac{x^2}{2\sigma^2}} dx = \frac{1}{2}\mathrm{erfc}\left(\frac{\xi}{\sqrt{2}\sigma}\right), \tag{2.36}$$

having introduced the complementary error function[16]. The hit in pixel $k+1$ under the condition of a photoelectron impinging above pixel k is obtained when the fraction of charge collected reaches a threshold value f_{tr}. In the simplified picture this happens when the photoelectron hit is closer to the edge than the distance ξ_{tr} for which:

$$f(\xi_{tr}) = f_{tr} \rightarrow \frac{1}{2}\mathrm{erfc}\left(\frac{\xi_{tr}}{\sqrt{2}\sigma}\right) = f_{tr}. \tag{2.37}$$

Assuming a uniform distribution of the photoelectron hit position in the range [-D/2;D/2], the conditional probability P($double|k$) of having two adjacent hits due to a single photoelectron above k is given by:

$$\mathrm{P}(double|k) = 2\mathrm{P}(k+1|k) = \frac{2\xi_{tr}}{D}, \tag{2.38}$$

[16]It is, by definition, $\mathrm{erfc}(\xi) = \frac{2}{\sqrt{\pi}} \int_{\xi}^{+\infty} \mathrm{e}^{-x^2} dx$.

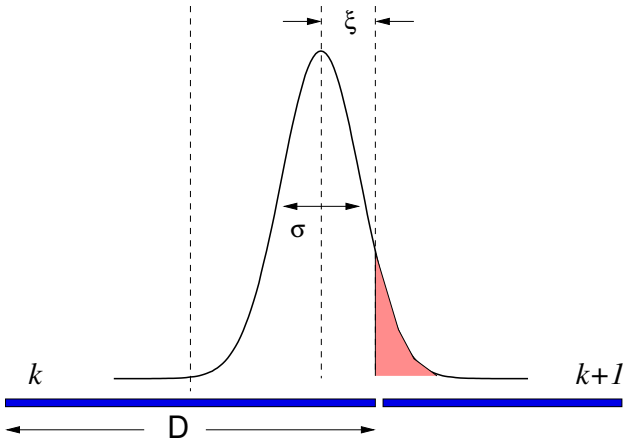

Figure 2.18: Illustration for the estimation of the probability of the amount of double pixel clusters due to charge sharing.

where $P(k+1|k)$ is the conditional probability of having a hit in $k+1$ given the photoelectron above k.

Let us assume $f_{tr} = 1/4$ of the total injected charge (unitarian in this model). Substituting into Eq. (2.37) and Eq. (2.38) the numerical values appropriate for the LHCb Pixel HPD silicon detector (D=62.5 μm and $\sigma = 7.6$ μm for V_b=80 V, see Fig. 2.9 on page 39) one obtains $P(double|k) \simeq 0.16$.

2.4 Measurements of the LHCb Pixel HPD detection performances

2.4.1 Quantum efficiency measurements

The quantum efficiency curves of various LHCb Pixel HPD prototypes were measured at different times from their manufacturing. These measurements were made to verify the obtained radiant sensitivity, to investigate variations between prototypes and to study a possible evolution of the characteristics with time.

The setup used is shown in Fig. 2.19. It allowed a measurement of the HPD cathode photocurrent under illumination with a monochromatic beam of light of known intensity. The light from a Xenon arc lamp was filtered in wavelength with a 1 nm spectral resolution monochromator. It was collimated on the HPD entrance window or on a calibrated photodiode for the determination of its intensity. A small mirror could be rotated to direct the light onto the HPD or onto the photodiode.

The photocurrents were measured with an ammeter with a sensitivity of

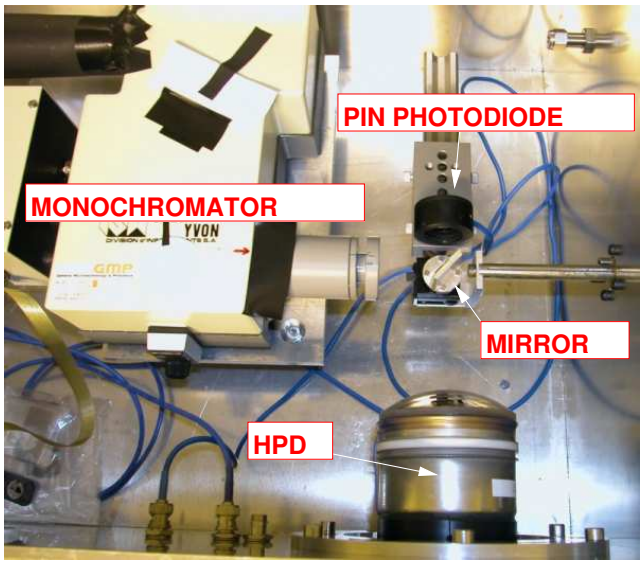

Figure 2.19: Picture of the set-up for measuring the HPD quantum efficiencies.

one picoampere. A voltage could be applied between the HPD cathode and all other electrodes connected to ground (cf. Fig. 2.1(b) on page 25). The maximum achievable ground to cathode voltage drop was 500 V. The ammeter was in series with the photocathode and floating at the bias potential during the HPD current measurements. The photodiode was operated in photoconductive mode, with constant 0 V bias voltage. The stability of the light intensity was continuously verified. Dark current levels were measured and subtracted from data.

Light absorption in the entrance window reduces the intensity reaching the photocathode, as do the reflections at the window outer and inner surfaces. Therefore the radiant sensitivity measured is the overall response including these losses. The measurements were repeated illuminating different positions of the photocathode and excellent spatial uniformity of the response was observed with negligible variations from point to point.

Radiant sensitivity curves are shown in Fig. 2.20 for five tubes. The corresponding quantum efficiency curves are given in Fig. 2.21. Data points are equally spaced by 5 nm in wavelength. Error bars were determined by considering the errors of the photocurrent measurements. The larger errors in the ultraviolet region are due to the lower light intensity and to the smaller photodiode responsivity, both resulting in smaller currents (0.1 nA) below 300 nm. This implies a relatively larger effect of the dark current subtraction, the pick-up noise and the resolution of the ammeter.

Three HPDs satisfy the specification on quantum efficiency (cf. Table 2.2). Two tubes (3_1, Tube 9) do not satisfy it, being just at the limit. Both

have QE=0.15 at 400 nm and tube 3_1 reaches 0.19 at 270 nm. Other four prototypes were measured and their sensitivity is situated between the two upper curves and the lower three of the plot. They all satisfied the requirement on quantum efficiency.

All curves are compatible with the typical multi-alkali photocathode data available in literature and from data sheets of manufacturers. A significant spread of characteristics between the HPD prototypes was measured. Two of the devices (3_2, 4_5) showed very high sensitivity in the 250-400 nm region, above the typical multi-alkali performance. Tube 3_2 shows a reduced sensitivity in the near infrared, while outperforming the other devices in the UV. Three other devices show a lower sensitivity below 400 nm, with tube 4_3 still peaking above 70 mA/W at 420 nm. Other four prototype HPDs presented a radiant sensitivity practically coinciding with the canonical response of S20 cathodes.

The reason for the differing responses in the UV is not clear. It can be attributed to variations in the stoichiometry or in the crystalline structure of the photocathodes, requiring an improvement of the control of the deposition process. The spread of absorption curves of the entrance windows could play a role in determining the tube by tube variations. However, absorption curves of synthetic silica do not present variations between 300 and 400 nm like those exhibited in the measurements. Significant variations of the photocathode thickness could have an effect, but this parameter should be well controlled. Feedback to the partner industry was provided to improve control of the manufacturing process and achieve better uniformity between the tubes.

2.4.2 Detection efficiency measurements

To evaluate the detection efficiency it is necessary to measure simultaneously the number of photoelectrons hitting the silicon sensor and the number of recorded hits. Details are given in [19]. A detection efficiency of 88% was measured under optimal operating conditions (-20 kV cathode to anode voltage and optimal threshold setting).

The dependence of the detection efficiency on the operating settings is rather complex because of the interplay between the fluctuations of injected charge, the amplitude of the analog signals, the threshold discrimination level and the synchronization with the digital clock. This was discussed in Section 2.3.5. Measurements of the relative variations of detection efficiency with respect to high voltage, threshold setting, silicon detector bias were made in a dedicated set-up.

A fast pulsed solid state ∼630 nm laser was used to illuminate the HPD

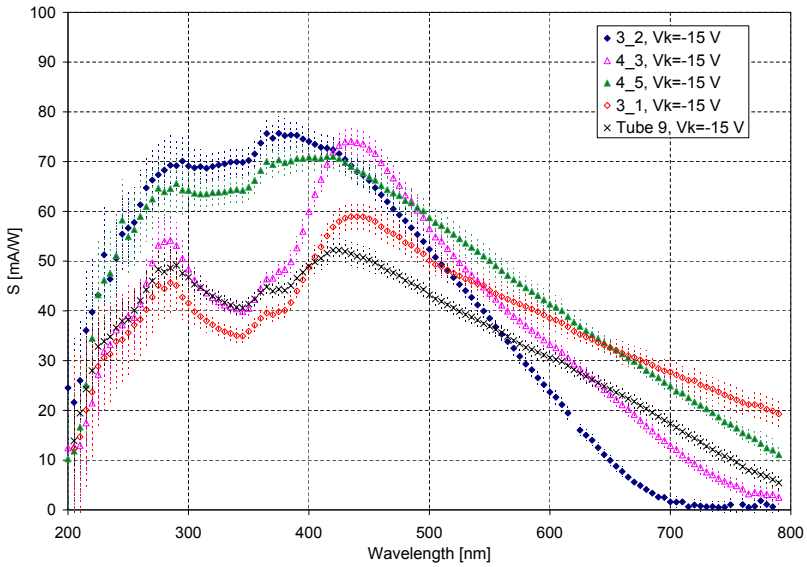

Figure 2.20: Radiant sensitivities of 5 prototype HPDs. Measurements include the absorption in the entrance window.

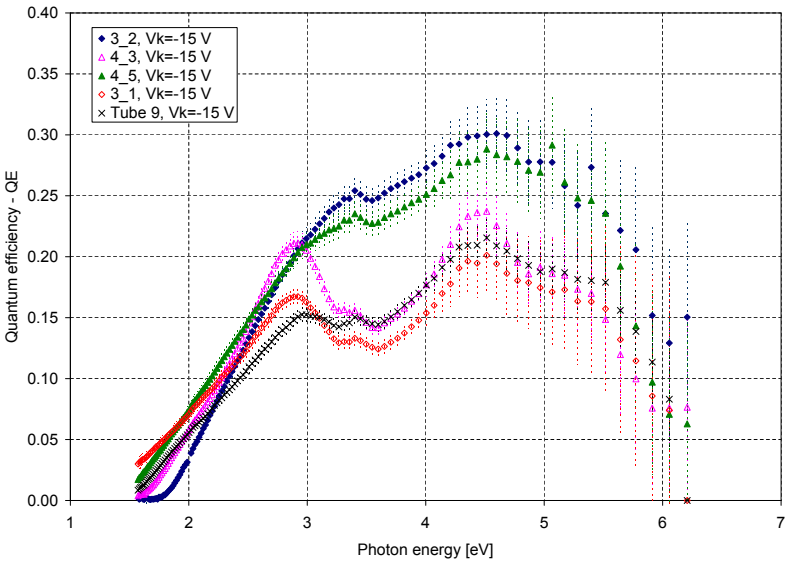

Figure 2.21: Quantum efficiencies of 5 prototype HPDs as a function of photon energy. Measurements include the absorption in the entrance window.

on a circular region of ∼20 mm diameter centered on the window. The pulse duration was ≃150 ps, for all practical purposes instantaneous with respect to the LHCBPIX1 integration time. The source was strongly attenuated in order to have on average ∼0.4-0.5 recorded hits per pulse with the optimal settings.

The light pulse was triggered by a signal synchronized with the clock of the readout chip. This allows to regulate the timing of the light pulse with respect to the clock period in which the signal is expected to arrive, determined by the strobe pulse.

100000 events (light pulses) were triggered and recorded for each of the operating settings. The average number $< N_h >$ of photoelectron hits per event was evaluated. A correction for the clusters due to charge sharing was applied. All double pixel clusters were counted as a single photoelectron hit. The number of clusters with more than two hits was negligible. There was no risk of overcorrection, given that the probability that these clusters originated from two photoelectrons hitting adjacent pixels was negligible: the mean number of photoelectrons was very small and they were spatially spread on more than 100 pixels.

A fraction of ∼15% of double pixel clusters was measured at the nominal settings. This value is in good agreement with the previous measurements [19] and with the estimation of Section 2.3.5.

Fig. 2.22 shows two sets of measurements of the average number of hits recorded as a function of the light pulse time delay. Results are shown as a function of the delay between the clock and the light pulse, indicated with Δt in the abscissa of the plots. Each curve is taken with the same high voltage, silicon bias and threshold setting. They differ for the duration of the strobe pulse that is sent to the pixel chip to store the recorded hit in the output FIFO register. The reduction of the strobe length does not cause a reduction of the detection efficiency. With the 25 ns strobe duration, however, the time setting to maximize the detection efficiency must be tuned with higher accuracy. The estimated slope between the peak value and the data point at 140 ns implies a reduction of the detection efficiency of 0.25%/ns.

Fig. 2.23 shows a set of measurements with different cathode to anode high voltage settings. Reducing the high voltage the optimal delay reduces. This is due to the reduction of the amplitude and the slope of the rising edge of the shaper output, translating in a shift of the discriminator transition later in time. The light pulse must then come earlier to compensate for the shift. With the settings used, changing the cathode voltage from -19.2 kV to -17.8 kV gave no appreciable reduction in detection efficiency. In the range from −19.2 to −16 kV the reduction of the (peak) detection efficiency is ∼0.7%/kV. A further reduction of 6.5% was measured setting the high voltage to -12 kV.

The non linear behavior due to the timing effects is evident by comparing

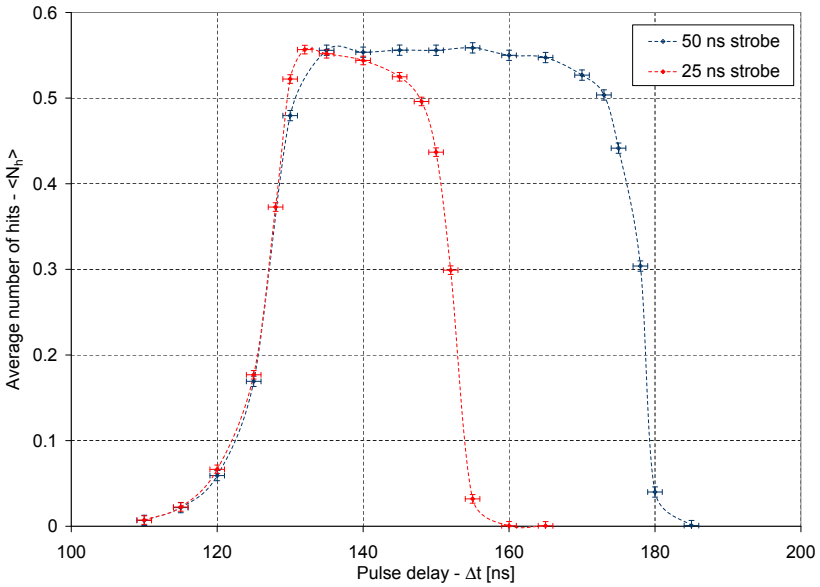

Figure 2.22: Average number of recorded hits $< N_h >$ vs. delay of the light pulse with respect to a trigger synchronous with the clock. Cathode to anode voltage: -19.2 kV. Silicon detector reverse bias: 80 V. Discriminator threshold equivalent to 1180 e.

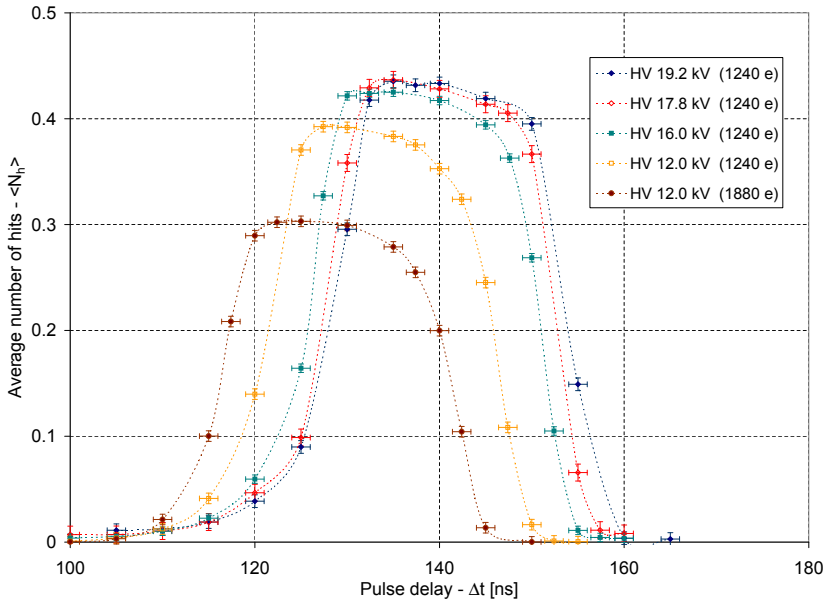

Figure 2.23: Average number of recorded hits $< N_h >$ vs. delay of the light pulse with respect to a trigger synchronous to the clock. Anode to cathode voltages and equivalent discriminator thresholds are given in the legend. Silicon detector reverse bias: 80 V.

the two curves measured at -12 kV. They were taken with different discriminator threshold settings. While obviously the maximum detection efficiency decreases, there is a critical region of delay time for which the efficiency is higher with the higher threshold setting. This is not surprising realizing that increasing the threshold also shifts the discriminator transition later in time, bringing it back in the strobed clock period.

Fig. 2.24 shows a set of measurements of the average number of detected hits as a function of the light pulse delay for three different values of the silicon detector reverse bias voltage. The shift in time is related to the longer drift time of the holes in the silicon detector. This translates in longer current pulses, in turn implying a delayed shaper pulse. The reduction of the peak detection efficiency using a reverse bias voltage of 55 V instead of 80 V was smaller than the measurement error (1%).

The delay measured between the 80 V and the 55 V case is in good agreement with the calculation of the output of the shaper for the same values of detector bias voltages, shown in Fig. 2.16 on page 50. The measurement at 35 V shows a delay reduction larger than expected. Charge diffusion was neglected in the calculation and this could explain the difference.

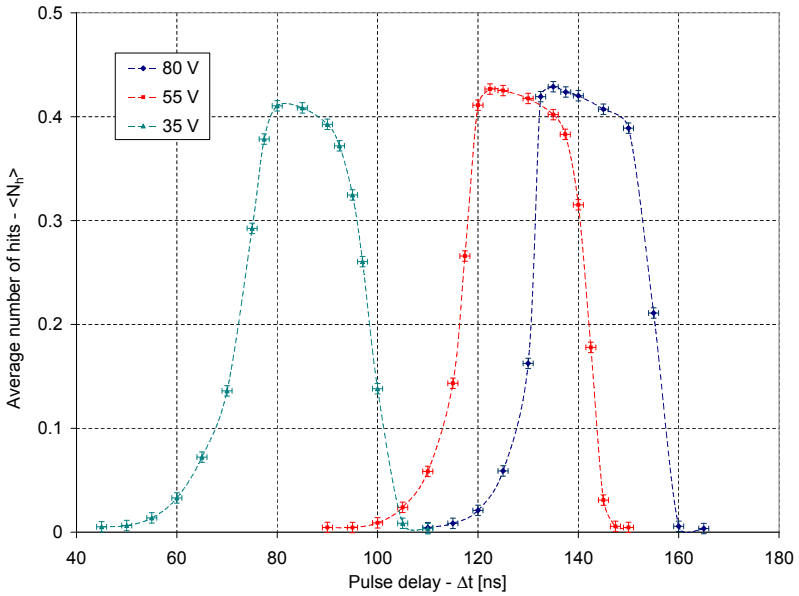

Figure 2.24: Average number of recorded hits $< \mathrm{N_h} >$ vs delay of the light pulse with respect to a trigger synchronous with the clock. Cathode to anode voltage: -19.2 kV. Equivalent discriminator threshold: 1240 e. Silicon detector reverse bias voltages given in the legend.

Bibliography

[1] R. Mirzoyan, *et al.*, "An evaluation of the new compact hybrid photodiodes r7110u-07/40 from Hamamatsu in high speed light detection mode", *Nucl. Instr. and Meth. A*, vol. 442, pp. 140–145, 2000.

[2] P. G. Kwiat, *et al.*, "High-efficiency single-photon detectors", *Phys. Rev. A*, vol. 48, no. 2, pp. R867–R870, August 1993.

[3] R. DeSalvo, *et al.*, "First results on the hybrid photodiode tube", *Nucl. Instr. and Meth. A*, vol. 315, pp. 375–384, 1992.

[4] T. Gys, *et al.*, "Position-sensitive single-photon detection with a hybrid silicon pixel array tube", *Nucl. Instr. and Meth. A*, vol. 387, pp. 131–133, 1997.

[5] V. P. Beguchev, *et al.*, "Optical and photoemissive properties of multialkali photocathodes", *J. Phys. D: Appl. Phys.*, vol. 26, pp. 1499–1502, September 1993.

[6] T. E. Everhart and P. . H. Hoff, "Determination of kilovolt electron energy dissipation vs penetration distance in solid materials", *J. Appl. Phys.*, vol. 42, no. 13, pp. 5837–5846, December 1971.

[7] H. Spieler, "Semiconductor Detectors, SLUO Lectures on Detector Techniques", Stanford Linear Accelerator Center, Tech. Rep., 1998, http://www-physics.lbl.gov/~spieler.

[8] C. A. Klein, "Bandgap dependence and related features of radiation ionization energies in semiconductors", *Journal of Applied Physics*, vol. 39, no. 4, pp. 2029–2038, March 1968.

[9] G. F. Knoll, *Radiation Detection and Measurement*, 3rd ed. John Wiley & Sons, 1999.

[10] G. Lutz, *Semiconductor Radiation Detectors*, 1st ed. Springer-Verlag, 2001.

[11] R. C. Alig, *et al.*, "Scattering by ionization and phonon emission in semiconductors", *Phys. Rev. B*, vol. 22, no. 12, pp. 5565–5581, December 1980.

[12] J. C. Barton, "Basic physics and statistics of photomultipliers, Tech. Rep. Technical reprint R/P063, http://www.electrontubes.com.

[13] C. D'Ambrosio and H. Leutz, "Hybrid photon detectors", *Nucl. Instr. and Meth. A*, vol. 501, no. 2-3, pp. 463–498, April 2003.

[14] C. P. Datema, *et al.*, "Hybrid photodiodes in scintillation counter application", *Nucl. Instr. and Meth. A*, vol. 387, no. 1-2, pp. 100–103, March 1997.

[15] Z. He, "Review of the shockley-ramo theorem and its application in semiconductor gamma-ray detectors", *Nucl. Instr. and Meth. A*, vol. 463, pp. 250–267, 2001.

[16] H. Spieler, "Front-end electronics and signal processing", in *Instrumentation in elementary particle physics, AIP Conference Proceedings*, vol. 674. American Institute of Physics, 2002.

[17] N. Wermes, "Trends in pixel detectors: Tracking and imaging", *IEEE Trans. Nucl. Sci.*, vol. 51, no. 3, pp. 1006–1015, June 2004.

[18] M. Campbell and al., "A fine pitch bump bonding process compatible with the manufacture of the Pixel-HPD's for the LHCb RICH detector", in *Proceedings of the NSS Nuclear Science Symposium.* IEEE, 2004, N16-108.

[19] M. Moritz, *et al.*, "Performance study of new pixel hybrid photon detector prototypes for the LHCb RICH counters", *IEEE Trans. Nucl. Sci.*, vol. 51, no. 3, pp. 1060–1066, June 2004.

[20] T. Gys, "HPD Point Spread Function numerical simulation", June 2005, private communication.

[21] K. Wyllie, *et al.*, "Silicon detectors and electronics for pixel hybrid photon detectors", *Nucl. Instr. and Meth. A*, vol. 530, pp. 82–86, June 2004.

[22] R. Dinapoli and et al., "An analog front-end in standard 0.25 μm cmos for silicon pixel detectors in ALICE and LHCb", in *Proceeding of the Sixth Workshop on Electronics for LHC Experiments.* CERN, 2000, CERN-LHCC-2000-041.

Chapter 3

Performance evaluation of the LHCb Pixel Hybrid Photon Detector in a beam test

3.1 A beam test with the LHCb Pixel Hybrid Photon Detectors

The performances of the first prototypes of the LHCb Pixel Hybrid Photon Detectors were tested in the October 2003 LHCb RICH beam test.

The experimental setup consisted of a Ring Imaging Cherenkov detector using nitrogen and silica aerogel as Cherenkov radiators and the prototype HPDs as photon detectors. It was installed in an experimental area at CERN and used to detect the Cherenkov photons generated by the particles of a beam crossing the radiators. The experimental runs with N_2 were used for the calibration and performance evaluation of the photon detectors.

This chapter describes the setup, the experimental method and the analysis of data of the N_2 runs. The detection efficiency and the angular resolution of the HPDs were evaluated with this experiment, in conditions similar to those that will be found in the LHCb RICHs.

3.1.1 The vessel, the Cherenkov radiators and the mirror

A picture and a scheme of the RICH detector used for the experiment are shown in Fig. 3.1 and Fig. 3.2. It consisted of a light tight and gas tight vessel containing the tiles of silica aerogel, nitrogen, a spherical mirror and three HPDs as photon detectors. The vessel was located in the T9 experimental

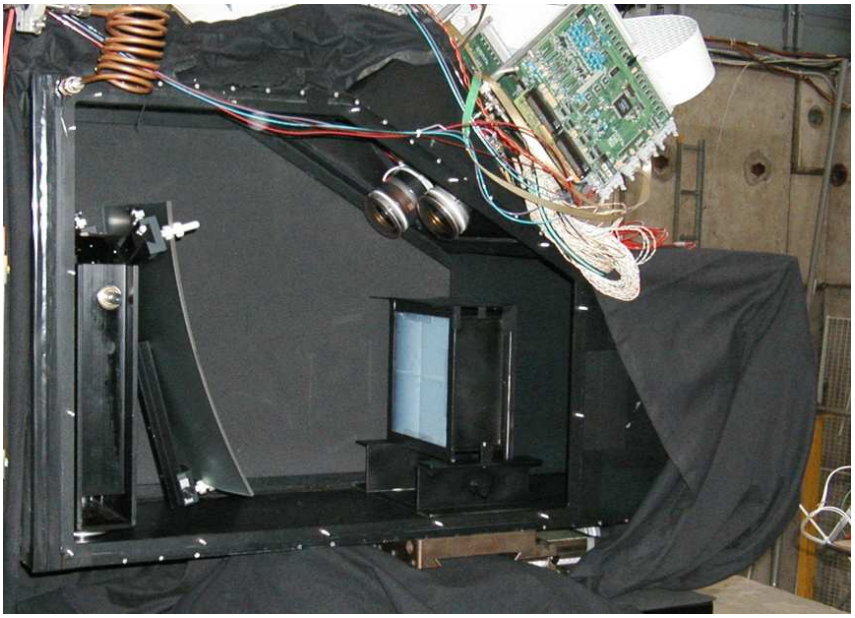

Figure 3.1: Picture of the light tight vessel with one side wall removed. The silica aerogel, the mirror and the two lower HPD detectors are visible, as well as an electronic board of the readout interface.

facility at CERN.

The particles crossed the vessel entering from the right hand side. They crossed the volume of nitrogen and the silica aerogel tiles, generating Cherenkov light, then the mirror. The distance between the entrance point and the mirror was L=103 cm. The Cherenkov photons were reflected by the spherical mirror and focused onto the photon detectors.

The Cherenkov emission angle was approximately 240 mrad for the aerogel (see Eq. (1.7) for $n_{agel} \simeq 1.03$ and $\beta = 1$) and the photons were focused on a ring spanning the three HPDs. The Cherenkov radiation emitted from the nitrogen between the aerogel and the mirror was normally focused in the insensitive region between the three photon detectors.

The silica aerogel tiles were removed during the calibration runs and the mirror was re-oriented to focus the Cherenkov light onto one of the three photon detectors in turn. The Cherenkov angle was ∼24 mrad in N_2 ($\beta = 1$) and the rings were, in this case, fully contained on a single HPD.

The mirror used in the setup had radius of curvature R=949 mm and featured a multiple layer dielectric coating (Ref. [1] and Chapter 5), with enhanced reflectivity in the UV region. The distance between the mirror and the lower HPDs was D=463 mm.

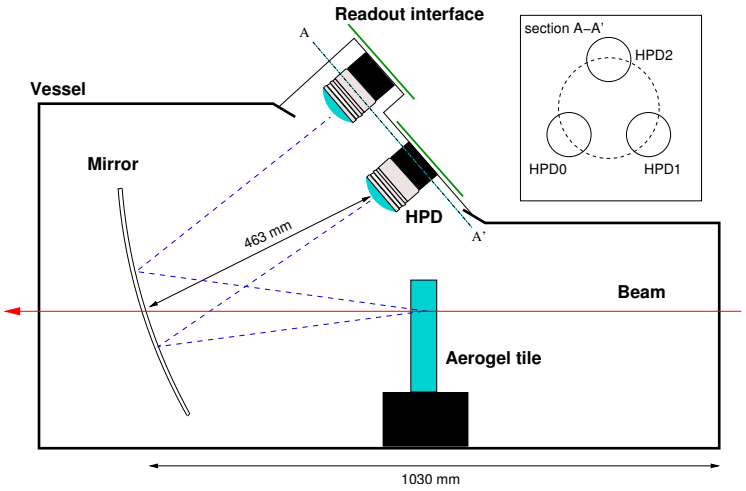

Figure 3.2: A schematic view of the light tight vessel used for the aerogel beam test.

3.1.2 The prototype Pixel HPDs of the beam test

The three prototype LHCb Pixel HPDs were located on the upper side of the vessel, at the vertices of an equal sided triangle (Fig. 3.2). The two lower HPDs were located symmetrically with respect to the middle vertical plane. They were labeled HPD 0 and HPD 1. The third HPD sat on the middle plane and was called HPD 2.

HPD 0 and HPD 1 were final prototypes with 32×256 pixels of 500 × 62.5 μm^2 as described in Section 2.3.4. They were the first prototypes of HPDs tested and could operate at 40 MHz. They were nevertheless operated with a 10 MHz clock due to limitations in the electronics of the readout system. HPD 2 was an older prototype with a different anode assembly. The dimensions of both the silicon pixel detector and of the readout chip were smaller in this device, featuring 32×256 pixels of 425×50 μm^2. Conventionally the terms columns and rows are used respectively to indicate the sets of 256 and 32 aligned pixels in the matrix.

3.1.3 The beam

A beam of charged particles originating from the the Proton Synchrotron (PS), one of CERN accelerators, was available in the experimental area. The beam was composed predominantly by pions with an admixture of electrons of about 4%. The momentum of the particles in the beam was determined by a momentum slit. Negatively charged particles of 10 GeV/c momentum were selected.

The beam used for the experiments is a secondary beam. A primary beam

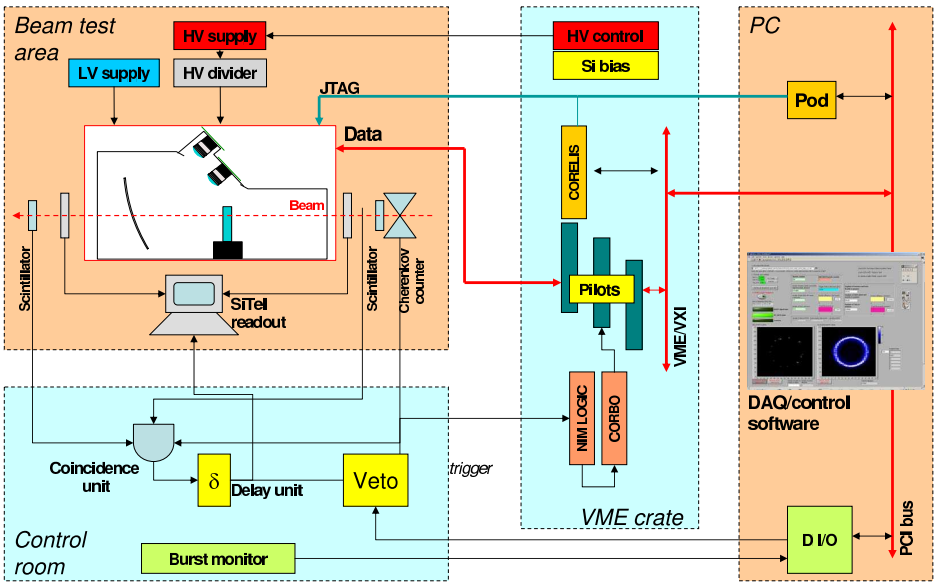

Figure 3.3: Scheme of the October 2003 LHCb-RICH beam test setup.

of protons is extracted from the PS machine and sent onto a fixed metal target. The target, 100 mm of Al followed by 3 mm of W acting as electron enricher, emits the secondary mixed π/e beam.

3.1.4 The trigger, readout and control systems

A schematic description of the entire setup, including the trigger, the readout and the control subsystems, is shown in Fig. 3.3.

The trigger for the readout was provided by the coincidence of the pulses, due to a crossing particle, of four aligned scintillators coupled to photomultipliers. Two scintillators of 1 cm^2 located $\sim$8 m apart limited the beam divergence to $\pm$1.25 mrad. A Cherenkov threshold counter could be optionally inserted in the trigger circuitry to discriminate between π and e.

The hardware and software [2] systems used for the HPD development and the previous measurements (Section 2.4.2) were modified to provide the readout and control of the tubes in the beam test.

The readout of the HPDs binary data was done through three electronic front-end boards (Pilot boards) interfacing to VME bus. The signals were transfered over $\sim$20 m between the beam area and the readout station. For each event the binary maps of the hits on the HPDs were read out and stored to memory. Each binary array was 256$\times$32 bits=1024 bytes plus a header and

Particle	Rest mass [MeV/c^2]	Momentum [GeV/c]	β
Pion, π	139.6	10	$1 - 9.74 \times 10^{-5}$
Muon, μ	105.6	10	$1 - 5.58 \times 10^{-5}$
Electron, e	0.511	10	$1 - 1.3 \times 10^{-9}$

Table 3.1: The values of β for different particles of 10 GeV/c momentum.

a trailer long words.

Data were read out during a beam spill, buffered in the memory of the Pilot boards and then transferred to the computer for storage, during the idle time between consecutive beam spills. Maps of recorded hits were also displayed on three histograms on the readout software interface.

A veto signal from the readout computer and a beam monitor signal were connected to the trigger circuitry for synchronization. Only after the data storage was completed the computer allowed for more readout pulses to be sent to the HPDs by releasing the veto signal. At the end of a beam spill period, marked by the beam monitor signal, the software read out the data from the memory of the front-end boards to the computer memory and to disk. A read out rate of few kHz could be achieved during the beam spill.

Calculation in real time of event and pixel occupancy, allowed the software to act as an online monitor during data acquisition. Software routines were developed for the offline conversion of the raw binary data to other formats and for offline analysis.

A control system was used to allow the control of the three HPD chips and of the respective biasing circuitry using JTAG standard. All the necessary supply voltages for the proper biasing of the HPDs were provided. The three high voltages for the HPD tube electron optical system were obtained by a resistive voltage divider. The HPD cathodes were biased at -18 kV, instead of the nominal -20 kV, due to non optimal high voltage insulation in the setup.

3.2 Expected photoelectron yield and Cherenkov angles in the N_2 calibration runs

The Cherenkov angle and the photon yield are determined by the velocity β of the particle, according to Eq. (1.7) and (1.10). Values of β calculated with Eq. (1.22) are summarized in Table 3.1. Pions, muons and electrons of 10 GeV/c momentum are considered. The momentum spread of the particles (0.5%) is neglected in the following analysis.

HPD	N_{pe}		θ_c [mrad]	
	π	e	π	e
HPD 0	9.6±0.75	14.6±1.14	19.33±0.7	23.84±0.7
HPD 1	8.7±0.68	13.3±1.04	19.36±0.6	23.86±0.4

Table 3.2: Expected photoelectron yields, average and RMS Cherenkov angle for 10 GeV/c pions and electrons in two HPDs.

3.2.1 Photon yield

Eq. (1.19) can be used to calculate the average number of photoelectrons generated in a given HPD per event.

The radiator length is $L = 103 \pm 1$ cm. The index of refraction of N_2 is described by Eq.(1.25). The temperature and pressure measured in the vessel were p=97000 Pa and T=293 K. Optical absorption in N_2 is neglected. The reflectivity of the mirror had been measured with a reflectometer.

The curves of the quantum efficiency of the 40 MHz HPD prototypes are shown in Fig. 3.6. The light reflections at the boundaries of the quartz entrance window and the light absorption in quartz are implicitly folded in the curves. Numerical integration of Eq. (1.19) gives the expected average photoelectron yields. The results are summarized in Table 3.2.

An uncertainty of ±8% is estimated for the calculations, resulting from the quadrature sum of the uncertainties on the various measurements: 2% for the trajectory length and the refractive index and 5% for the reflectivity curves and quantum efficiency. A numerical integration error of ∼2% was included due to the sensitivity to the lower integration limit, where the QE curves have to be extrapolated.

3.2.2 Expected Cherenkov angles

Each of the detected photoelectrons corresponds to a photon emitted at a certain angle. The distribution of the Cherenkov angles of the detected photons is given by Eq. (1.18), plotted in Fig. 3.5 after multiplication for the radiator length. The distribution of the emission angle of the detected photons is determined by the speed of the particle, the index of refraction (chromatic aberration) and also by the detector spectral response. The averages and RMS deviations of the angular distributions are listed in Table 3.2.

The dip in the angular distribution is related to the dip in the quantum efficiency curve. The smaller angles correspond to longer wavelengths. The oblique incidence and the refraction at the entrance window are neglected.

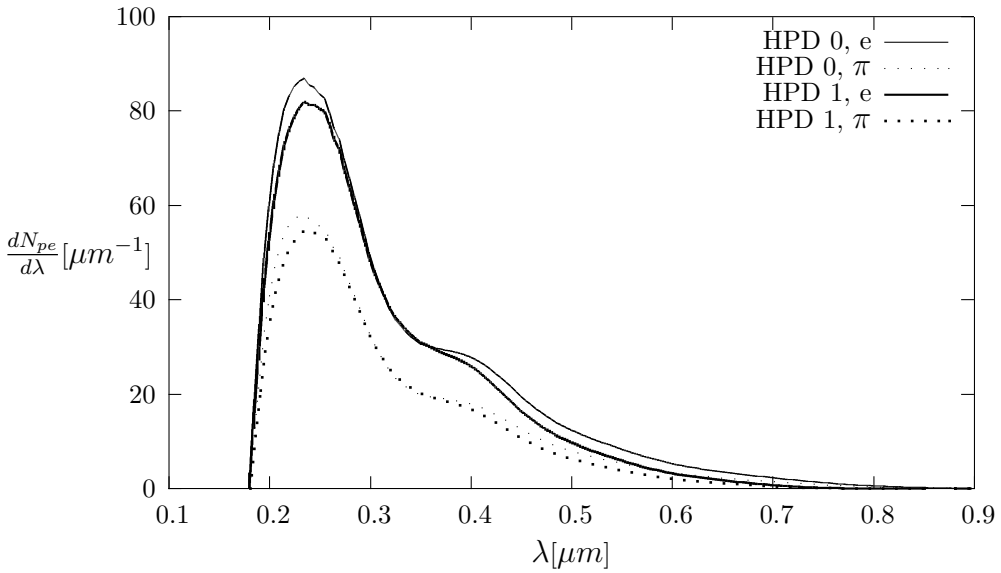

Figure 3.4: Spectral density of the expected number of photoelectrons. The integrand of Eq. (1.19) is plotted for the two HPDs and 10 GeV/c pions and electrons in nitrogen.

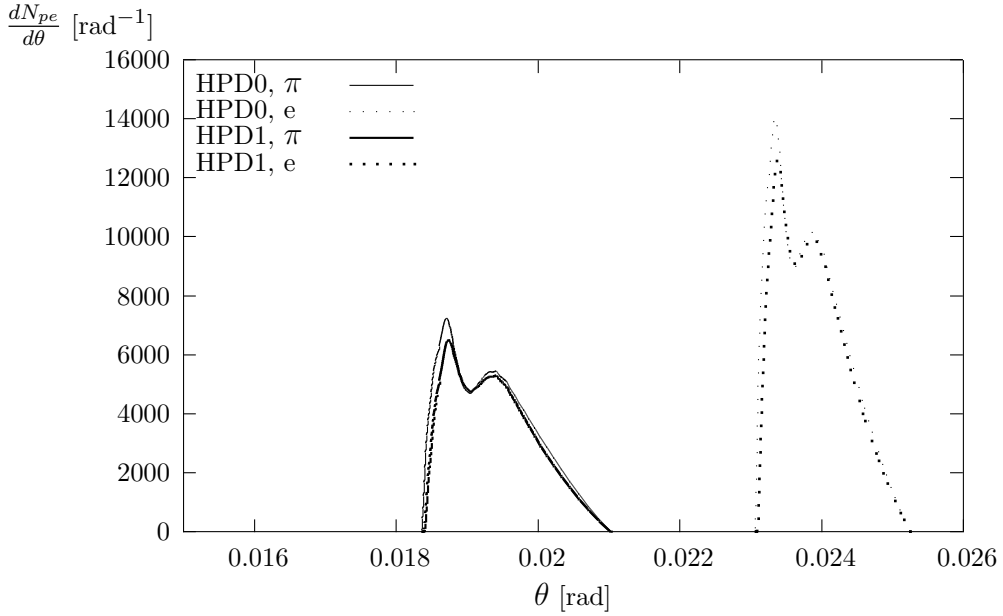

Figure 3.5: Distribution of the number of photoelectrons with respect to the angle of the originating Cherenkov photon, for HPD 0 and HPD 1 and for pions and electrons.

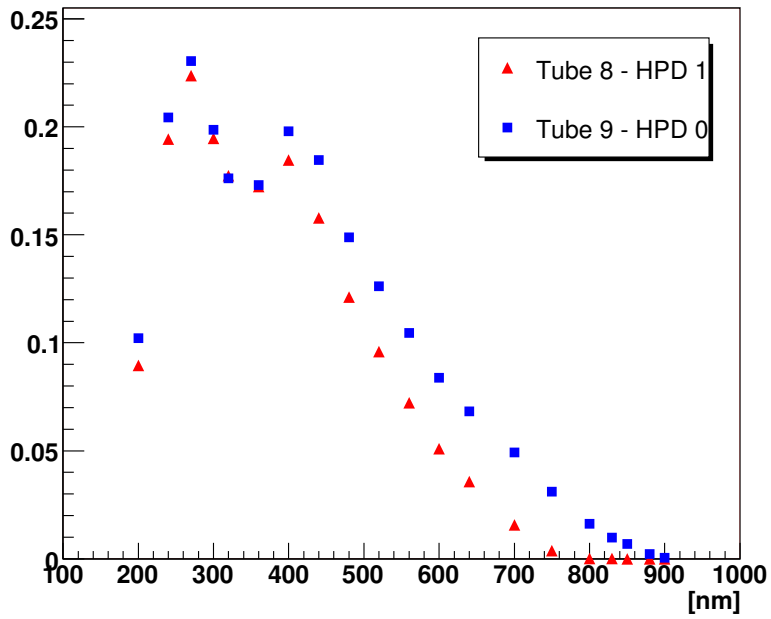

Figure 3.6: Quantum efficiency curves for two of the three HPDs used in the beam test. Measurements for HPD 0 and HPD 1 were done by the industrial partner.

3.3 Analysis of the nitrogen runs data

Three experimental runs were taken using only N_2 as Cherenkov radiator, each with around 50000 recorded events. The Cherenkov radiation was used in this case as a reference pulsed light source for the evaluation of the detection efficiencies of the HPDs. The detection efficiency is defined as the conditional probability that a pixel hit is recorded given a photoelectron impact on the pixel (see Section 2.3.5). The calibration based on the N_2 runs was later used for the analysis of the runs with silica aerogel as radiator.

Fig. 3.7 shows the histograms of the pixel hits on the anodes of HPD 0 and HPD 1. The shape of the distributions are only approximately circular. An analytical determination of the exact shape is complex and should include the spherical aberration due to the mirror tilt angle, the refraction of the photons at the spherical window and the electrostatic mapping properties of the HPD electro-optical system.

The particles cross the radiator with straight trajectories distributed around the nominal beam line. The distribution of the angles of the trajectories (beam angular divergence) implies that the centre of the ring on which the photons hit the focusing surface changes event by event. The histogram of the hits is smeared by this effect.

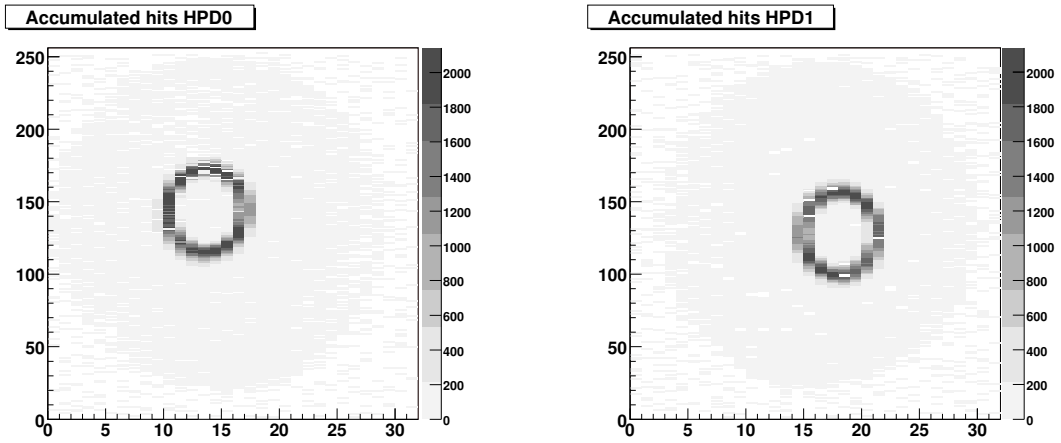

Figure 3.7: Histograms of the hits on HPD 0 and HPD 1, runs with N_2, ∼50000 events.

3.3.1 Evaluation of charge sharing

Charge sharing (Section 2.3.5) increases the number of recorded pixel hits with respect to the number of photoelectron hits. A single photoelectron can generate clusters of adjacent pixel hits instead of single hits. Only the probability of a photoelectron giving clusters of two hits (*double clusters*) is significant, while it is negligible for clusters of larger size. Double clusters of two hits on the same row (sharing a short side) or column (sharing a long side) are called horizontal or vertical respectively. The probability of the effect depends on the operating settings and can be measured on data by the frequency of double clusters in a set of events characterized by single photoelectron hits.

For each of the HPDs two background runs are available with the mirror focusing onto the other two tubes. The hits in these runs can have different origins: diffused photons, corona discharges[1], ion-feedback (Section 2.3.3) and thermal emission from the photocathode (*dark counts*). Discharge or ion-feedback events are characterized by a large number of photoelectrons and have to be excluded from the set of events to analyze. Their signature is the recording of a large number of pixel hits.

Table 3.3 gives the event counts in the background runs. The events with more than 2 hits, including those possibly due to discharge or ion-feedback, are less than 0.2% of the total. The largest fraction of events can contain hits only due to thermally emitted photoelectrons or from diffused or reflected photons converted at the photocathode. Assuming that the number of photoelectrons per event per HPD are Poisson distributed, an upper limit to their average

[1]Electrical discharges due to the high electro-static field on the outer surface of electrodes of the tube. A glowing plasma may be formed in the proximity of the electrodes.

HPD	Focusing on	Number of events			
		Total	$N_h = 0$	$1 \leq N_h \leq 2$	$N_h > 2$
0	1	50013	49094	895	24
0	2	50160	44372	5692	96
1	0	50023	49265	738	20
1	2	50160	49323	818	19

Table 3.3: Event counts in background runs. N_h indicates the number of pixel hits in an event. Number of events with 0, 1 or 2 and more than 2 pixel hits are detailed. The larger background measured in HPD 0 while focusing on HPD 2 is not understood.

HPD	Focusing on	N_h	N_{cl}	N_{hor}	N_{ver}
0	1	1042	967	7	66
0	2	6700	6230	36	428
1	0	903	796	16	89
1	2	973	848	14	108

Table 3.4: Counts of clusters in background runs. N_h: total number of hits. N_{cl}: sum of the numbers of single pixel hits and double clusters. N_{hor}, N_{ver} number of horizontal and vertical double clusters.

can be determined by the frequency of events with no recorded hits:

$$< N_h >= -\ln P(N_h = 0) \leq 0.123. \tag{3.1}$$

This gives that the fraction of events with more than one photoelectron is smaller than 0.7%. Therefore the probability of having two photoelectrons hitting adjacent pixels is negligible. Practically all the double pixel clusters in these runs must originate from charge sharing and their fraction is a direct measurement of the effect.

Let us indicate with P(v|e) and P(h|e) the probabilities of recording a vertical double cluster or a horizontal double cluster given a single photoelectron hit. The calculation from the cluster counts summarized in Table 3.4 gives P(v|e)$\simeq$ 6.9% and P(h|e)$\simeq$ 0.7% for HPD 0 and P(v|e)$\simeq$ 12% and P(h|e)$\simeq$ 2% for HPD 1. Ratios of counts are in good agreement between different runs.

3.3.2 Measured Cherenkov angles

An algorithm to fit circles to the hits on an event by event basis has been used to correct for the absence of tracking information for the N_2 runs. The distribution of the photon hits on the anode plane is not expected to be exactly circular.

Given an event and its list of hits on the anode plane, the algorithm fits a circle to the hits. This is repeated for all the events with at least 3 clusters. The fitted circle is the one that minimizes the quadratic sum of the distances of the hits from the circumference. A least square iterative minimization procedure is applied [3], with the error function expressed by:

$$E = \sum_{i=1}^{N} \frac{\sqrt{(x_i-x_c)^2+(y_i-y_c)^2}-r_c)^2}{\sigma_i^2} \tag{3.2}$$

$$\sigma_i^2 = \frac{(x_i-x_c)^2}{(x_i-x_c)^2+(y_i-y_c)^2}\frac{\Delta_x^2}{12} + \frac{(y_i-y_c)^2}{(x_i-x_c)^2+(y_i-y_c)^2}\frac{\Delta_y^2}{12} \tag{3.3}$$

where the sum is over the hits in the event, with coordinates (x_i, y_i). The 3 free parameters to determine are the radius (r_c) and the coordinates (x_c, y_c) of the centre of the circle. The σ_i at the denominator takes into account the uncertainty in the hit coordinate due to the pixelization; Eq. (3.3) shows that the dependence of the former on the azimuthal angle ϕ of the hit on the circle, due to the different pixel sizes on the column and row directions (Δ_x, Δ_y), is considered. Initial values are determined from the average centre and radius of the two dimensional histograms of the hits of the full run. Fig. 3.8 displays two events with the circles determined by the fitting, to illustrate the results of the algorithm.

Fig. 3.9 shows the distributions of the radii of the circles fitted to the events. One sigma cuts on the position of the centres of the fitted circles were applied. Pion events constitute the large fraction of events, while the secondary peak shows the presence of electrons in the beam.

The histograms are well fitted with Gaussian distributions. The average values and sigmas of the gaussian fits are listed in the R_a column of Table 3.5. Considering a linear demagnification by a factor 5 and the distance from the mirror given in Section 3.1.1, the radii of the events on the entrance window and the corresponding Cherenkov angles are calculated. Results are summarized also in Table 3.5. The Cherenkov angles measured in this way compare well with the expected ones listed in Table 3.2. The 3% difference between values for HPD 1 can be ascribed to a different radial demagnification function (cf. Section 4.2.1) for this tube.

3.3.3 Photoelectron counting and evaluation of detection efficiency

The radius of the fitted circles allows to discriminate the pion events from the electron events. Counting the number of pixel hits in these events and comparing it to the expected number of photoelectrons would give the detection efficiency. Because of charge-sharing a clustering algorithm is first to be applied to the data in order not to overestimate the number of photoelectrons,

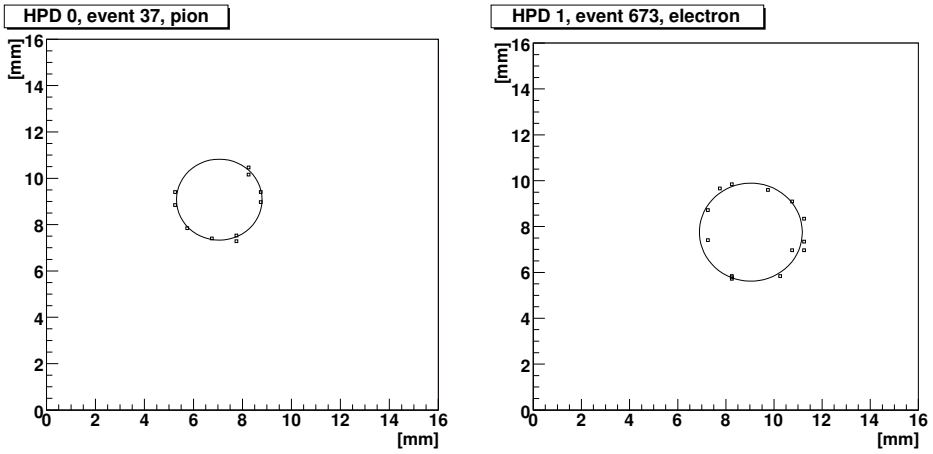

Figure 3.8: A pion event in HPD 0 and an electron event in HPD 1 with the fitted circles.

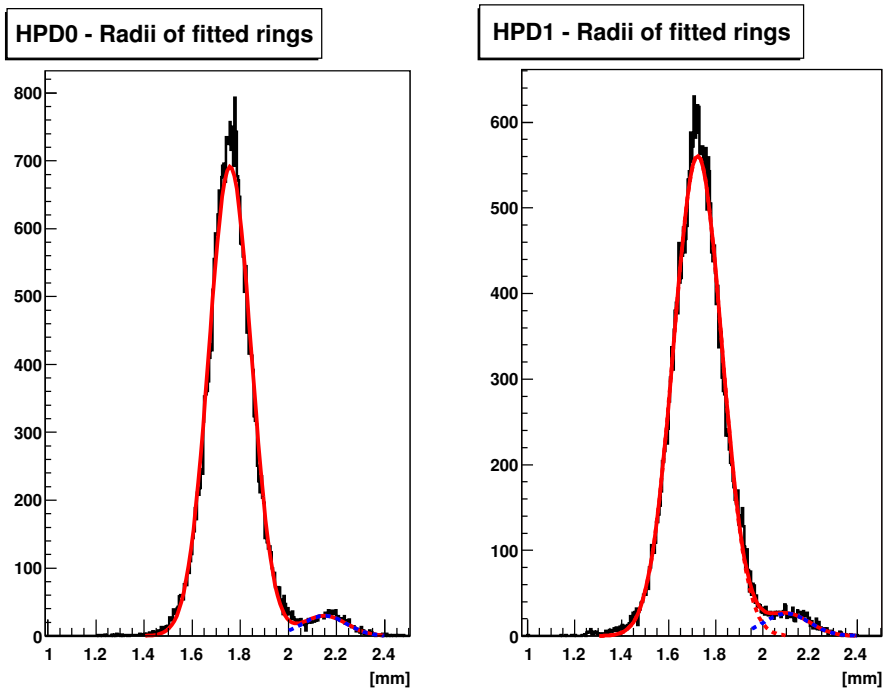

Figure 3.9: Distributions of the radii of the circles fitted to N_2 data runs. Double gaussian fits are overlapped to the histograms. The secondary peaks are due to electrons in the beam.

HPD	Particle	R_a [mm]	R_w [mm]	Θ_c [mrad]
0	π	1.78±0.08	8.9±0.4	19.2±0.8
0	e	2.21±0.08	11.05±0.4	23.8±0.8
1	π	1.74±0.09	8.7±0.45	18.8±0.8
1	e	2.15±0.09	10.75±0.45	23.2±0.8

Table 3.5: R_a: averages and sigmas of the Gaussian fits to the distributions of the fitted circles radii, on anode plane. R_w: corresponding values at the entrance window ($5\times R_a$). θ_c: corresponding Cherenkov angle.

i.e. one should count clusters as a single photoelectron hit. On the other side, two effects in N_2 data would cause an underestimation of the number of photoelectrons, due to the high occupancy of this case: a double-cluster can indeed originate from two photoelectrons hitting adjacent pixels and two photoelectrons can hit the same pixel, giving only one hit. For the former reason, a different approach than clustering has been chosen to determine the detection efficiency.

A numerical simulation allows to determine the distribution of the number of pixel hits per event, assuming a certain detection efficiency. The photoelectrons hits onto the pixelized anode are simulated. The number of photoelectrons is Poisson distributed, with the averages given in Table 3.2. They are distributed uniformly along a circle, whose position and radius are stochastic Gaussians variable with the averages and sigmas measured on the data. The charge-sharing effect was determined in Section 3.3.1 and is included in the simulation as a probability to get a hit in a pixel adjacent to the one on which the photoelectron impacts, once this is detected. In this way the pixelization, the occupancy and the charge-sharing effect are considered.

The detection efficiency is a parameter of the simulation and the entire distribution of the number of hits depends on its value. The determination of the detection efficiency is done by finding the value that reproduces in the simulation the distribution of pixel hits of the data.

Fig. 3.10 shows the distribution of hits in the data runs for the two HPDs and the best fits obtained with the simulation. The corresponding values of detection efficiencies are listed in Table 3.6. They are in agreement with the measurements in a dedicated setup [4], realized with the method of the *back pulse*, once the proper threshold values and high voltage are taken into account.

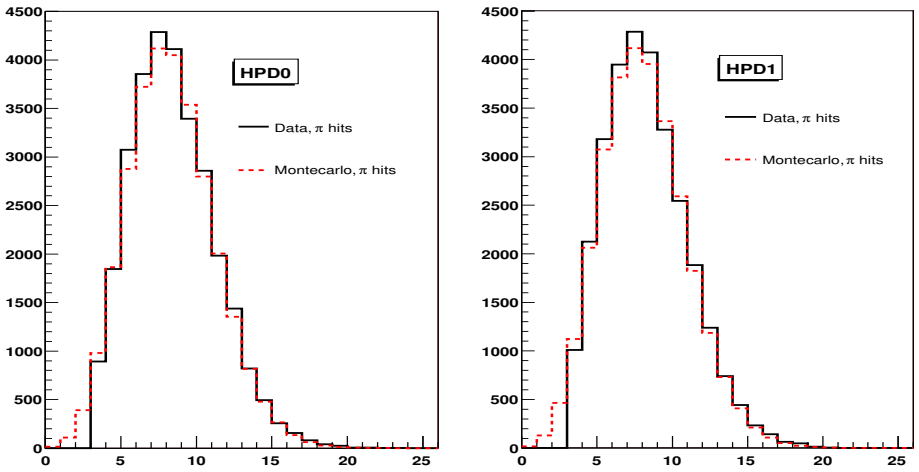

Figure 3.10: The distributions of the number of hits for pion events in the data. Events with less than 4 hits were not included in data. The distributions obtained with the simulation are overlaid.

HPD	Detection efficiency
0	0.80 ± 0.03
1	0.84 ± 0.04

Table 3.6: Detection efficiencies giving the best reproduction of the distribution of hits in data (π events) in the simulation.

Bibliography

[1] A. Braem, *et al.*, "Metal multi-dielectric mirror coatings for Cherenkov detectors", *Proceedings of RICH 2004, Nucl. Instr. and Meth. A*, 2005.

[2] K. Wyllie, *Pixel HPD Test System Hardware Description Version 1.0*, 2004. [Online]. Available: http://kwyllie.home.cern.ch/kwyllie/LHCBPIX1_doc/Test_hardware_doc_1.0.pdf

[3] D. Umbach and K. N. Jones, "A few methods for fitting circles to data", *IEEE Trans. Instrum. Meas.*, vol. 52, no. 6, pp. 1881–1885, December 2003.

[4] M. Moritz, *et al.*, "Performance study of new pixel hybrid photon detector prototypes for the LHCb RICH counters", *IEEE Trans. Nucl. Sci.*, vol. 51, no. 3, pp. 1060–1066, June 2004.

Chapter 4

The effects of magnetic flux density on the LHCb Pixel Hybrid Photon Detector. Characterization and correction

The electrostatic focusing system of the LHCb Pixel HPD is sensitive to an external magnetic flux density, as mentioned in Section 2.3.3. The magnetic effects may deteriorate the spatial resolution of the HPD or even cause loss of coverage if the photoelectrons can not reach the sensitive anode. Similar effects are observed, for example, in Image Intensifiers [1, 2].

The accurate reconstruction of the photon impact position is an essential requirement (see Section 1.3) for the LHCb RICH detectors. Both RICH 1 and RICH 2 are located in the fringe field of the spectrometer magnet (Fig. 1.1 on page 2). The peak magnetic flux density inside the magnetic shielding boxes containing the photon detectors is less than 2.5 mT in RICH 1 and less than 1.0 mT in RICH 2 (cf. Section 1.3). The HPD must operate in this residual field.

This chapters describes the results of a detailed experimental characterization of the distortion induced on the LHCb Pixel HPD by a static external magnetic flux density. The sensitivity of the device to various orientations and amplitude of the field was evaluated. A local magnetic shielding was tested as an effective counter measure to reduce the amount of distortions, thus broadening the range of applications of the novel device.

A model of the effects can be used to correct the distortions of the image in the case of axial magnetic flux density. Even in presence of significant distortion, the reconstruction of the photon hit position from the pixel hit position is possible once the field is known (Section 4.4). A method developed

and tested to estimate the magnitude of the axial magnetic flux density is finally proposed (Section 4.5).

4.1 Magnetic effects and experimental characterization

4.1.1 Description of the induced distortions

The photoelectron trajectories are governed by the Lorentz force due to the electrostatic field ($\mathbf{E}$) generated by the electron optics and any applied magnetic flux density ($\mathbf{B}$):

$$\mathbf{F} = -e\,(\mathbf{E} + \mathbf{v} \times \mathbf{B})\,. \tag{4.1}$$

Fig. 4.1 shows the trajectories with no magnetic flux density applied. An undistorted ($\mathbf{B}$=$\mathbf{0}$) and a distorted photoelectron trajectories are sketched in Fig. 4.2. The case with a magnetic flux density parallel to the HPD axis ($\mathbf{B}_{\parallel}$) is characterized by cylindrical symmetry, given that also the electric field of the electronic lens is cylindrically symmetric. The Lorentz force is normal to $\mathbf{B}_{\parallel}$, making the electrons rotate around the tube axis in spiral trajectories while being accelerated toward the anode. This induces a distortion of the image of the cathode, called S-distortion, as shown in Fig. 4.4. The rotational symmetry is evident.

Referring to Fig. 4.2, let C_k be the centre of the cathode, O the centre of the cathode image on the anode plane, Q the photoelectron emission point and P the impact point of the photoelectrons on the anode plane with no magnetic flux density applied. Assume P' as the impact point of the photoelectron emitted in Q when $\mathbf{B}_{\parallel}$ is applied; then let define r=$\|C_kQ\|$ and r'=$\|OP'\|$. Vectors OP and OP' form an angle $\Delta\varphi$. In the ideally rotationally symmetric case, r' and $\Delta\varphi$ are expected to depend only on the cathode radial coordinate r. These dependencies will be described by a radial mapping function and a rotation function.

A magnetic flux density $\mathbf{B}_{\perp}$ perpendicular to the tube axis, causes a lateral shift of the electronic image. The amount of shift depends on the photoelectron emission point because of the electrostatic field geometry, as shown in Fig. 4.9.

4.1.2 Setup and methods

The experimental setup, shown in Fig. 4.3, allowed to project a collimated beam of light on a predefined set of positions on the HPD's entrance window. The HPD was placed in the magnetic flux density generated by a Helmholtz coil. All the elements of the setup — HPD, a light emitting diode (LED),

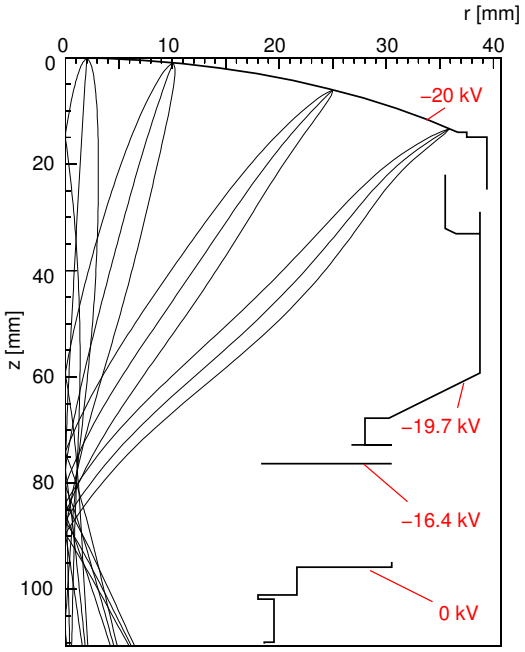

Figure 4.1: Photoelectron trajectories r=r(z) in the LHCb Pixel HPD calculated with no magnetic flux density applied (**B**=**0** T). The results corresponding to four different emission points at increasing radial distances on the cathode are shown. For each of the emission points three different initial velocities were considered for the photoelectron.

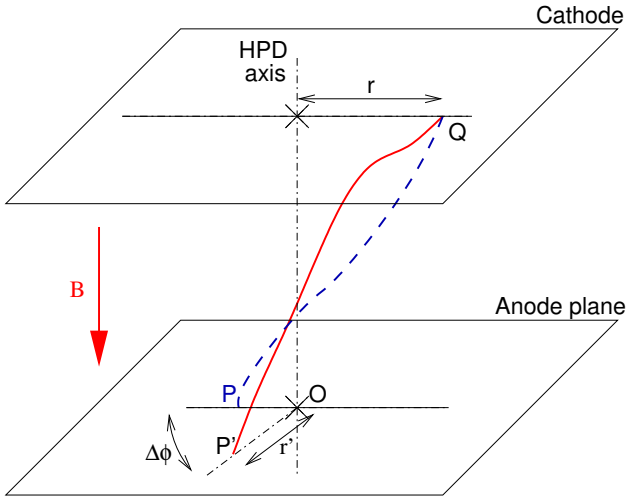

Figure 4.2: A schematic drawing of two photoelectron trajectories with (dashed line) and without (continuous line) an external $\mathbf{B}_{\parallel}$ field applied. Emission point Q and impact points P, P' are shown, as well as the rotation angle $\Delta\phi$.

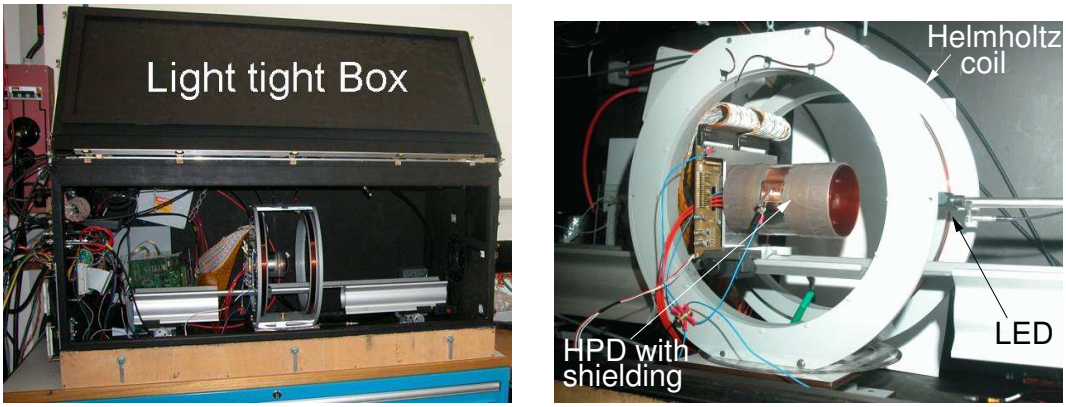

Figure 4.3: Pictures of the setup used for the measurements of distortions induced by magnetic flux density. In evidence: the light tight box, the LED mounted on the x-y table and the Helmholtz coil.

front-end electronics, x-y translation table, coils — were contained in a light-tight box. The subsystems of the setup were interfaced to a computer and controlled via automation software, developed on a commercial platform[1].

The light source was a collimated LED (λ=600 nm) and was supported on the x-y motorized translation table. The light beam was parallel to the tube axis and projected onto the entrance window from a distance of $\sim$7 cm, with a spot size of $\sim$1 mm. By moving the translation table it was possible to define the photon hit position on the HPD window. The setup was also equipped with a system to project a programmable light pattern using a digital projector.

A magnetic shield could be installed around the HPD tube. It consisted of a cylindrical envelope made of Mumetal® of 86 mm diameter, 0.9 mm thickness and 140 mm length[2]. Measurements were done with and without the magnetic shield. The results in the two cases and the effect of the shield will be discussed.

The Helmholtz coil generated a magnetic flux density distribution, uniform on a volume larger than the HPD. Magnetic flux densities up to 5.0 mT could be generated with the coils and they could be rotated at various angles with respect to the HPD geometrical axis.

The HPD perturbed the magnetic flux density map, due to the material of its electrodes (cf. Section 2.3.3) and to the magnetic shielding cylinder surrounding the device. Consequently, the magnetic flux density distribution was

[1] National Instrument LabView^{TM}

[2] Mumetal® is a ferromagnetic alloy of 77% Ni, 14% Fe, 5% Cu and 4% Mo. It has high magnetic permeability, high saturation flux, good malleability. It is widely used for magnetic shielding.

not uniform when the device was in place between the coils. The magnitude of magnetic flux density mentioned in this chapter is to be taken as the value of the field measured in the centre of the coils in absence of the HPD tube and its shield.

Three geometrical configurations were studied. The magnetic flux density was not uniform in any of the configurations described. The symbols among parentheses will be used to refer to the magnetic flux density for each of the cases.

- *Axial orientation*, with an angle of 0° between the HPD geometrical axis and the coil axis ($\mathbf{B}_{\parallel}$) .
- *Transverse orientation*, with an angle of 90° between the HPD axis and the coil axis ($\mathbf{B}_{\perp}$).
- *Oblique orientation*, with an angle of 45° between the HPD axis and the coil axis ($\mathbf{B}_{\angle}$).

The notations $B_{\parallel}$, $B_{\perp}$ and $B_{\angle}$ will be used to indicate the modules of the magnetic flux density.

During a data taking run a magnetic flux density $\mathbf{B}$ of known magnitude was applied to the HPD using the Helmholtz coil. The control and data acquisition system was capable of driving the x-y table holding the LED source across 160 positions on a double-cross pattern. With the light source at a given predefined position, a readout sequence was started, recording up to 20000 events. The LED intensity was regulated such to observe on average ∼0.5 photoelectron hits per event.

The accumulation of the pixel hits of all the 20000 events resulted in a cluster of pixel hits on the anode. The weighted centre of the cluster was calculated as the measure of the mean position of the photon hits corresponding to the predefined position of the LED. The RMS spread of the cluster was assumed as the measure of the corresponding error[3]. The centres and the RMS spreads of the clusters of hits recorded for each predefined position of the LED constituted the data used to characterize the magnetic distortions.

4.2 Measurements and results

4.2.1 Axial magnetic flux density

The effect of $\mathbf{B}_{\parallel}$ in the axial orientation is shown in Fig. 4.4. The centres of the 160 clusters of hits recorded on the anode are plotted in Fig. 4.5 and Fig. 4.6

[3]Data taking was done using the HPD chip in the high resolution ALICE mode, see Section 2.3.5.

for a tube without magnetic shield or with shield respectively. In both cases data for two different values of $B_{\parallel}$ are overlaid on the undistorted (B=0 T) data set.

The hit radial coordinate r' and angular rotation $\Delta\varphi$ can be extracted from data. Following the discussion of Section 4.1.1, the measured radial mapping functions are plotted in Fig. 4.7 for the unshielded and shielded case. The data points are describable by a simple polynomial relation:

$$r' = a_1(B_{\parallel})r + a_2(B_{\parallel})r^2. \tag{4.2}$$

Fitting of Eq. (4.2) to data determines the coefficients a_1 and a_2, given in Table 4.1 as functions of $B_{\parallel}$. The deviation from the linear behavior due to the quadratic term, evaluated at r=35 mm is ∼11% in the unshielded case, while it increases to ∼27% in the shielded case.

The reduction of radial distortion due to the local shielding is evident comparing the dependence of the coefficients from $B_{\parallel}$. The linear coefficient a_1 is similar in the unshielded case with $B_{\parallel}$=1.5 mT and in the shielded case with $B_{\parallel}$=5.0 mT, i.e. with a magnetic flux density more than three times larger than the former case. Moreover for hit points farther from the cathode centre, the radial dilatation is reduced by the local shield. This is reflected into the increase of $|a_2|/a_1$ ratio. The overall dilatation factor of the cathode image is ∼1.3 at 1.5 mT in the unshielded HPD, while it is ∼1.15 at 5.0 mT in the shielded case.

Fig. 4.5 shows that for $B_{\parallel}$>1.0 mT the cathode image will start to extend out of the sensitive anode of an unshielded HPD, because of the dilatation. This constitutes a non recoverable signal loss. On the other hand the image is fully contained on the pixel anode of the shielded HPD, even at the highest magnetic flux density tested ($B_{\parallel}$=5.0 mT). The effectiveness of the Mumetal shielding in preventing coverage loss is evident.

The measured dependence on r of the rotation angle $\Delta\varphi$ around the geometrical tube axis due to the applied $B_{\parallel}$ is shown in Fig. 4.8 (see Section 4.1.1). The rotation angles are larger close to the optical axis than they are at the edges[4]. This is related to the spherical shape of the cathode: the photoelectrons emitted at larger radii have a smaller axial velocity (given the cross-focusing geometry), that implies a smaller force in the plane perpendicular to the axis.

Also in the case of the rotation function a polynomial fit to the data works

[4]The larger spread in data points at low radial coordinates is due to the uncertainties of the measurements of the coordinates of O, P and P'. The uncertainty of the extremities of the vectors, limited by the pixel resolution, affects the calculation of the angle $\Delta\varphi = \angle POP'$. The uncertainty on this angle goes to 2π in the limit of r going to 0.

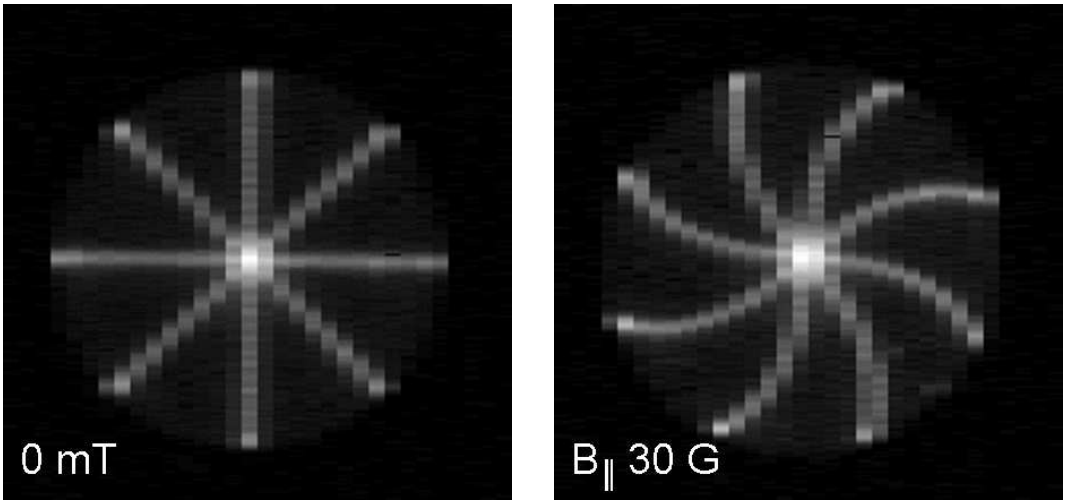

Figure 4.4: The double cross reference pattern recorded by the shielded HPD with no magnetic flux density applied (left) and with an axial magnetic flux density of 3.0 mT (right).

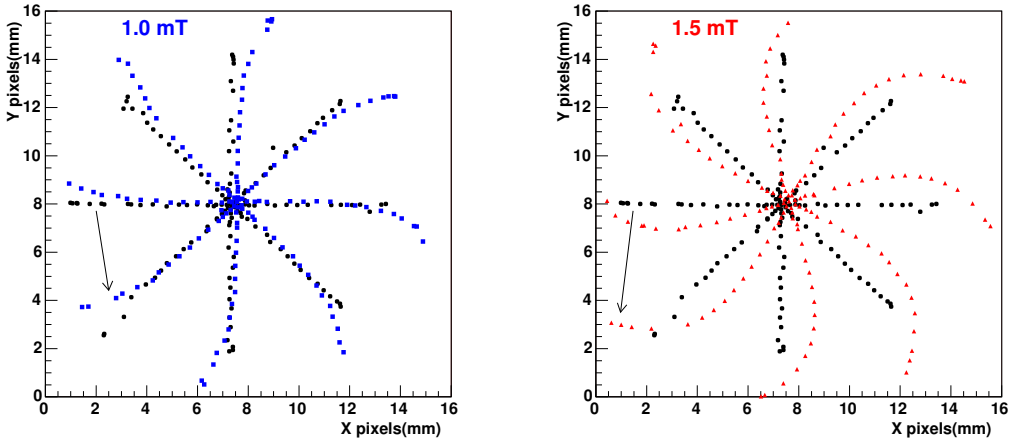

Figure 4.5: Image distortions in the unshielded HPD. The double cross pattern recorded with $B_{\parallel}$=1.0 mT (left, square marks) and $B_{\parallel}$=1.5 mT (right, triangular marks). Data are overlaid to the undistorted reference pattern (B=0.0 mT, dots).

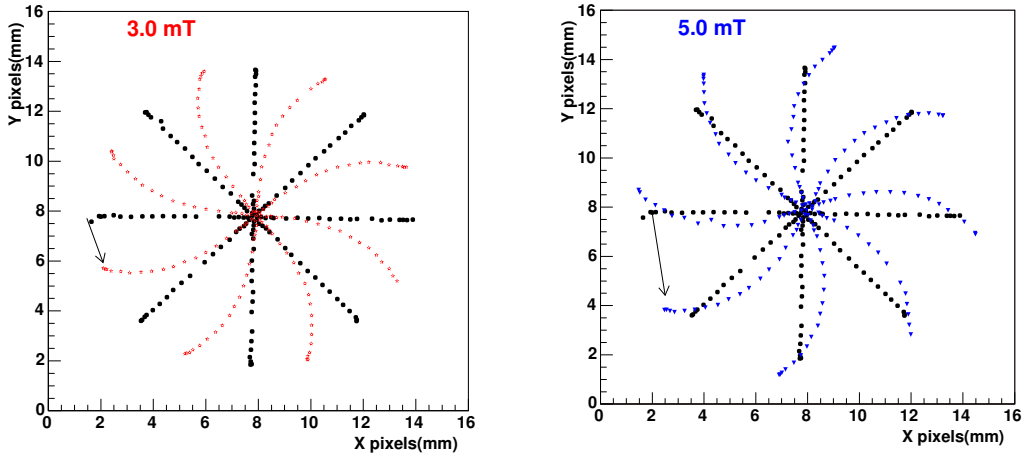

Figure 4.6: Image distortions in the shielded HPD. The double cross pattern recorded with $B_{\parallel}$=3.0 mT (left, square marks) and $B_{\parallel}$=5.0 mT (right, triangular marks). Data are overlaid to the undistorted reference pattern (B=0.0 mT, dots).

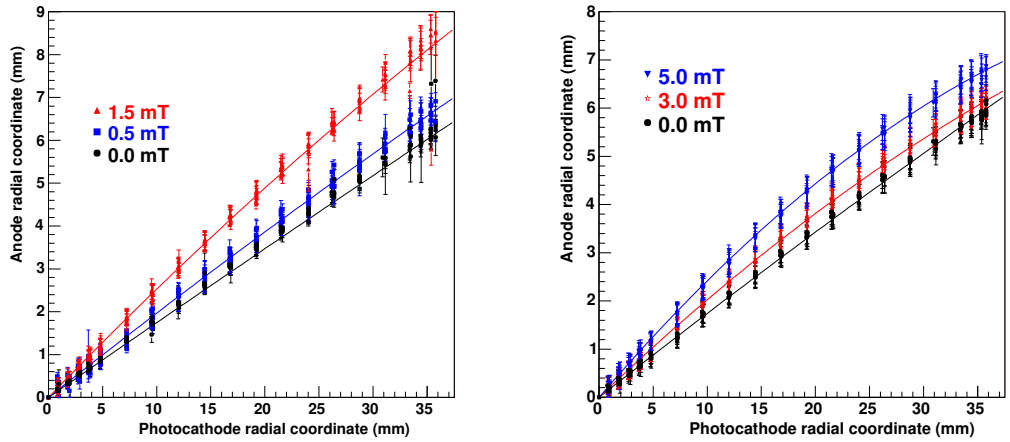

Figure 4.7: Radial mapping functions for an unshielded (left) and a shielded (right) HPD tube, for various values of $B_{\parallel}$.

Unshielded HPD		
$B_{\parallel}$ [mT]	a_1	a_2 [1/mm]
0.0	0.176 ± 0.001	(-1.0 ± 0.3)10^{-4}
0.25	0.192 ± 0.003	(-3.7 ± 0.9)10^{-4}
0.5	0.200 ± 0.002	(-3.6 ± 0.9)10^{-4}
0.75	0.212 ± 0.002	(-3.5 ± 0.9)10^{-4}
1.0	0.238 ± 0.002	(-7.6 ± 0.7) 10^{-4}
1.5	0.261 ± 0.003	(-8.5 ± 1.0)10^{-4}

Shielded HPD		
$B_{\parallel}$ [mT]	a_1	a_2 [1/mm]
0.0	0.177 ± 0.003	(-3.0 ± 1.0)10^{-4}
1.0	0.189 ± 0.003	(-7.0 ± 1.0)10^{-4}
2.0	0.197 ± 0.004	(-8.0 ± 1.0)10^{-4}
3.0	0.214 ± 0.003	(-12.0 ± 1.0)10^{-4}
4.0	0.232 ±0.004	(-16.0 ± 1.0)10^{-4}
5.0	0.262 ± 0.003	(-20.0 ± 1.0)10^{-4}

Table 4.1: The coefficients a_1 and a_2 of the radial mapping functions (Eq. (4.2)).

well:

$$\Delta\varphi = a_3(B_{\parallel}) + a_4(B_{\parallel})r^2 + a_5(B_{\parallel})r^3. \tag{4.3}$$

The values of the coefficients[5] are given in Table 4.2. As it was observed for the radial dilatation, one has to increase $B_{\parallel}$ up to 5.0 mT with the shielded HPD to get the same amount of image rotation measured in the unshielded HPD with $B_{\parallel}$ of only 1.5 mT. In both cases the rotation is less for the photoelectrons emitted far from the axis, but the shape of the reduction of $\Delta\varphi$ with radial distance r is changed by the shielding.

The maximum displacements of the spots between the reference pattern and the distorted pattern were measured on the anode chip. They are listed in Table 4.3. The points with the maximum displacement are approximately halfway between the centre and the edge of the tube.

4.2.2 Transverse and oblique magnetic flux density

The non-uniform translation of the image in a direction normal to the transverse magnetic flux density is shown in Fig. 4.9. The comparison between the unshielded and the shielded case is shown in Fig. 4.10, in which the centres of the spots are overlaid to the reference positions measured with B=0.0 mT. In

[5] The first order coefficient in Eq. 4.3 was dropped to account for $\delta\varphi/\delta r = 0|_{r\to 0}$, i.e. constant rotation at low radii, as it can be deducted from the equation of motion.

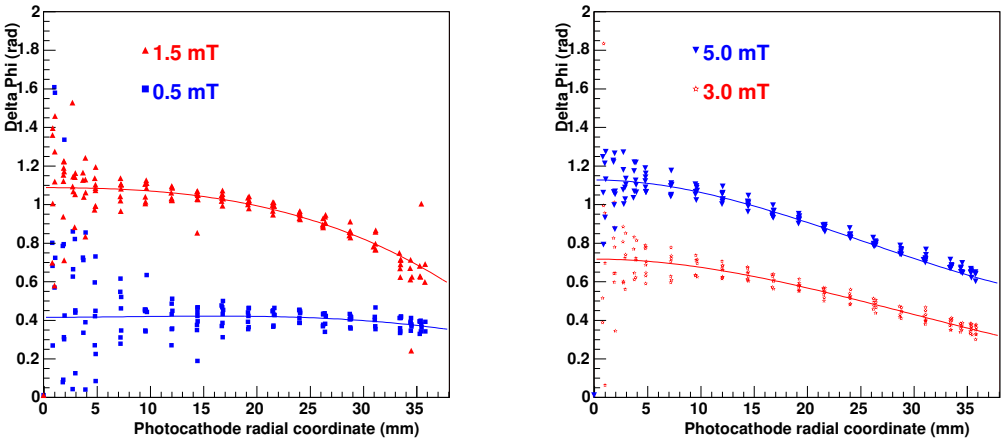

Figure 4.8: The rotation angle $\Delta\varphi$ vs. the photoelectron emission point radial coordinate r (rotation function), in the unshielded (left) and shielded HPD (right).

these figures the direction of the coil axis corresponds to the horizontal axis. The shift is larger in the central area of the pattern, while it reduces toward the left and right edges. This is also related to the reduction of the axial (z) component of the photoelectron velocity at the spherical cathode edge. The asymmetry between the upper and lower arms and the left and right ones can be explained considering the radial components of the velocity.

Previous studies [3] based on numerical simulations had shown that a transverse magnetic flux density as low as a few tenths of mT would sweep the cathode image out of the anode, causing loss of coverage. Magnetic flux densities well above 1.0 mT were applied during these measurements and the photoelectron were always contained inside the anode pixel sensor area. The reason of this difference is the magnetic self shielding effect of the HPD Kovar electrodes.

The displacements of the spots were measured and the maximum displacements in the patterns are listed in Table 4.4. The points undergoing the largest displacements are those close to the centre of the image. There are still symmetries in the transverse field case, but the parameterization is not as straightforward as in the case of axial orientation.

The Helmholtz coil was aligned with its axis at 45° with respect to the HPD axis to study the *oblique* configuration. Data are plotted in Fig. 4.11. In the unshielded HPD case the distortion consists, as expected, of a translation and a rotation of the undistorted image. The translation is the evidence of the effect of the transverse component of the applied $\mathbf{B}_{\angle}$ magnetic flux density. On the other side the shielded case shows rotational symmetry and is very similar to the axial orientation case. The displacement of the central point is

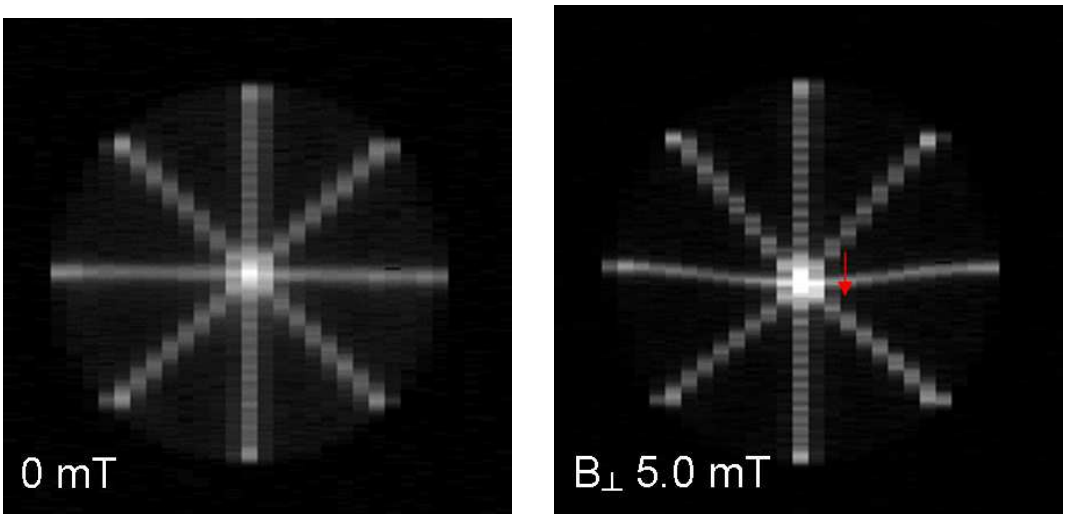

Figure 4.9: The double cross reference pattern recorded by the shielded HPD with no magnetic flux density applied (left) and with $B_{\perp}$=3.0 mT transverse field (right).

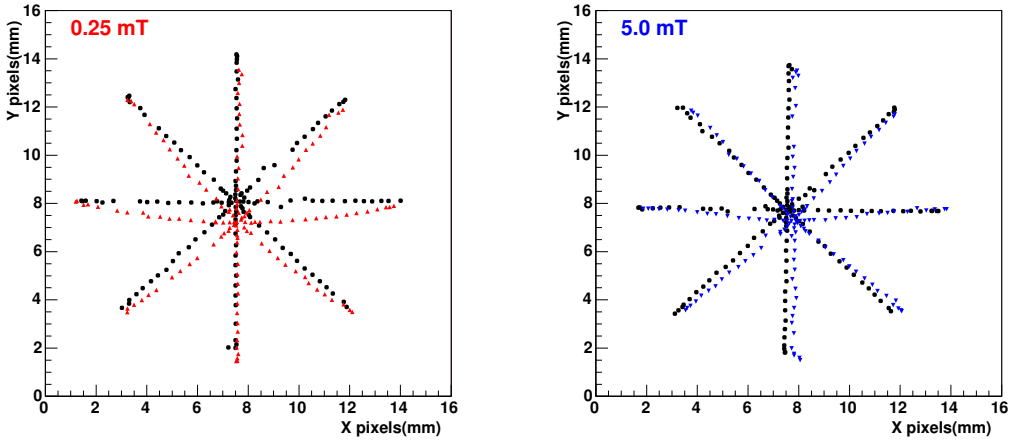

Figure 4.10: Image distortions in the HPD due to transverse magnetic flux density. The distorted (red triangles) double cross patterns are overlaid to the undistorted ($B_{\perp}$=0.0 mT, black circles) reference patterns. Left: unshielded HPD, $B_{\perp}$=0.25 mT. Right: shielded HPD, $B_{\perp}$=5.0 mT.

Unshielded HPD			
$B_{\parallel}$ [mT]	a_3 [rad]	a_4 [rad/mm^2]	a_5 [rad/mm^3]
0.25	0.22 ± 0.05	(0.1 ± 2.0)10^{-4}	(-1.0±6.0)10^{-6}
0.50	0.42 ± 0.04	(0.7 ± 2.0)10^{-4}	(-3.0±5.0)10^{-6}
0.75	0.60 ± 0.04	(0.8 ± 2.0)10^{-4}	(-4.0±4.0)10^{-6}
1.00	0.76 ± 0.03	(1.0 ± 2.0)10^{-4}	(-7.0±4.0)10^{-6}
1.50	1.09 ± 0.03	(-1.0± 1.0)10^{-4}	(-6.0±4.0)10^{-6}

Shielded HPD			
$B_{\parallel}$ [mT]	a_3 [rad]	a_4 [rad/mm^2]	a_5 [rad/mm^3]
1.0	0.24 ±0.06	(-2.0± 3.0)10^{-4}	0.0
2.0	0.49 ±0.04	(-3.0± 2.0)10^{-4}	(3.0 ± 6.0)10^{-6}
3.0	0.72 ±0.04	(-5.0± 2.0)10^{-4}	(6.0 ± 5.0)10^{-6}
4.0	0.91 ±0.04	(-6.0± 2.0)10^{-4}	(8.0 ± 5.0)10^{-6}
5.0	1.13 ±0.04	(-8.0± 2.0)10^{-4}	(10.0 ± 5.0)10^{-6}

Table 4.2: Coefficients of Eq. 4.3 for different values of $B_{\parallel}$ and unshielded/shielded HPD.

negligible in this case. Therefore data were analyzed as they were taken in the axial configuration, determining the coefficients of the radial mapping function and rotation function (Eq. (4.2) and Eq. (4.3)), listed in Tables 4.5 and 4.6.

4.2.3 Effects of the local magnetic shielding and impact on application

The effects of the Mumetal shield had been previously investigated with a numerical solution of the magnetostatic problem [4]. A cylindrical envelope with the same geometry and of the same material of the one used for the measurements had been considered, with two boundary conditions assumed in turn: uniform far field $\mathbf{B}_{\parallel}$ of 5.0 mT parallel to the shield axis and uniform far field $\mathbf{B}_{\perp}$ of 5.0 mT perpendicular to the axis. These differ from the real case for the absence of the field sources at finite distance.

In the axial field case, $B_{\parallel}$ was shown to be reduced below 1.5 mT on the axis, in the region inside the shield where the HPD is located. Not surprisingly, the reduction was bigger in proximity of the cylinder wall ($r \simeq$40 mm), with $B_{\parallel}$<1.0 mT. In the transverse field case, $B_{\perp}$ resulted strongly reduced down to 0.25 mT in the HPD electron optics region. The shielding of the transverse magnetic flux density by the cylinder is obviously more effective with respect to the axial case.

Unshielded HPD		Shielded HPD	
$B_{\parallel}$ [mT]	Δd_{max} [mm]	$B_{\parallel}$ [mT]	Δd_{max} [mm]
0.25	1.6 ± 0.2	1.0	0.9 ± 0.2
0.50	2.6 ± 0.5	2.0	1.6 ± 0.4
0.75	3.7 ± 0.5	3.0	2.3 ± 0.3
1.0	4.7 ± 0.3	4.0	3.3 ± 0.4
1.5	6.4 ± 0.5	5.0	4.3 ± 0.2

Table 4.3: Maximum displacements Δd measured on the anode for various axial magnetic flux densities.

Unshielded HPD		Shielded HPD	
$B_{\perp}$ [mT]	Δd_{max} [mm]	$B_{\perp}$ [mT]	Δd_{max} [mm]
0.25	1.0 ± 0.3		
0.50	1.6 ± 0.2		
0.75	2.2 ± 0.3	3.0	0.4 ± 0.2
1.0	2.8 ± 0.3		
1.5	3.6 ± 0.3	5.0	0.7 ± 0.2

Table 4.4: Maximum displacements Δd measured on the anode for various transverse magnetic flux densities, with the unshielded and the shielded HPD.

The results presented in Section 4.2.1 are in agreement with the reduction of $B_{\parallel}$ below 1.5 mT inside the shield determined in the simulation. Moreover the gradual reduction of $B_{\parallel}$ going from the axis to larger radii and due to the shield, reflects in the different shapes of the radial mapping function and rotation function (Figs. 4.7 and 4.8). The radial compression at larger radii in the shielded case is due to the decrease of $B_{\parallel}$, as well as the smaller rotation angle at intermediate radial distance. The former is essential to avoid loss of coverage.

Table 4.4 confirms that even with $B_{\perp}$ as large as 5.0 mT the maximal displacement measured in the shielded HPD was smaller than the one observed in the unshielded HPD with $B_{\perp}$=0.25 mT.

The recovery of the rotational symmetry (see Fig. 4.11) in the oblique case can be explained with the strong reduction of the transverse component of $\mathbf{B}_{\angle}$ due to the local magnetic shield. The distortions well correspond to the axial field case, as if only the axial component of $\mathbf{B}_{\angle}$ is acting. This is confirmed by the comparison of entries in Tables 4.5 and 4.6 with those of Table 4.1 for which $B_{\parallel}=B_{\angle}/\sqrt{2}$.

In Section 1.3 the expected magnetic field inside the LHCb RICH photon detectors shielding boxes were discussed. The unshielded HPD cannot oper-

Radial mapping function		
$B_{\angle}$ [mT]	a_1	a_2 [1/mm]
0.0	0.182± 0.002	(-4.0 ±1.0)10^{-4}
1.5	0.189± 0.002	(-6.0 ±1.0)10^{-4}
2.8	0.196± 0.003	(-7.0 ±1.0)10^{-4}
4.2	0.218± 0.003	(-10.0 ±1.0)10^{-4}

Table 4.5: Oblique configuration, shielded HPD. Coefficients of the radial mapping function (Eq. 4.2).

Rotation angle			
$B_{\angle}$ [mT]	a_3 [rad]	a_4 [rad/mm^2]	a_5 [rad/mm^3]
1.5	0.29 ± 0.05	(-3.0 ± 2.0)10^{-4}	(5.0 ±7.0)10^{-6}
2.8	0.50 ± 0.04	(-3.0 ± 2.0)10^{-4}	(3.0±6.0)10^{-6}
4.2	0.76 ± 0.04	(-6.0 ± 2.0)10^{-4}	(8.0±5.0)10^{-6}

Table 4.6: Oblique configuration, shielded HPD. Coefficients of the rotation angle function (Eq. 4.3).

ate in RICH 1 magnetic flux density of 2.5 mT without coverage loss. The shielded HPD is expected to be operational with this field level, but given the large displacements (see Table 4.3) of the image on the anode, a correction of the distortion will be needed, to recover the required accuracy in the reconstruction of the photon Cherenkov angle. The HPDs could operate unshielded in the 1.0 mT transverse magnetic flux density inside RICH 2 shielding boxes, but would suffer of significant distortions. Local shielding is expected, from the previous measurements, to reduce the distortions to an undetectable level, if no significant axial component of **B** will be present.

4.3 The parameterization of the distortions

The rotational symmetry and regular behavior of the radial mapping function and the rotation function allow to extend the model presented in Section 4.2.1.

The radial mapping function can be expressed with a second order polynomial:

$$\rho = \rho_1(B_{\parallel})r + \rho_2(B_{\parallel})r^2 \tag{4.4}$$

$$\rho_i(B_{\parallel}) = \sum_{j\leq 3} \rho_{i,j} B_{\parallel}^j \tag{4.5}$$

in which the coefficients are in turn polynomial functions up to third degree of

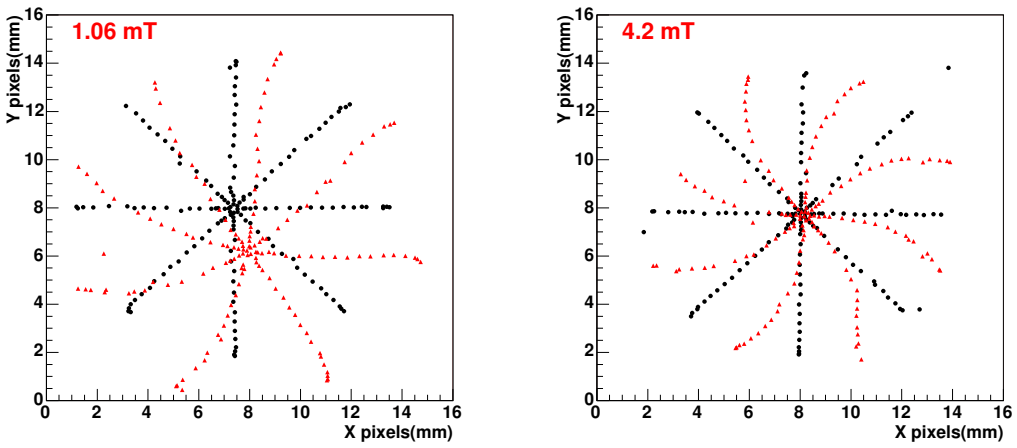

Figure 4.11: Distorted patterns in the 45° oblique orientation, overlaid to the reference pattern (black circles). Left: unshielded HPD with $B_{\angle}$=1.06 mT. Right: shielded HPD with $B_{\angle}$=4.2 mT.

the field value. In a similar fashion the rotation function is parameterized by

$$\Delta\varphi = \Delta\varphi_0(B_{\parallel}) + \Delta\varphi_2(B_{\parallel})r^2 + \Delta\varphi_3(B_{\parallel})r^3 \quad (4.6)$$

$$\Delta\varphi_i(B_{\parallel}) = \sum_{j\leq 3} \Delta\varphi_{i,j} B_{\parallel}^{j}. \quad (4.7)$$

See also footnote on page 87.

Each of the coefficients $\rho_{i,j}$ and $\Delta\varphi_{i,j}$ have been calculated to best fit the full set of experimental data, thus providing a simple but complete parameterization of the radial mapping function and rotation function with respect to the magnetic flux density.

The coefficients are listed in Tables 4.7 and 4.8. This simple model can also be applied in the oblique configuration, in which the effect of the transverse component of **B** is strongly reduced by the local shield.

$\rho_{i,j}$	j			
i	0	1	2	3
1	0.1771	$1.818\cdot10^{-4}$	$2.2197\cdot10^{-5}$	0
2	$-4.713\cdot10^{-4}$	$8.613\cdot10^{-6}$	$-1.2794\cdot10^{-6}$	$1.36\cdot10^{-8}$

Table 4.7: Coefficients of the expression of the radial mapping function, Eq. 4.5, with the radial coordinates expressed in [mm] and $B_{\parallel}$ in $[10^{-1}\text{mT}]=[\text{G}]$

$\Delta\varphi_{i,j}$	j			
i	0	1	2	3
0	0	$2.552{\cdot}10^{-2}$	$-4.790{\cdot}10^{-5}$	0
2	0	$-6.930{\cdot}10^{-6}$	$-8.313{\cdot}10^{-7}$	$1.230{\cdot}10^{-8}$-8
3	0	$3.381{\cdot}10^{-8}$	$1.619{\cdot}10^{-8}$	$-2.248{\cdot}10^{-10}$

Table 4.8: Coefficients of the expression of the rotation function, Eq. 4.7, with the angle expressed in [rad] and $B_{\parallel}$ in $[10^{-1}\text{mT}]$=[G].

4.4 Distortion correction

The photon hit position can be reconstructed from a pixel hit using the previous model even when a $\mathbf{B}_{\parallel}$ field is acting. The rotation function and the radial mapping function can be inverted to reconstruct the hit position on the window from the coordinates of the pixel hit on the anode. It is assumed that $B_{\parallel}$ is known. This constraint will be addressed in Section 4.5.

Fig. 4.12 shows, on the left, the original uncorrected pixel hit data, namely the centers of the spots recorded by the HPD readout when the light source was scanned through the points of the double cross. The coordinates are on the anode plane.

Some of the data points are out of the pattern. They were recorded when the source was located at the extremities of the pattern and light was reflected by the metalization at the edge of the HPD cathode. The reflected light reached the anomalous positions on the cathode originating the clusters of hits out of the pattern.

The right frame of the same figure shows the output of the reconstruction algorithm applied to the case with $B_{\parallel}$=3.0 mT. The reconstructed positions of the LED are shown, overlaid to the known real positions. The coordinates in this figure refer to the x-y translation table coordinates and constitute a reference frame on the plane normal to the HPD axis, tangent to its entrance window, with the origin coinciding with the tube axis.

A quantitative evaluation of the results of the correction algorithm can be expressed by the RMS error in the reconstruction of the 160 positions of the double cross pattern. The RMS errors are listed in Table 4.9. Sixteen data points corresponding to the reflections from the edge were excluded from the computation.

The procedure needs an accurate knowledge of the coordinates of intersection of the axis of rotational symmetry with the anode plane and the window plane, from which all the radial distances and vector angles are evaluated. Uncertainties on these coordinates are a source of reconstruction error, even in the case with B=0 mT.

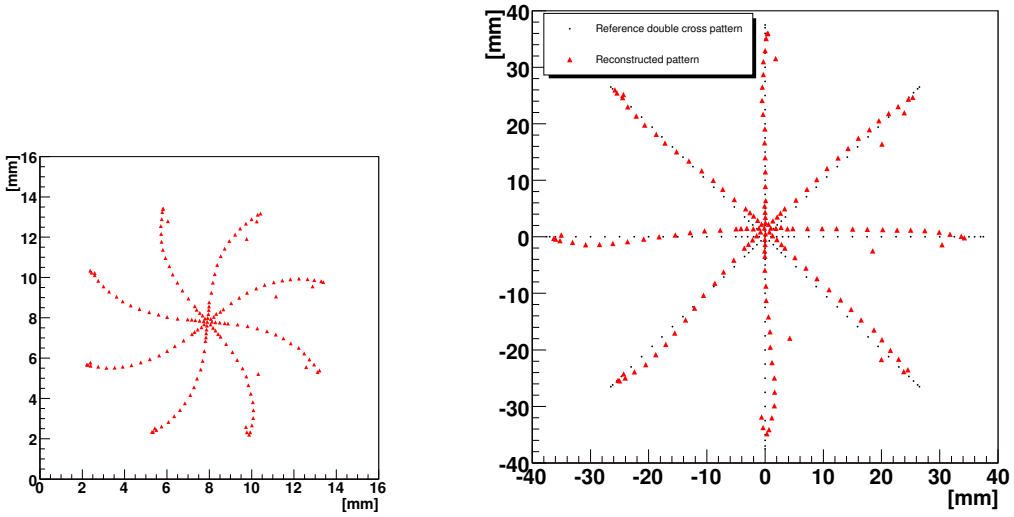

Figure 4.12: Left: the weighted centres of the recorded hits in the pixel detector, double cross pattern, $B_{\parallel}$=3.0 mT. Right: the reconstruction algorithm output. Positions on the entrance window plane, true (black dots) and reconstructed from data (red triangles).

The correction error should be compared to the limited spatial resolution of the HPD due to the pixel size: $\sim 2.5/\sqrt{12} = 0.72$ mm and $\sim 0.312/\sqrt{12} = 0.09$ mm on the column and row directions. For the application in the LHCb RICH only the larger resolution has to be considered.

$B_{\parallel}$ [mT]	RMS reconstruction error [mm]
0.0	0.40
1.0	0.75
2.0	0.88
3.0	1.33
4.0	1.65

Table 4.9: Root mean square reconstruction error on the points of the double cross pattern, for different values of $B_{\parallel}$.

4.5 Magnetic flux density estimation

The correction procedure described in the previous section relies on the a priori knowledge of the axial magnetic flux density generated by the coils. The parameterization of the distortions given in Eq. (4.6) allows, despite its

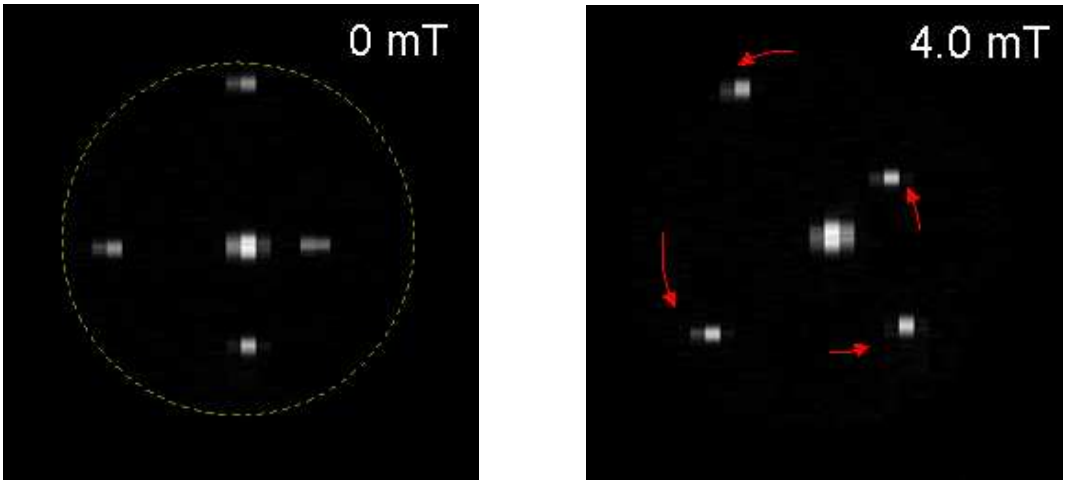

Figure 4.13: The estimation pattern. Left: B=0.0 mT. Right: $B_{\parallel}$=4.0 mT.

simplicity, the estimation of the applied field from experimental data. The algorithm of the estimator is based on the measurement of the amount of S-distortion on a simple test pattern. The data read out when no field is applied and when the unknown $B_{\parallel}$ axial flux is present are compared.

The test pattern used for the proof of principle had five spots of light, with the central one larger in size than the remaining four, located at increasing radial distances from the former.

Left frame of Fig. 4.13 shows the image read out from the HPD while the test pattern is being projected onto the window and without magnetic flux density applied (B=0 mT). The frame on the right shows the effects of the application of a $B_{\parallel}$=4.0 mT magnetic flux density. The static light pattern used in the test was realized with the digital projector connected to a computer and attenuated with absorptive filters.

The estimating algorithm extracts informations on the pattern of the image: after thresholding and clustering, the centres of the clusters of hits are computed by the intensity weighted average. The procedure is applied to the undistorted image and to the distorted one, producing two lists of spot coordinates. The data points from the two frames are ordered by the increasing distance from the central spot, which is easily identified in both cases by its larger size. The correspondence problem is then solved by the algorithm using the hierarchy in the radial distance. The obtained four point sampling of the rotation angle as a function of radius is then used together with Eq. (4.6); $B_{\parallel}$ is now considered as a free parameter. The applied $B_{\parallel}$ is determined as the one giving the least square best fit of the measured points.

The results of the application of this algorithm to test runs with various axial magnetic flux densities are reported in Table 4.10. In most of the cases

the estimator committed an error smaller than 0.1 mT. The 3.0 mT data set constitutes an anomaly, the reason of which was not understood.

Applied $B_{\parallel}$ [mT]	Estimated $B_{\parallel}$ [mT]	Error [mT]
1.0	0.90±0.20	-0.1
2.0	2.05±0.27	0.05
3.0	3.24±0.27	0.24
4.0	4.08±0.24	0.08
5.0	5.07±0.19	0.07

Table 4.10: The errors of the estimator of the axial magnetic flux density.

4.6 A system for the correction of image distortions in the LHCb RICHes

The need for a correction of the distortions in RICH 1 was discussed in Section 4.2.3. The possibility of the correction of the distortion, once the field is known, has been demonstrated. Accurate numerical computation of the **B** field in the LHCb experiment and measurements on the real system during the test of the LHCb dipole magnet indicate that the magnitude $B_{\parallel}$ of the magnetic flux density will differ between the HPDs located at different locations on the detection plane. Also for RICH 2 the possibility of correcting the residual distortions would be useful.

Given that 484 HPDs will be installed in RICH 1 and RICH 2 an automated procedure to determine the distortions in each tube should be used. A projected test pattern is required to be simple, to allow for automatic image analysis and extraction of quantitative information from the recorded data. Light projection systems properly positioned in the RICHs are under study to allow projection of test patterns on the detector planes. They will allow to apply a calibration procedure similar to the one discussed in the previous section, by acquiring sample data before and after the ramp-up of the LHCb dipole magnet current.

Another viable possibility is to map the distortions at various instants during the ramping up of the magnet current, determining the position of each spot at various values of the field. This would solve the correspondence problem by extracting the closest neighbor from frame to frame. A look-up table should be calculated from the recorded data to map the pixel hit position to photon hit position. Refinement of the look up table could be done offline using data from saturated tracks.

Bibliography

[1] P. Cerveri, *et al.*, "Hierarchical radial basis function networks and local polynomial un-warping for x-ray image intensifier distortion correction: a comparison with global techniques", *Med. Biol. Eng. Comput.*, vol. 41, pp. 151–163, 2003.

[2] E. Gronenschild, "The accuracy and reproducibility of a global method to correct for geometric image distortion in the x-ray imaging chain", *Med. Phys.*, vol. 24, no. 12, December 1997.

[3] T. Gys and D. Piedigrossi, "Performance of electrostatically-focused image intensifier tubes in low magnetic fields", CERN, Tech. Rep. CERN-LHCb-97-026, 1997.

[4] T. Gys, "Hpd magnetic shielding", 1999, private communication. http://tilde-gys.home.cern.ch/~gys/LHCb/PixelHPDs.htm.

Chapter 5

LHCb RICH 2 optical system

5.1 High reflectivity mirrors. Light and accurate opto-mechanical system

The particle identification performance of the RICH detectors relies on a highly reflective and perfectly aligned system of mirrors (Section 1.3.2). The highest number of Cherenkov photons should be collected for the efficient determination of the particle type (Section 1.3.2). The precision of the Cherenkov angle reconstruction goes roughly as $1/\sqrt{N}$, where N is the number of detected photons.

N is smaller than the number of emitted photons mainly because of the photodetector limited quantum efficiency (cf. Chapters 2 and 3). Other losses are due to photon scattering and absorption, either by the radiator itself or by the mirrors, or to the reflections at the optical interfaces. Apart from the special case of silica aerogel, photon losses in the gas radiators can be neglected [1].

The mirrors must be highly reflective, particularly in the wavelength range 200-400 nm, where the quantum efficiency of the photon detectors is at the maximum (see Fig. 5.5).

No degradation of the detector angular resolution should be caused by the mirror geometrical characteristics or residual misalignments. The mirror support system must therefore allow a precise initial alignment and long term mechanical stability. It must be also compatible with the fluorocarbons CF_4 and C_4F_{10} used as Cherenkov radiators.

The total amount of material of the opto-mechanical system is limited by the constraint on the radiation length and interaction length discussed in Section 1.3.3.

The construction and implementation of a light and precise optical system

with a stable and accurate supporting structure has been a technological challenge requiring extensive research and development. The solutions developed to satisfy the stringent requirements on the LHCb RICH 2 optical system are described in the following. The development and construction of the mirrors, the integration, the quality assurance, the final installation and the alignment procedure are discussed.

5.1.1 The mirror geometrical characteristics and the mutual misalignment

The optical properties of the mirrors influence the accuracy of the Cherenkov angle reconstruction [2]. For the LHCb RICH detectors it is required that the error introduced by the optical systems be negligible with respect to the others. Both RICH 1 and RICH 2 have reflective surfaces made up of arrays of adjacent mirror segments. It is useful to distinguish between the intrinsic optical resolution of the mirror segments and the error due to their mutual misalignment.

The nominal value of the radius of curvature R is determined by the geometry of the detector and by the location of the photodetectors out of the acceptance. Let r_c be the radius of the base of the Cherenkov cone on the mirrors and F=R/2 the focal length of a mirror segment. The RMS error in the reconstructed Cherenkov angle due to a variation of F is given by:

$$\sigma_{\theta,F} = \frac{r_c\sqrt{<\Delta F^2>}}{F^2}. \tag{5.1}$$

Thin and large mirrors as the ones of the LHCb RICHes have irregular surfaces even at a macroscopic scale. Their surface can only approximate the ideal spherical shape. The irregular mirror geometry can be described by the angle $\Delta\theta_m$ between the normal to the surface at various points of the mirror and its nominal direction passing by the centre of curvature. Due to the reflection of the photons on the mirror, the RMS error introduced in the reconstruction of the Cherenkov angle is:

$$\sigma_\theta = 2\sigma_m = 2\sqrt{<{\Delta\theta_m}^2>}. \tag{5.2}$$

The corresponding transverse spread of the intensity of the image of an ideal point-like source on the plane at a distance R is:

$$\sigma_s \simeq 2R\sigma_m. \tag{5.3}$$

The intrinsic diffraction limited spot size is much smaller and has been neglected. Assuming an ideal two dimensional Gaussian distribution of light in

the image plane

$$I(x,y) = \frac{I_0}{2\pi\sigma_s^2} e^{-\frac{x^2+y^2}{2\sigma_s^2}}, \tag{5.4}$$

a circle of diameter $D_0 = 2\sqrt{6}\sigma_s$ contains 95 % of the intensity. Therefore the intrinsic optical resolution of the spherical mirrors can be obtained from:

$$\sigma_\theta = 2\sigma_m = \frac{\sigma_s}{R} = \frac{D_0}{2\sqrt{6}R}. \tag{5.5}$$

The mutual misalignment of the mirror elements is another source of reconstruction error. However the offline analysis of data will allow for the correction of the mutual misalignment if it is initially of the order of ∼0.1 mrad [3].

5.1.2 Specifications on the RICH 2 mirrors

Each of the two spherical reflective surfaces of RICH 2 is composed of 28 elements, as shown in Fig. 5.1, for a total of 56 spherical mirrors. There are 36 hexagonal mirrors. Their shape is inscribed in a circle of 502 mm diameter. The remaining elements are half hexagons or special pieces with cuts to leave space for the RICH 2 central tube. The radius of curvature and the spot size were specified to be R = 8600 ± 43 mm and $D_0 < 2$ mm (see Section 5.2.1). The RICH 2 radiator length is ∼2 m. For particles with $\beta = \frac{v}{c} = 1$ in CF_4 it is $\theta_{ch} \simeq 32$ mrad, then $r_c = \theta_{ch} \times 2$ m $\simeq 64$ mm. Eq. (5.1) gives $\sigma_{\theta,F} \simeq 0.075$ mrad assuming a uniform distribution of radii in the specification interval. Eq. (5.5) gives the uncertainty due to the irregularity of the shape $\sigma_{\theta,D_0} \simeq 0.05$ mrad. Both contributions to the reconstruction error are negligible with respect to the other sources listed in Table 1.2 on page 18.

The LHCb RICH 2 design specified the second reflective surfaces to be planar. Each of them is made up of 20 flat mirrors installed in two arrays of 5×4.

5.2 Measurements of the characteristics of the LHCb RICH 2 mirrors

5.2.1 Geometrical parameters and surface quality

All the substrates of RICH 2 mirrors were made of SiMax[1] glass and were produced by a specialized firm[2]. They were ground and polished to the nominal

[1] Clear hard borosilicate glass with high resistance to heat and chemical stability. 80.4% SiO_2, 13.6% B_2O_3, 2.4% Al_2O_3, 4.2% Na_2O+K_2O.

[2] Compass, Czech Republic.

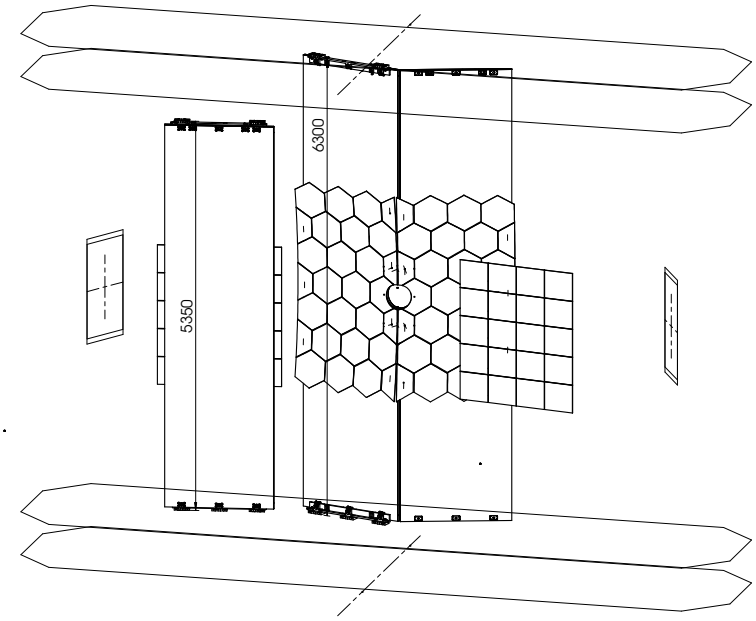

(a)

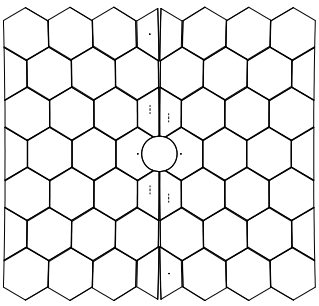

(b)

Figure 5.1: (a) Design drawings of the RICH 2 optical system, view looking to positive z. The spherical and flat arrays of mirrors are in evidence. The right flat mirrors supporting panel is not shown for clarity (cf. Fig. 1.8(b) on page 15). (b) Detail of the spherical mirror arrays.

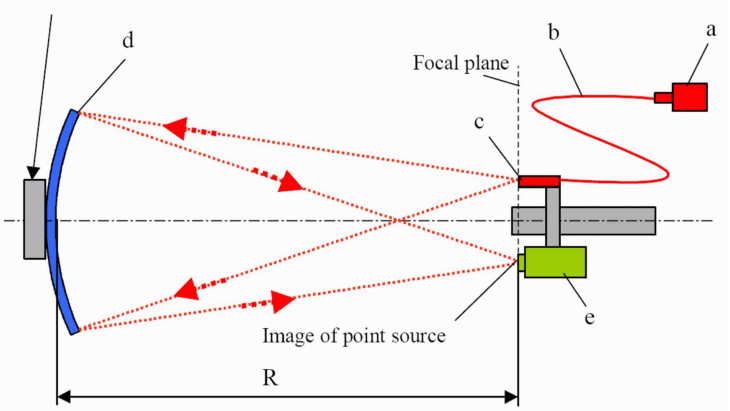

Figure 5.2: The scheme of the setup for the measurement of the radius of curvature and the spot size of the RICH 2 mirrors.

shape and thickness from bulk substrates. Their maximum thickness is 6 mm.

An optical test bench was used for qualifying the substrates as they were delivered to CERN from the manufacturing, prior to coating. The setup is shown schematically in Fig. 5.2. The radius of curvature of each of the mirror substrates and the spot size had to be measured. The method was based on the imaging on a CCD camera of a point-like source after a reflection on the substrate. The light was reflected at the dielectric boundary between air and the glass substrate. The distance between the source and the substrate was varied until a reflected spot of minimum diameter was imaged on the CCD, located on the plane of the light source. Fig. 5.3 shows a typical reflected spot as imaged on the CCD sensor. The irregularity of the spot is due to the non-ideal spherical shape and the hypothesis of Gaussian intensity profile is clearly not satisfied. In spite of that Eq. (5.5) was applied to calculate the intrinsic mirror resolutions from the measurement of a spot size.

The spot size D_0 was operationally defined as the diameter of the smallest circle containing 95% of the light reflected on the sensor. The radius of curvature R was the distance between the source and the mirror for which the spot size D_0 was obtained. The two geometrical parameters were simultaneously measured with an automated procedure. A 16 bit dynamic range CCD had to be used to guarantee the proper accuracy of the image analysis algorithm determining the circumference of minimum diameter [4].

Fig. 5.4 shows the results of the measurements on the spherical substrates. A few of them were out of specifications, but this was not critical because of the negligible impact on the angular resolution. The resulting average and absolute maximum error introduced by the spherical mirrors are 0.063 mrad and 0.12 mrad.

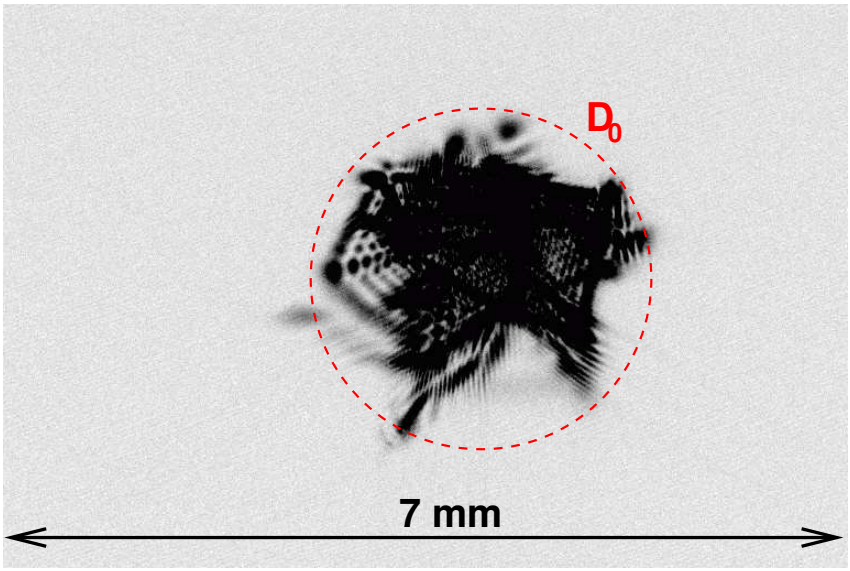

Figure 5.3: The spot of light reflected by the spherical mirrors as imaged on the CCD sensor located at plane of the point-like source. The sensor was 7×4.6 mm^2.

	Min.	Avg.	Max.	RMS dev.
Radius [m]	70.9	79.75	96.1	4.8
Intrinsic resolution [μrad]	23.8	63.6	141.2	29.8

Table 5.1: A summary of the measurements on the 40 mirrors of the flat reflective surfaces. The intrinsic resolution is evaluated by measuring the spot size of a reference spherical mirror after double reflections on the element under test.

Due to manufacturing limitations the 40 rectangular mirrors that make up the two flat surfaces are in fact also spherical. However their radius of curvature is larger than 70 m. This is an acceptable modification of the original design. They will be still referred using the term flat in the following.

The geometrical properties of the segments of the flat mirrors were qualified using a variant of the procedure described. The light source was imaged after multiple reflections: first on the mirror under test, then onto a reference high precision spherical mirror and finally again on the flat mirror. Table 5.1 summarizes the measurements on the 40 mirrors.

The amount of defects on the glass surface, typically originating from bubbles in the substrates, was determined by inspection with a microscope. The substrates were rejected if the defects extended for more than 0.1% of the total surface. The roughness of the polished substrates could not be measured directly. The surface quality could be fully evaluated only after the coating of the substrates.

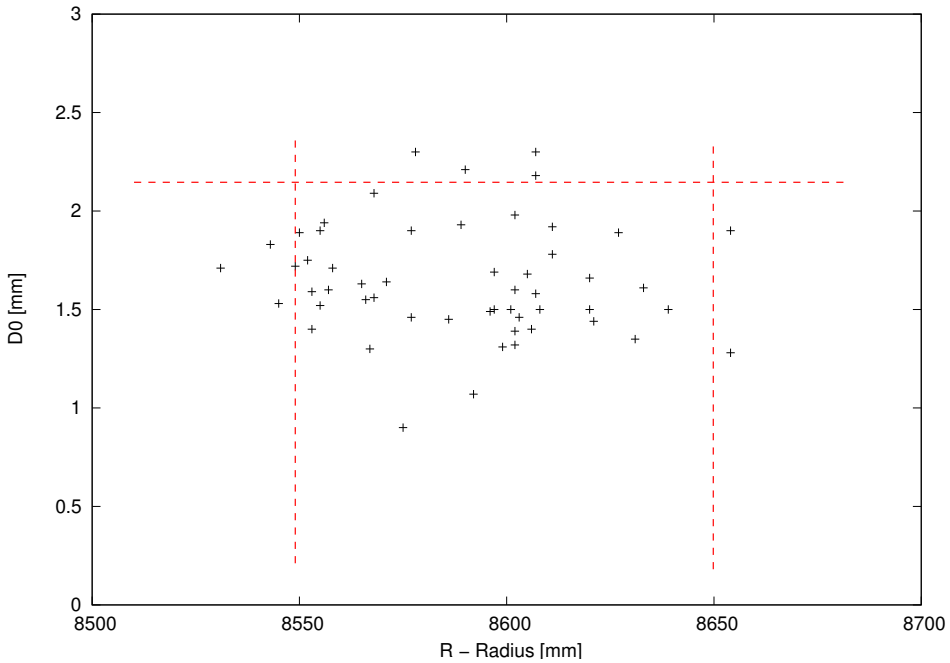

Figure 5.4: Geometrical parameters of the RICH 2 spherical mirrors substrates: scatter plot of spot size D_0 vs radius of curvature R. The lines delimit the region in which the specifications are satisfied.

5.2.2 Reflective coatings

The reflective coatings of the RICH 2 mirrors were realized at CERN [5]. Aluminum is the only viable film material for reflective mirrors that require high reflectivity in the 200-400 nm UV region [6]. Other common coating metals (Au, Ag, Pt, Cu) have strong absorption in this wavelength range. The deposition rate of the high purity Al film in very high vacuum has to be fast (>4 nm/sec) and the substrate kept at room temperature. Under these circumstances the level of impurities and the surface roughness are kept very low and the high reflectivity is obtained. The metal layer has to be coated with a dielectric film to protect it from oxidation in air. This would introduce undesired UV absorption. The dielectric coating also acts as a mechanical protection. Silica SiO_2 strongly adheres on Al. It can be used for UV coatings provided that evaporation in an oxygen enriched atmosphere is used to ensure full oxidation.

The deposition was done in a 1 m diameter vacuum chamber. An 85 nm layer of aluminum was deposited on top of a 20 nm chrome layer. The chrome layer enhances adhesion on the glass substrate. The deposition of Al (5 nm/sec) was by thermal evaporation of 99.999% pure material, heated by a tungsten coil. A double layer dielectric coating was deposited on top of the Al layer.

N_{tr}	45.3
Spherical mirror coverage	96.2%
Flat mirror coverage	97.5%
Quartz plate interface	96%
HPD array coverage	63.7%
N_{pe}	26
N_{hits}	22.6

Table 5.2: Expected average photoelectron yield N_{pe} and number of detected hits N_{hits}. N_{tr} was calculated from Eq. (1.12) integrated in the 200-800 nm range, considering an average track length of 2 m [3, 7], $\beta = 1$, the refractive index of CF_4 (STP) and the average HPD quantum efficiency of Fig. 5.5. The coverages of the mirror surfaces are from [7]. An average loss of 2% was estimated for each reflection at the surfaces of the fused silica plates in front of the photodetector housings (single layer MgF_2 anti-reflective coating centered at 300 nm). The 89.5 mm HPD pitch and 37.5 mm entrance active radius determine the HPD coverage. A detection efficiency of 87% [8] was used to calculate the number of detected hits from the number of photoelectrons.

A 38 nm thick HfO_2 layer on top of a 28 nm SiO_2 layer enhance the reflectivity around the peak sensitivity of the photodetectors (270 nm). The dielectric materials were evaporated by electron beam in oxygen atmosphere ($p(O_2) \sim 10^{-3}$ Pa) at rates of 0.2 nm/sec.

Fig. 5.5 shows the average reflectivity of the coated mirrors. The average HPD quantum efficiency curve is shown as well as the product of the latter with the mirror reflectivities to account for the double reflection. The expected average number of photoelectrons in RICH 2 can be calculated from Eq. (1.12). The results are summarized in Table 5.2. The expected number of detectable hits is in agreement with the design value [7].

The reflectivity of each mirror was also measured shining light (660 nm) on the entire surface of the mirror and measuring the reflected intensity. Data were compared to a reference sample. The distribution of the measured reflectivities of a subset of mirrors is given in Fig. 5.6. The mirrors with a relative reflectivity lower than 95% of the reference were not accepted for installation in RICH 2.

5.3 Mirror supporting system

5.3.1 The mirror holder and the holding panels

The mirror support system has to be very light and mechanically rigid. Moreover the possibility to align the mirror elements is to be guaranteed together

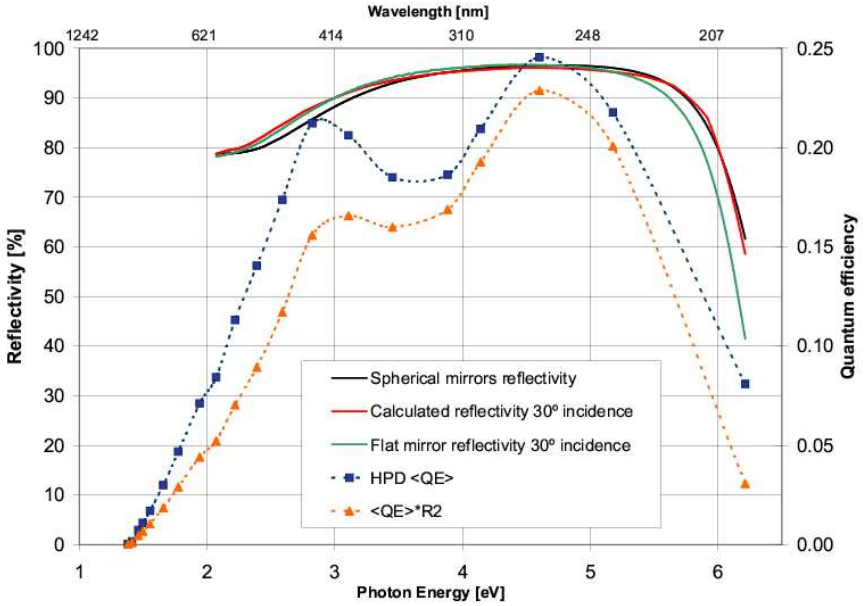

Figure 5.5: RICH 2 mirrors reflectivity and HPD quantum efficiency. The average reflectivity measured on 63 spherical mirrors is plotted (left axis). The curve for the flat mirror was measured on the first coated mirror. The HPD quantum efficiency (right axis) is the average of the measurements on 6 pre-production prototypes. The product with the two measured reflectivities is shown.

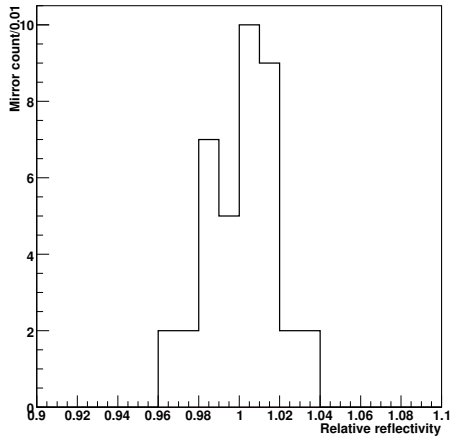

Figure 5.6: Reflectivity of 42 of the RICH 2 spherical mirrors relative to a reference sample.

	Radiation length [% X_0]	
Entrance window	1.0	
Exit window	2.5	
	Spherical mirror panel	Flat mirror panel
Al honeycomb support panel	4.0	3.8
Mirror support (average)	0.5	0.4
Mirror	4.7	4.7
Total	12.7	12.4

Table 5.3: RICH 2 material budget. Fractional radiation lengths of the various elements of RICH 2 traversed by the particles. The corresponding fractional energy losses of high energy electrons for bremsstrahlung are 11.9% and 11.7%.

with long term mechanical stability. Polycarbonate was chosen to manufacture the mirror supports. It satisfies the rigidity and lightness requirements and it is tolerant to fluorocarbon gases.

A polycarbonate ring was glued with epoxy glue on the back of each mirror segment and connected with a three screw regulation system to a mirror holder. The polycarbonate mirror holders were connected by screws to the supporting panels made of aluminum honeycomb 40 mm thick (Fig. 5.7).

The fractional radiation length of the elements of the mirror supporting system are listed in Table 5.3. The total fractional radiation length is compatible with the design value.

5.3.2 Long term mechanical stability monitoring

A full scale prototype of the RICH 2 mirror support system, shown in Fig. 5.8, was built to study and qualify the mechanical properties and the long term mechanical stability. The measurement consisted in recording the angular movements of the mirrors installed on the prototype during several months. The ambient temperature and the humidity of the room were recorded to disentangle possible correlations. Fig. 5.9 shows a scheme of the monitoring setup. A point-like source, located close to the centre of curvature of the mirrors, was shining light on the sample mirrors. The light reflected by the mirrors was collected by a system of lenses and imaged as bright spots onto a CCD sensor. The angular movements of the mirrors were determined by measuring the displacements of the spots on the sensor. The acquisition of the CCD frame and of the temperature data was automated. The movement to monitor was the variation of the direction of the mirror axis, i.e. the possible pivoting of the mirror on the support. The optical ray reflected from the centre of the mirror (C) passes through the point where the lens would form the image of C. The spot formed on the CCD located further, translates of a distance

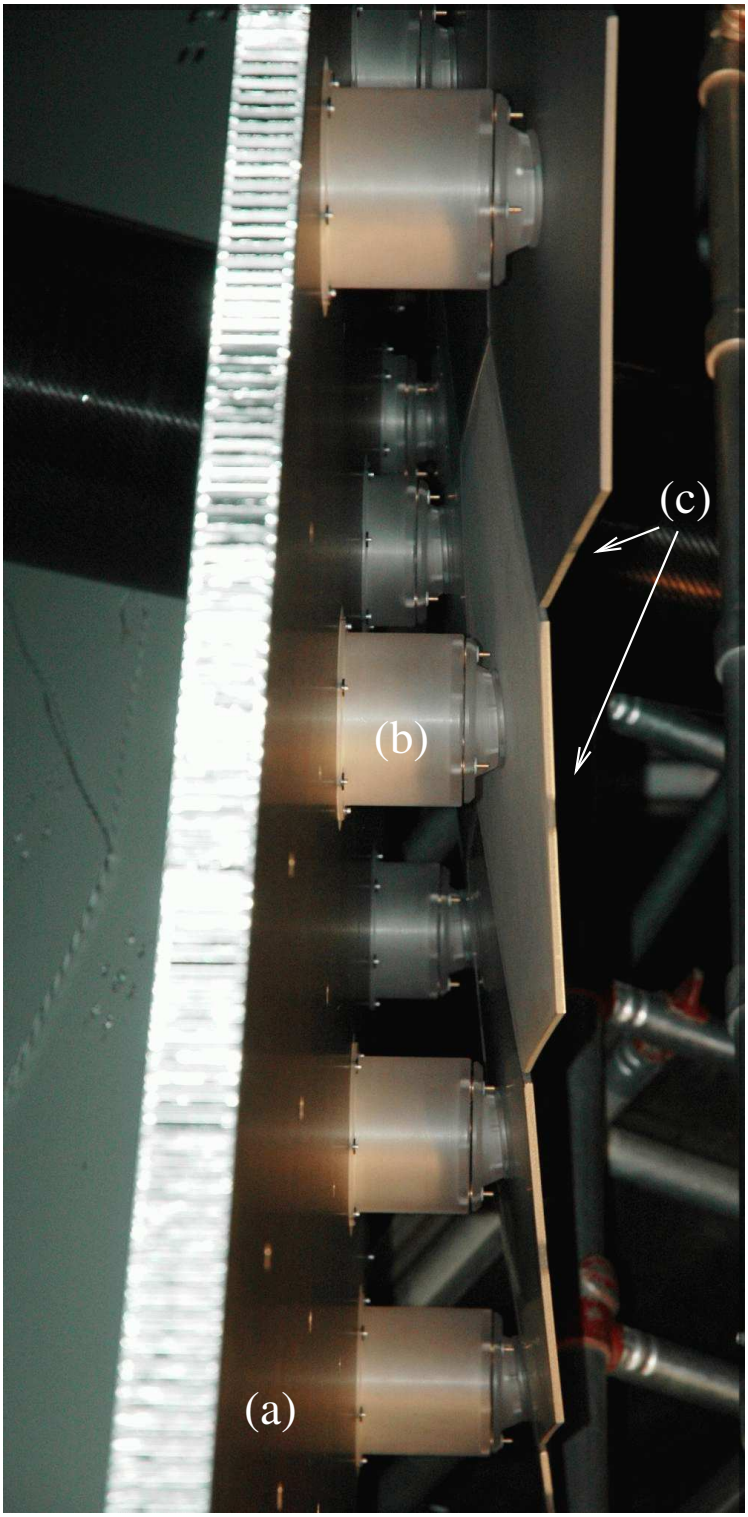

Figure 5.7: The mirror supporting system: (a) the aluminum honeycomb panel, (b) the polycarbonate supports, (c) the mirrors.

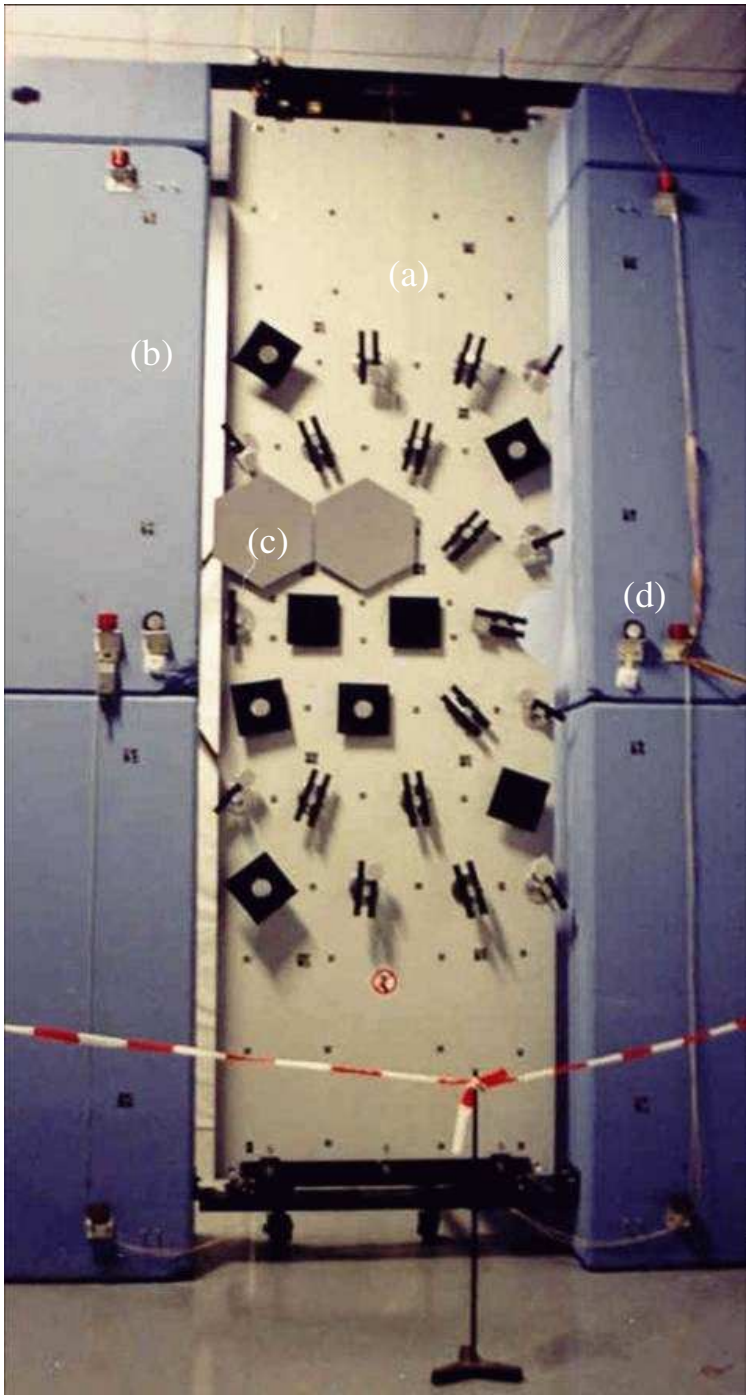

Figure 5.8: The prototype of the panel (a) with mirror supports and prototype mirrors (c) for the long term stability monitoring. The concrete blocks (b) and the reference mirrors (d) are also shown.

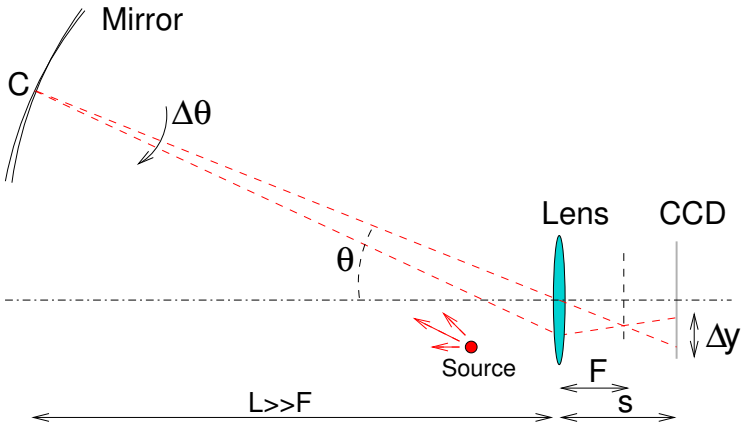

Figure 5.9: A scheme of the long term stability monitoring setup.

Δy in correspondence of the mirror angular displacement $\Delta\theta$. The sensitivity of the optical system is given by:

$$S = \frac{\Delta y}{\Delta \theta} \simeq \left(\frac{2L}{\cos^2\theta}\right)\left(1 - \frac{s}{F}\right) \tag{5.6}$$

where L is the mirror-lens distance, F the lens focal length, s the lens-CCD distance.

The measurement of the translations was based on the calculation of the intensity weighted average centres of the spots. Considering that $L \simeq 8600$ mm and that the CCD pixel size was $\sim$11 μm, a resolution of 1 μrad could be achieved with the setup. The system was calibrated by translating the point like source by a known distance and measuring the corresponding shift of the spot image.

Up to four prototype hexagonal mirrors were installed on the panel. Weights reproduced the mechanical load of the missing mirrors. Small spherical mirrors were installed on the weights to monitor the movements on the full panel. Reference mirrors were located on the supporting concrete blocks to provide an absolute spatial reference. Fig. 5.10 shows the spots from the mirrors imaged on the CCD sensor.

Fig. 5.11 shows the horizontal and vertical angular displacements recorded for a representative set of sample mirrors during almost six months. The temperature of the clean room is referred to the right axis. Large angular movements were measured during an initial period of two months. The temperature was not regulated during this period and its variations influenced the system. Mechanical deformations of the panel and strain variations at the interface between the mirror and the polycarbonate holders could be detected because of the high sensitivity of the setup. Strains induced by the glue and

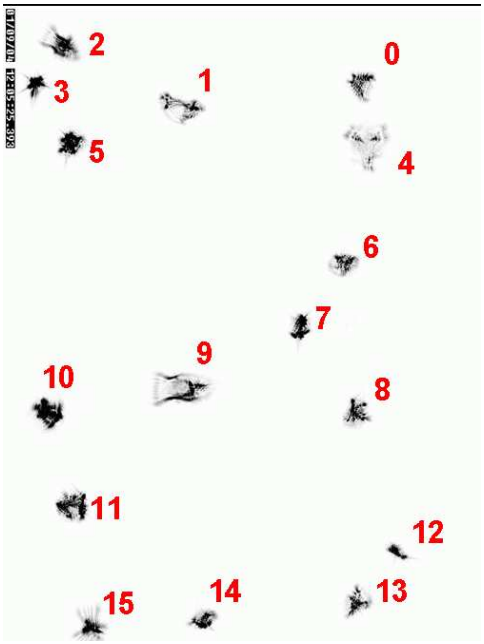

Figure 5.10: Sample frame acquired with the CCD of the long term stability setup. The spots from 16 small mirrors are visible in the negative frame.

by the screws of the polycarbonate holder are released during an initial relaxation period of approximately ∼100 days. This phenomenon is visible in the data. Angular displacements up to 150 μrad were measured. After the initial relaxation, the root mean square angular deviations of all the mirrors were below 15 μrad during the stable period from mid October to mid December (days 70-170). Later the temperature regulation failed and larger movements of the mirrors were again recorded.

5.4 Installation of the RICH 2 optical system

The production of RICH 2, not including the photon detection system, was completed by the third quarter of 2005. The mirrors were installed on their supports, mounted on the supporting panels inside the detector and then aligned to their nominal positions. Fig. 5.12 shows the two phases procedure that was used. The 28 elements of each of the two spherical surfaces were first aligned so that their optical axis intersected in the two nominal centres of curvature (C and the point symmetric with respect to the z-axis). Two optical systems similar to the one used for the long term monitoring were employed, with point-like sources and targets located at well defined positions close to the centre of curvature. One mirror element at a time or the full panel could be

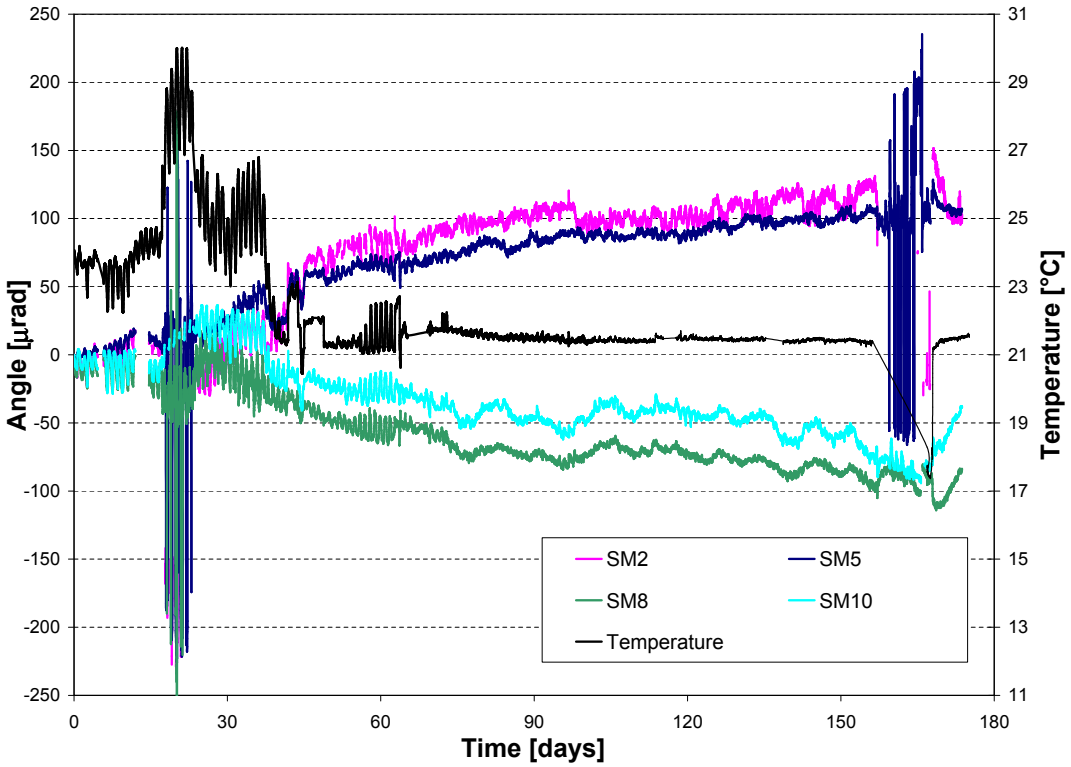

Figure 5.11: Representative subset of angular movement data for some of the mirrors of the stability monitoring prototype. Day 0 is 15/07/2003. Movements on the horizontal (vertical) plane are plotted for mirrors SM2, SM5 (SM8, SM10) and referred to the left axis (cf. Figs. 5.8 and 5.10). The temperature is plotted in black (central line) and referred to the right axis.

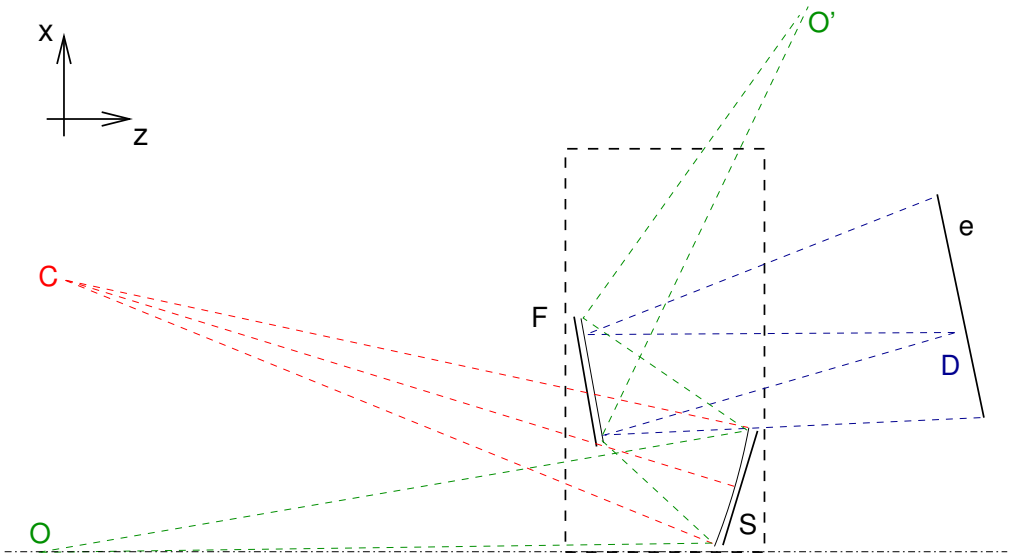

Figure 5.12: RICH 2 mirrors alignment scheme. Spherical mirrors are optically aligned by illuminating them from point C. The flat mirrors are aligned imaging a grating from D on the screen e. Finally the overall alignment is checked imaging a point-like source from O to O'. The entire procedure is repeated for the second plane mirror surface, not shown here for simplicity.

illuminated. The spots of light imaged by each mirror element on the target were recorded with a CCD camera and centres were calculated by weighted mean. This measured the mirror axis orientation with respect to the target. The three screw regulation supports were used to align each of the mirrors to the target.

The segments of the flat mirrors were aligned in a second phase. A point-like source was located in O and the light was reflected first on the aligned spherical mirrors and then on the flat mirrors. In this case, due to the large incidence angle, the image of the point source is not formed in a single point. Therefore two elements on each flat panel were first aligned until the light was reflected onto the nominal targets in O'. The remaining elements were aligned relatively to the first two by projecting a test image from D on a screen (e) after a reflection on the entire set of flat mirrors. The projected image was a mosaic of the reflections from each element and abrupt discontinuities in the projected image originated by the mutual misalignment of the flat segments. They were aligned until the discontinuities were minimized. The procedure was used for both the flat surfaces. A final check was done by verifying that the light from the point source in O was imaged on the expected targets for each of the elements. The overall procedure proved to be fast and accurate.

Scatter plots of the angular error for the alignment of the spherical mirrors

	Left panel [μrad]		Right panel [μrad]	
	6/6/2005	18/7/2005	6/6/2005	18/7/2005
RMS($\theta_x - \overline{\theta_x}$)	10	10	11	16
RMS($\theta_y - \overline{\theta_y}$)	13	20	13	21
$\overline{\theta_x}$	-12	-27	5.6	-15
$\overline{\theta_y}$	-15	-54	-11	-22

Table 5.4: Alignment of the spherical mirrors. $\theta_{x,y}$ are the projections on the horizontal and on the vertical planes of the angle between the mirror axis and their nominal directions. The mean values and RMS deviations are calculated on the 28 mirrors of each panel.

are shown in Fig. 5.13. The three sets of data refer to three sampling times after the initial alignment. The distance between the average positions of the spot centres and the target is a measurement of the overall alignment error of the spherical segments. The RMS deviation of the positions of the centres is a measurement of the inter-mirror misalignment error. Averages of data are listed in Table 5.4 and show the excellent accuracy of the alignment of the spherical mirrors. The alignment accuracy of the flat mirrors was estimated of the order of 0.15 mrad.

The development and the production of the unique RICH 2 optical system achieved the design goals. 96 thin and light highly UV reflective mirrors were developed and realized. The reflectivity of the metal dielectric coating performed above specification. The intrinsic angular resolution will have a negligible impact on RICH 2 angular accuracy. The supporting mechanical system proved to be stable and precise. Installation and initial alignment of the optical system were achieved with the desired accuracy. The system complies with the overall material budget for RICH 2.

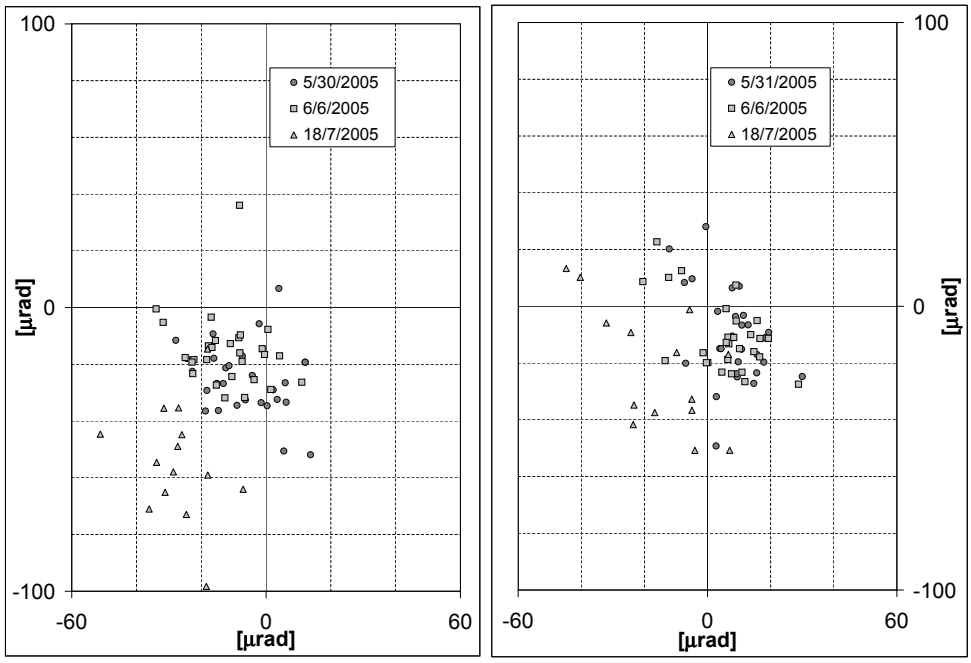

Figure 5.13: Alignment of the spherical mirrors. The projections on the horizontal and on the vertical planes of the angle between the mirror axis and the target direction (0,0) are shown. Data taken just after the initial alignment are compared with two later measurements for the left and the right panel respectively.

Bibliography

[1] O. Ullaland, "Refractive index, Transparency and other Interesting Subjects", September 2003, private communication.

[2] C. D'Ambrosio, *et al.*, "The optical system of LHCb RICHes: a study on the mirror walls and mirror specifications", CERN, Tech. Rep. CERN-LHCb-2000-071, 2000.

[3] LHCb RICH Collaboration, "LHCb RICH Technical Design Report TDR", CERN, Tech. Rep. CERN/LHCC 2000-037, September 2000.

[4] M. Laub, "Development of opto-mechanical tools and procedures for the new generation of RICH detectors at CERN", Ph.D. dissertation, 2001, Czech Technical University, Prague.

[5] A. Braem, *et al.*, "Metal multi-dielectric mirror coatings for Cherenkov detectors", *Proceedings of RICH 2004, Nucl. Instr. and Meth. A*, 2005.

[6] G. Hass, *et al.*, *Reflectance and preparation of front surface mirrors for use at various angles of incidence from the ultraviolet to the far infrared*, ser. Physics of thin films. Academic Press, 1982, vol. 12, pp. 1–51.

[7] LHCb RICH Collaboration, "LHCb RICH 2 EDR Engineering Design Review report", CERN, Tech. Rep. CERN-LHCb-2002-009, March 2002.

[8] M. Moritz, *et al.*, "Performance study of new pixel hybrid photon detector prototypes for the LHCb RICH counters", *IEEE Trans. Nucl. Sci.*, vol. 51, no. 3, pp. 1060–1066, June 2004.

Conclusion

This thesis describes the results of an extensive experimental characterization of the first prototypes of the LHCb Pixel Hybrid Photon Detector.

The quantum efficiency and the detection efficiency were evaluated by dedicated experimental setups (Chapter 2). The achievement of the required specification on sensitivity was demonstrated and the dependence of the detection efficiency on the operating parameters determined.

The prototypes were operated in a beam test with a Ring Imaging Cherenkov detector (Chapter 3). The experiment was realized to investigate the device performances under conditions replicating those of the target application. The spatial resolution and the detection efficiency of the photon detectors operating in these conditions were determined. The results confirmed that the Pixel HPD operated according to the expectations. The achievement of this milestone determined the adoption of the Pixel HPD as the photon detector for the LHCb RICHes. The data acquisition and control system developed for these experiments is currently used in the tube production process for performance verification.

The HPD sensitivity to an applied magnetic flux density and the consequent deterioration of its spatial resolution was investigated (Chapter 4) in order to determine adequate counter measures. The distortions induced by the magnetic flux density were experimentally evaluated and a model of the effects was developed. An algorithm for the correction of the distortions induced on a shielded HPD was conceived, implemented and experimentally verified. The correction procedure was completed with the implementation of an automatic method to estimate the applied magnetic flux density, based on the analysis of a light test pattern projected on the photon detector.

The experimental evaluation of the optical and geometrical properties of the RICH 2 mirrors (Chapter 5) and the implementation of original installation and monitoring methods for the RICH 2 optical system made possible to achieve the required high levels of accuracy and performance.

The fulfillment of the objectives of the described research and development activity coincides with the installation of the RICH 2 detector, complete with its optical system, in the cavern of the LHCb experiment.

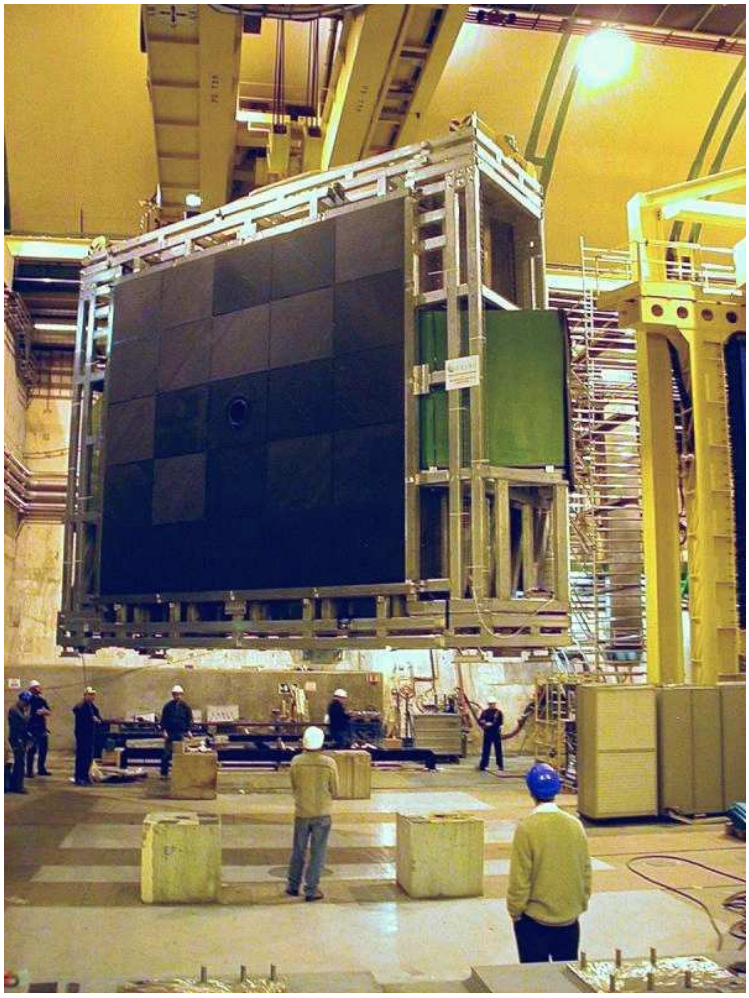

Installation of the RICH 2 detector in the experimental cavern hosting the LHCb experiment.

Simultaneously, the production and the installation of the 484 LHCb Pixel Hybrid Photon Detectors for the RICH 1 and RICH 2 detectors of LHCb began.

Glossary of particle names

This appendix serves as a quick reference for the particles mentioned along the chapters of this thesis. It does not intend to be exhaustive[1].

The Standard Model is the most accurate theory of matter constituents and fundamental forces available today[2]. It is a quantum theory including the theory of strong interactions (quantum chromodynamics, QCD) and the unified theory of weak and electromagnetic interactions (electroweak). The fourth fundamental interaction, gravity, is not part of the Standard Model. Matter constituents are fermions of two types: leptons and quarks (Table 5.5). They are subdivided in three families. Ordinary (stable) matter is made of electrons and up and down quarks. For each particle type there is an antiparticle type with the same mass and spin but opposite electric charge. The fundamental interactions are mediated by bosonic carriers. The electroweak interaction is associated with four bosons, including the photon. The strong interaction is associated to the gluon and acts on the strong charge (or color charge) of quarks and gluons.

Spin: intrinsic angular momentum of particles. It is usually given in units of $\hbar$.

Fermion: Particle of half-integer spin.

Boson: Particle of integer spin.

Hadron: Subatomic particle experiencing strong nuclear interaction. Made of quarks and gluons.

[1] The information here summarized was taken from: The Standard Model of Fundamental Particles and Interactions Chart, copyright 1999 Contemporary Physics Education Project (http://www.cpepweb.com).

[2] It is not a complete theory. Researches in theoretical physics have developed various theories beyond the Standard Model. Some experimental verifications of these theories will be done with the experiments at the Large Hadron Collider.

Barion: Fermionic hadrons made up by three quarks (qqq) or anti-quarks ($\bar{\mathrm{q}}\bar{\mathrm{q}}\bar{\mathrm{q}}$). About 120 baryons are known. Among them are the **proton** (uud, mass 0.938 GeV/c^2, charge $+e$, spin 1/2) and the **neutron** (udd, mass 0.940 GeV/c^2, zero charge, spin 1/2).

Meson: Bosonic hadrons made of a quark and an anti-quark ($\mathrm{q}\bar{\mathrm{q}}$). About 140 mesons are known. Among them are the **pion** π^+ ($\mathrm{u}\bar{\mathrm{d}}$, mass 0.140 GeV/$c^2$, charge $+e$, spin 0), the **kaon** K^- ($\mathrm{s}\bar{\mathrm{u}}$, mass 0.494 GeV/$c^2$, charge -$e$, spin 0), and the $\mathbf{B}^0$ ($\mathrm{d}\bar{\mathrm{b}}$, mass 5.279 GeV/$c^2$, charge 0, spin 0).

Matter constituents (fermions, spin 1/2)		
Leptons		
Flavor	Mass [GeV/c^2]	Electric charge
e electron	5.11×10^{-4}	-1
ν_e electron neutrino	$<1\times10^{-8}$	0
μ muon	0.106	-1
ν_μ muon neutrino	$<2\times10^{-4}$	0
τ tau	1.7771	-1
ν_τ tau neutrino	$<2\times10^{-2}$	0
Quarks		
Flavor	Approx. Mass[GeV/c^2]	Electric charge
u up	0.003	2/3
d down	0.006	-1/3
c charm	1.3	2/3
s strange	0.1	-1/3
t top	175	2/3
b bottom	4.3	-1/3

Force carriers (bosons, spin 1)		
Unified electroweak		
Name	Approx. Mass[GeV/c^2]	Electric charge
γ photon	0	0
W^+	80.4	+1
W^-	80.4	-1
Z	91.187	0
Strong (color)		
g gluon	0	0

Table 5.5: Fermionic constituents of matter and bosonic force carriers. Masses are expressed in GeV/c^2. Electric charge is in units of electron charge 1.6×10^{-19} C.

Acknowledgements

During the three years of my Dottorato di Ricerca I had the privilege to work with many people to whom I will remain indebted.

To Prof. Stefano Riva Sanseverino I owe expert and friendly supervision. He supported my participation in the CERN Doctoral Program and always advised with foresight. Carmelo D'Ambrosio, my CERN supervisor, has continuously been a source of ideas and motivation as well as a friendly teacher. Special thanks go to Olav Ullaland for having uninterruptedly guided and advised my activity. His teachings, his experience and his sagaciousness are invaluable as well as his sense of humour - he kept it also whilst reading, correcting and rejecting the drafts of this thesis dozens of times.

Thanks to Thierry Gys for countless and pleasant discussions at the board and for everything he taught me on the Pixel HPD. Thanks to Ken Wyllie for his friendly guidance and effective teaching in the realization of the photon detector readout systems.

It has been a privilege to work alongside Erich Albrecht, Christoph Frei and Didier Piedigrossi. Their dedication and skills are fabulous.

Working together with Ann Van Lysebetten, Mitesh Patel and Alex Howard has been stimulating and pleasant. Tito Bellunato has always been a forthcoming teacher as well as a good friend. Thanks to Marta Calvi for the kind and responsive review of the beam test analysis and the insight into the methods applied.

Thanks go to my colleagues of DIEET in Palermo, to the LHCb RICH team, the LHCb collaboration, the CERN PH-DT2 and PH-LBD groups for the stimulating and agreeable environment that they offered me. I greatly appreciated David Websdale's advice and recognition of my work, in which he injected rigorousness and vigor. Roger Forty's kind observations provided me with insight and always proved very useful. Thanks to Christian Joram for kindly supporting my work and for his very useful suggestions.

I would like to thank a large and fun group of *compañeros de viaje* who made pleasant the free time of the years in Geneva.

I shared a good time in the large house in Thoiry, below the Jura, with:

James Chamings, Ville Koivula, Daniel Kramer, Nina Lintzen, Bern Reinhold, Giulia Papotti, Pietro Chimenti.

To the mates of my volleyball team, Geneve Etoile, warm thanks for welcoming me in their *tissu social*: Tiziano Bernasconi, Seb Rubin, Claudio Guerrieri, Marin Barada, Gilles Boyer, Salvatore Finocchiaro, Denis Gredig, Yan Mathis, Xavier Pfister, Cyrille Kamdem.

The past three years would have been less precious without the warm friendship of Cristina Dias Soares, Sonia Taboada Gameiro, Maria Paz Casas Lino, Sabrina Picazo Marin, David Watts, Robert Gomez-Reino, Damien Laucher. Or without the Italian speaking gang: Eleonora Messineo, Belinda Bonazzi, Paolo Iengo, Massimo Della Pietra, Matteo Volpi, Andrea Dotti, Silvia Ventura, Paolo Valente, Giuseppe Lo Presti. AleDiggi, Alessandro Di Girolamo, is always running and over-clocked, that's why he slipped in this lower line. Thanks Ale.

Thanks to Tania for her love, sweetness and patience. Thanks to my brother Gabriele and to my family. They never cease to motivate and trust me: Grazie Mamma e Papà.

The kind reader will forgive me if, having opened this thesis with a quotation, I will terminate it with another one, following the Italian version of these acknowledgements. It seems to me a nice way to close the circle or - rather - the ring.

Durante il triennio del mio Dottorato di Ricerca ho avuto il privilegio di collaborare con molte persone verso le quali resterò indebitato.

Al Prof. Stefano Riva Sanseverino devo supervisione amichevole ed esperta. Mi ha sostenuto nella partecipazione al Doctoral Program del CERN e sempre consigliato in maniera lungimirante. Carmelo D'Ambrosio, il mio supervisore al CERN, è stato fonte costante di idee e motivazione, nonché un affabile insegnante. Un grazie speciale va ad Olav Ullaland per aver costantemente indirizzato e sostenuto il mio lavoro. I suoi insegnamenti, la sua esperienza e la sua sagacia sono preziosissimi, così come il suo senso dell'umorismo - lo ha mantenuto anche leggendo, correggendo e respingendo le bozze di questa tesi non so più per quante volte.

A Thierry Gys sono grato di innumerevoli e piacevoli discussioni alla lavagna e di tutto quanto mi ha insegnato sul Pixel HPD. Ken Wyllie è stato una guida amichevole ed un efficace insegnante nella realizzazione dei sistemi di acquisizione del fotorivelatore.

E' stato un privilegio lavorare al fianco di Erich Albrecht, Christophe Frei e Didier Piedigrossi. La loro dedizione e abilità sono entusiasmanti.

Lavorare con Ann Van Lysebetten, Mitesh Patel e Alex Howard è stato stimolante e divertente. Tito Bellunato è stato sempre prodigo di insegnamenti,

oltre che un amico cordiale. Grazie a Marta Calvi per la gentile e precisa critica delle misure del beam test e per gli approfonditi commenti sui metodi.

Grazie ai colleghi del DIEET di Palermo, al team di LHCb RICH, alla collaborazione LHCb e ai gruppi CERN PH-LBD e PH-DT2 per aver costituito un ambiente di lavoro stimolante e gradevole. Ho apprezzato i suggerimenti di David Websdale e la sua valorizzazione del mio lavoro, nel quale ha iniettato precisione e solidità. I gentili commenti di Roger Forty sono stati fonte di ispirazione e si sono rivelati sempre utilissimi. Grazie a Christian Joram per il gentile sostegno al mio lavoro e per i suoi utili suggerimenti.

Vorrei ringraziare un folto e allegro gruppo di *compañeros de viaje* che ha animato e reso piacevole il tempo libero di questi anni ginevrini.

Ho condiviso dei bei tempi nella grande casa alle pendici del Jura a Thoiry con, in successione: James Chamings, Ville Koivula, Daniel Kramer, Nina Lintzen, Bern Reinhold, Giulia Papotti, Pietro Chimenti.

Ai ragazzi della mia -segna!- squadra di pallavolo, Geneve Etoile, un caloroso grazie per avermi accolto nel loro *tissu social*: Tiziano Bernasconi, Seb Rubin, Claudio Guerrieri, Marin Barada, Gilles Boyer, Salvatore Finocchiaro, Denis Gredig, Yan Mathis, Xavier Pfister, Cyrille Kamdem.

Gli scorsi tre anni non sarebbero stati così preziosi senza l'amicizia di Cristina Dias Soares, Sonia Taboada Gameiro, Maria Paz Casas Lino, Sabrina Picazo Marin, David Watts, Robert Gomez-Reino, Damien Laucher. E della combriccola italofona: Eleonora Messineo, Belinda Bonazzi, Paolo Iengo, Massimo Della Pietra, Matteo Volpi, Andrea Dotti, Silvia Ventura, Paolo Valente, Giuseppe Lo Presti. Va sempre a cannone - perciò derapa senza controllo al rigo sottostante - AleDiggi, Alessandro Di Girolamo: grazie.

Grazie a Tania per il suo amore, la sua dolcezza e la pazienza. Grazie a mio fratello Gabriele e alla mia Famiglia. Non cessano mai di motivarmi e di darmi fiducia: Grazie Mamma e Papà.

Il benevolo lettore vorrà concedermi, avendo aperto questa tesi con una citazione, di terminarla con un'altra. Mi sembra un buon modo di chiudere il cerchio - o meglio: l'anello.

> The White Rabbit put on his spectacles. 'Where shall I begin, please your Majesty?' he asked.
> 'Begin at the beginning,' the King said gravely, 'and go on till you come to the end: then stop.'
>
> Lewis Carrol, *Alice in Wonderland*

Dicembre 2005
Gianluca Aglieri Rinella